

POLITECNICO DI MILANO

Scuola di Ingegneria Industriale e dell'Informazione

Corso di Laurea Specialistica in Ingegneria Biomedica



**FINITE ELEMENT SIMULATION FOR
REPLICATION OF A MAGNETIC
RESONANCE ELASTOGRAPHY (MRE)
EXPERIMENT ON AN ANISOTROPIC
MUSCLE-MIMICKING PHANTOM**

Relatore: Prof. Pasquale VENA

Correlatore: Prof. Thomas J. ROYSTON

Tesi di Laurea Specialistica di:

Chiara GAMBACORTA

matr. 918385

Anno Accademico 2019/2020

To Luigi and Marinella

ACKNOWLEDGMENTS

Firstly, I would like to thank Professor Pasquale Vena for showing his ongoing help, support and insight throughout the development of my Master thesis. I am deeply grateful to him also for his demonstration of constant presence throughout a difficult situation, as the one we are facing nowadays.

A great thanks goes to Professor Royston and Professor Klatt for welcoming me at UIC and providing me with the useful knowledge on the innovative MRE technique and for putting at my disposal any kind of equipment needed for laboratory research.

My gratitude also goes to Martina Guidetti: she has been one of the most important resources found at UIC, both as an academic tutor and as a good friend throughout the whole experience.

I would like to thank my friends both in Italy and in the USA, as part of the Acoustic and Vibrations Lab, for always welcoming, accepting me and making me feel part of a bigger family. A special thanks goes to Clelia, Noemi, Giulia, Luke, Riccardo and Pietro for being my home away from home and an endless source of joy and amusement during these difficult times. A big thank you to Simone, for always sticking with me.

Last but not least, my absolute gratitude goes to my parents, Marinella and Luigi, for always believing in me, standing by my side in every situation without ever showing a glimpse of annoyance throughout the rollercoaster of these five academic years.

ABSTRACT

Changes occurring in mechanical properties of biological skeletal muscle are often related to the presence of severe diseases that terribly affect the lives of many. For this reason, pre-emptive assessment of such changes has become a topic worthy of attention for medical doctors worldwide. In recent years, scientists have developed a new diagnostic tool, based on the MRI imaging technique, named Magnetic Resonance Elastography (MRE), a technique that is able to non-invasively assess tissue mechanical properties by relying on an initial mechanical excitation.

As for this work, MRE had been previously put to a test by the author during experiments performed at the University of Illinois at Chicago: an assembled anisotropic muscle-mimicking phantom was harmonically excited in a geometrically focused axial fashion, acquiring images of waves propagating inside the medium and eventually inverting displacement data to shear modulus values. This research study aims to provide a different point of view on the MRE technique, by reversing the common procedure steps, thus creating a Direct Formulation: mechanical properties do not represent the result of the process, rather the input for the study, performed via FE computational simulations in Abaqus; the software is fed with properties from the anisotropic phantom studied at UIC, and it eventually provides images of displacements. These are used as a source of comparison with those acquired during the experimental analysis of the phantom and are needed to validate both the numerical and the experimental procedure. Additionally, post-processing steps are performed starting from the application of a 2D Fourier Transform on the displacement data. These measures provide a qualitative and quantitative demonstration of the fact that anisotropy within tissues gives a substantial contribution to the way waves propagate. Still, some inequalities between numerical and experimental displacement images are present, due to the impossibility of having an exact match for the properties of the two works. An improvement in the accuracy of the selection of such values will elevate the analysis's accuracy and its future applications.

Overall, this work represents a further contribution to the wide panorama of research conducted on the MRE technique, providing an uncommon point of view on the technique itself. Together with many other works, it could be useful in extending knowledge on MRE, thus improving the accuracy and efficiency of diagnosis.

TABLE OF CONTENTS

ACKNOWLEDGMENTS.....	I
ABSTRACT	III
TABLE OF CONTENTS.....	V
LIST OF FIGURES.....	VIII
LIST OF TABLES.....	XII
LIST OF ABBREVIATIONS.....	XIII
SUMMARY.....	XIV
SOMMARIO.....	XIX
1 INTRODUCTION	1
1.1 ELASTOGRAPHY	1
1.2 MAGNETIC RESONANCE ELASTOGRAPHY	10
1.2.1 MRI: THE BASIS TO MRE.....	10
1.2.2 THE MAGNETIC RESONANCE ELASTOGRAPHY TECHNIQUE.....	16
1.3 SKELETAL MUSCLE AS AN ANISOTROPIC MEDIUM	21
1.3.1 ANISOTROPIC BEHAVIOUR OF SKELETAL MUSCLE.....	21
1.3.2 WAVES IN ANISOTROPIC MEDIA	22
1.3.3 WAVES IN TRANSVERSE ISOTROPIC MEDIA.....	24
2 PREVIOUS WORK AND MOTIVATION.....	29
2.1 STUDIES AT UIC AND THEIR RATIONALE	29
2.1.1 THE INVERSE PROBLEM.....	29
2.1.2 THE NOVELTY OF THE TORSIONAL ACTUATION	32
2.1.3 THE RESULTS.....	33
2.2 STATE OF THE ART AND MOTIVATION FOR THE PRESENT WORK.....	36
2.2.1 THE DIRECT PROBLEM.....	36
2.2.2 AN EXPLANATORY EXAMPLE REGARDING THE DIRECT FORMULATION.....	36
2.2.3 MOTIVATION FOR THIS WORK	38
3 MATERIALS AND METHODS	40
3.1 THE STARTING RVE GEOMETRY: ONE-ELEMENT-THICK CYLINDER.....	40

3.2 MECHANICAL PROPERTIES ACQUISITION.....	41
3.2.1 A FIRST ATTEMPT: DERIVING GLOBAL PROPERTIES FROM THE SINGLE CONSTITUENTS.....	41
3.2.2 FITTING THE REAL EXPERIMENT TO THE COMPUTER SIMULATION: AN ACCURACY COMPROMISE	43
3.3 FREQUENCY DEPENDENT MATERIAL PROPERTIES: TAKING VISCOELASTICITY INTO ACCOUNT	44
3.4 MESHING THE GEOMETRY	49
3.5 HOMTOOLS: APPLYING PERIODIC BOUNDARY CONDITIONS TO THE RVE.....	51
3.6 LOAD	54
3.7 DIRECT SOLUTION STEADY-STATE DYNAMIC ANALYSIS	55
3.7.1 IMPLEMENTATION OF THE UMAT USER SUBROUTINE.....	57
3.8 A BETTER EVALUATION OF DISPLACEMENT IMAGES VIA FOURIER TRANSFORM ...	58
3.8.1 SPLITTING THE GEOMETRY IN A QUARTER SEGMENT.....	59
3.8.2 WAVE NUMBER VS. ANISOTROPIC RATIO: A QUANTITATIVE COMPARISON.....	64
3.9 BYPASSING THE PROPERTIES FITTING: A MORE PUNCTUAL ASSESSMENT OF THE WHOLE PROCESS	67
4 RESULTS AND DISCUSSION.....	70
4.1 VARYING FIBERS MECHANICAL PROPERTIES: APPLYING DIFFERENT MATLAB FITTINGS TO THE EXPERIMENTAL DATA.....	70
4.2 EXPERIMENTAL DISPLACEMENT DATA VS. SIMULATION DISPLACEMENT DATA: A VISUAL COMPARISON	74
4.3 VARYING OF FIBERS ANISOTROPIC RATIO	77
4.4 COMBINING VARIATIONS IN FREQUENCY OF ACTUATION AND ANISOTROPIC RATIO...	81
4.5 FROM DISPLACEMENT IMAGES TO SHEAR MODULUS VALUES VIA FOURIER TRANSFORM	82
4.6 WAVE NUMBER VS. ANISOTROPIC RATIO: A QUANTITATIVE COMPARISON	87
4.7 BYPASSING THE PROPERTIES FITTING: A MORE PUNCTUAL ASSESSMENT OF THE WHOLE PROCESS	89
5 CONCLUSION AND FUTURE DEVELOPMENTS.....	93
CITED LITERATURE.....	97
6 APPENDIX A: MATLAB CODES	101
BARBERO CODE	101
FITTING VISCOELASTICITY PARAMETERS TO EXPERIMENTAL CURVES.....	104
MIRRORING THE DATA: FROM A QUARTER SLICE TO THE ENTIRE GEOMETRY	105
APPLYING FAST FOURIER TRANSFORM TO THE DISPLACEMENT DATA	106

<i>Mirroring</i>	106
<i>FFT_Fettina</i>	107
<i>Insitu_DFT</i>	108
7 APPENDIX B: USER DEFINED FUNCTIONS.....	110
UMAT TO DEFINE VISCOELASTIC PROPERTIES OF THE SIMULATION MATERIAL	110
DISP.PY: THE PYTHON CODE TO EXTRACT DISPLACEMENT AND COORDINATES DATA FROM THE ODB FILE	115

LIST OF FIGURES

Figure 1.1: MRI T1 and T2 parameters' range VS range of shear modulus in human tissues. Adapted from Fung.....	2
Figure 1.2: Different elastographic modalities. Adapted from Klatt.....	4
Figure 1.3: Compression modality in a quasi-static ultrasound based elastography technique. Adapted from Gennisson.....	6
Figure 1.4: Top: transverse wave; Bottom: longitudinal wave	7
Figure 1.5: Main Ultrasound components. Adapted from Klatt.....	8
Figure 1.6: Behavior of magnetic moments of protons with and without an external magnetic field B.	10
Figure 1.7: Bloch equation representation. Adapted from Prof Klatt	12
Figure 1.8: a) spin motion during a spin echo sequence	13
Figure 1.9: a) readout of k-space starting from bottom left point	14
Figure 1.10: Application of the Inverse Fourier Transform going from K-space to the image. Adapted from Prof Klatt.....	15
Figure 1.11: Schematic representation of intravoxel coherent motion.....	15
Figure 1.12: synchronization between excitation signal and MEG starting point	16
Figure 1.13: Correction of phase wraps. Adapted from Prof Klatt	19
Figure 1.14: Length-Tension curve for skeletal muscle tissue.....	22
Figure 1.15: Sketch of skeletal muscle as a transversely isotropic material. X and y define the plane of isotropy.	26
Figure 2.1: Schematic visualization of the UIC setup.....	30
Figure 2.2: The examined sample. From left to right: gelatin sample, anisotropic phantom, mouse muscle sample	31
Figure 2.3: Actuator systems. From left to right: piezoelectric actuator and stepper motor actuator	32
Figure 2.4: Shear modulus trend as a function of frequency for an anisotropic phantom. Double arrows represent standard deviation values. Top: real part; Bottom: imaginary part	34
Figure 2.5: wave images for anisotropic phantom after torsional excitation	35

Figure 2.6: (left) sketch of the applied displacement on the outer boundaries of the Ecoflex phantom; (right) displacement profile on the cylinder top surface as a function of radial position. Image re-adapted from Yasar et al.....	37
Figure 2.7: Displacement profiles acquired at 1500 Hz of the top surface of the cylinder along the radial direction spanning from -12.5 mm to 12.5 mm (because of axi-symmetry only half path is displayed). (Left) results from the numerical simulation; (right) results from the MRE experiment. Adapted from Yasar et al.	38
Figure 3.1: Anisotropic phantom.....	40
Figure 3.2: Starting RVE geometry	41
Figure 3.3: Fitting of computational and custom-made results for the loss modulus with actual loss modulus values from experiments held at UIC	44
Figure 3.4: Stress-strain curve for a viscoelastic material. The blue area represents the loss of energy between a loading-unloading cycle (hysteresis).....	45
Figure 3.5: Visualization of the experimental curve compared to the computational curve and relative viscoelastic parameters (first example).....	48
Figure 3.6: Visualization of the experimental curve compared to the computational curve and relative viscoelastic parameters (second example).....	49
Figure 3.7: Visualization of the nodes distribution along the geometry	50
Figure 3.8: Seeds built along the circular boundary	50
Figure 3.9: (left) 3D visualization of the meshed part; (right) top/bottom face of the meshed parts: it is evident that nodes correspond on the two faces	51
Figure 3.10: Setting procedure for the Homtools toolbox. Each request must be filled as explained in the bulleted list above	52
Figure 3.11: Visualization of the geometry after application of periodic boundary conditions (PBCs)	53
Figure 3.12: (top left) Visualization of the Constraint Manager tab with equations for each point in the top face and its corresponding one in the bottom face; (top right) Detailed explanation of the applied equations for the boundary condition for the single couple of points in the geometry; (bottom) Visualization of the two matching points to which the equations are related (posteriorly highlighted in red).....	53
Figure 3.13: Representation of the first applied boundary condition	54
Figure 3.14: Representation of the second applied boundary condition	55

Figure 3.15: Setting of the Step tab in the ABAQUS simulation.....	56
Figure 3.16: Transfer of viscoelasticity parameter , shear modulus and direction values from the UMAT subroutine to ABAQUS property tab.....	57
Figure 3.17: Slice of the global geometry that corresponds to ¼ of the total, meshed with a higher number of seeds.....	60
Figure 3.18. Outline of the process that, starting from the output database given by the ABAQUS simulation ultimately allows the extraction of the k-space, via a Python and Matlab cod	63
Figure 3.19: Visualization of the smaller geometry after mirroring operation. Picture arising from the 3 rd simulation at 600Hz with an anisotropic ratio of 0.5	64
Figure 3.20: Example of surface created from the evaluation of the Fourier transform matrix. Λ_x^{-1} and Λ_y^{-1} lay on the in-plane axes, while the vertical axis represents the power density	65
Figure 3.21: Power density as a function of λ^{-1} for both x (red line) and y direction (blue line)	66
Figure 4.1: First simulation: (left) the first seven mechanical properties represent the viscoelasticity parameters; (right) the corresponding curve fitting: the blue curve represents the computational simulation, the red curve represents the experimental data.....	70
Figure 4.2: Second simulation: (left) the first seven mechanical properties represent the viscoelasticity parameters; (right) the corresponding curve fitting: the blue curve represents the computational simulation, the red curve represents the experimental data.....	71
Figure 4.3: Third simulation: (left) the first seven mechanical properties represent the viscoelasticity parameters; (right) the corresponding curve fitting: the blue curve represents the computational simulation, the red curve represents the experimental data.....	71
Figure 4.4: Fourth simulation: (left) the first seven mechanical properties represent the viscoelasticity parameters; (right) the corresponding curve fitting: the blue curve represents the computational simulation, the red curve represents the experimental data.....	72
Figure 4.5: Fifth simulation: (left) the first seven mechanical properties represent the viscoelasticity parameters; (right) the corresponding curve fitting: the blue curve represents the computational simulation, the red curve represents the experimental data.....	72
Figure 4.6: Images resulting from properties of the first simulation, evaluated at 800Hz with an anisotropic ratio value of 0.6	74

Figure 4.7: Images resulting from properties of the third simulation, evaluated at 600Hz with an anisotropic ratio value of 0.7	75
Figure 4.8: Visual explanation of the wave pattern inside a phantom with fibers aligned in the vertical direction	76
Figure 4.9: Fourier maps for the same simulation (third simulation at 600 Hz). On the left density value is 1.06E-09, on the right density value is 4.24E-09	86
Figure 4.10: Plots from the 1 st simulation at 3000Hz. Left: anisotropic ratio of 1; Right: anisotropic ratio of 0.3. X axis represents alternatively values of λ_x^{-1} and λ_y^{-1} . Y axis represents the power density.....	87
Figure 4.11: Visualization of displacement pattern for simulations run at 1500Hz adjusting the FE shear modulus values to the experimental values. Left: anisotropic ratio value of 1. Right: anisotropic ratio value of 0.1	89
Figure 4.12: Comparison between FE simulation and MRE experiment. Frequency=1500Hz	90
Figure 4.13: Top row shows the power spectrum and plot for the simulation run at 1500Hz with an anisotropic ratio value of 1. Bottom row shows the power spectrum and plot for the simulation run at 1500Hz with an anisotropic ratio value of 0.1	91

LIST OF TABLES

Table 1.1: Impedance values as a function of density	9
Table 3.1: : Parallel and perpendicular shear modulus values using both isotropic assumption and transformation elastography theorem as a function of frequency for an anisotropic phantom	47
Table 3.2: Results of shear moduli from UIC experiments	68
Table 4.1: Values of viscoelastic parameters for each Matlab simulation	73
Table 4.2: Changes in the displacement images' pattern as the anisotropic ratio value increases the mismatch between parallel and perpendicular (to the fibers) direction.	77
Table 4.3: Changes in the displacement images' pattern as the anisotropic ratio value increases the mismatch between parallel and perpendicular (to the fibers) direction evaluated for the smaller, more thickly meshed geometry.	80
Table 4.4: Representation of displacement images from the first simulation at different frequencies (500 and 800Hz) and different anisotropic ratio (1 and 0.4).....	81
Table 4.5: Comparison between displacement image and Fourier map of the whole geometry VS the sliced geometry for different anisotropic ratio values. Properties from the 3 rd simulation (see paragraph above) at 600Hz and density value x 4.	82

LIST OF ABBREVIATIONS

MRE	Magnetic Resonance Elastography
MRI	Magnetic Resonance Imaging
US	Ultra-Sound
RF	Radio-Frequency
MEG	Motion Encoding Gradient
PBCs	Periodic Boundary Conditions
TE	Transformation Elastography
LFE	Local Frequency Estimation
AR	Anisotropic Ratio
UIC	University of Illinois at Chicago

SUMMARY

Background

Magnetic Resonance Elastography (MRE) is an imaging technique that exploits propagating mechanical shear waves to probe mechanical properties of tissues. The most immediate effect of the technique is that such waves travel faster when going through stiffer tissues, while reducing their speed through softer tissues. After having provided mechanical excitation and having visualized the way in which waves move inside the tissue itself, the MRE technique has as third and last step the inversion of displacement data in order to retrieve quantitative values for the mechanical properties.

Medical diagnosis on various body districts has pointed out the existing relation between tissues' stiffness and the presence of an ailment: this is the case of fibrosis and cirrhosis for the liver, but many other examples exist. One of these is skeletal muscle tissue, which can be severely affected by a series of neuromuscular disorders, such as atrophy or Duchenne's Muscular Dystrophy, that have an invalidating effect on the patient and exhibit as a first red flag the thickening of the tissue itself. MRE, in such context, becomes a useful and powerful tool to preemptively assess the presence of abnormal levels of stiffness in the tissues, thus allowing for an early diagnosis and treatment of severe conditions.

The challenge for MRE of skeletal muscle is given by the intrinsic viscoelasticity and anisotropy of such tissue that makes inversion to shear modulus data of difficult implementation.

This problem has been partly solved in a previous experimental work done at the University of Illinois at Chicago: an anisotropic phantom comprised of PDMS filaments inserted in a soft plastic matrix was designed in order to resemble structure of skeletal muscle tissue. Subsequently, it was harmonically vibrated in an axial fashion and displacement images were retrieved. To overcome the issue of intrinsic anisotropy of the phantom, an innovative technique named Transformation Elastography was proposed, which would simply distort the considered geometry allowing to have properties which would result isotropic in the newly created coordinate system. This would eventually allow for inversion and reconstruction of mechanical properties.

Aim of the present work

The aim of this specific thesis work is to provide further insight in the MRE world by reversing the usual plan of set passages, thus introducing a “Direct Formulation” of the problem: this is done by creating a Finite Element simulation in Abaqus where the material properties serve as inputs of the simulation and the result is given by the extraction of displacement images, whereas in a typical MRE procedure the starting point would be represented by the very same displacement maps. The work sets as its final goal the ability to better understand what role anisotropy and mechanical properties play in the propagation of waves inside skeletal muscle tissue and will eventually serve as a valuable tool to gain more knowledge on the innovative and possibly beneficial MRE technique.

Methods and Results

As mentioned before, in order to create a Direct Problem, that would basically reverse the theoretical route followed by experimental MRE on the anisotropic phantom, the Abaqus simulation carried out in this study traces step by step the previously mentioned experiment that was carried out at UIC: for this reason, input properties are given to the simulation either directly by plugging the existing value of shear modulus in a UMAT subroutine, or thanks to a Matlab curve-fitting sequence that implements equations that take viscoelasticity into account. All other Abaqus settings (Mesh, Step, Load, PBCs, etc.) were fit in such a way to be as coherent as possible with the MRE experiment.

To sum up:

- The sketched geometry represents a small part of the real phantom, thus it is called RVE (Representative Volume Element) and it has the shape of a very thin cylinder
- Mechanical properties are given as inputs to the simulation either
 - Plugging UIC experimental values in a UMAT subroutine, that was linked to the Abaqus simulation
 - Creating a trial and error approach needed to fit the experimental curves to numerical curves that were the result of equations of various parameters, accounting for viscoelasticity of the material

- The mesh is created so to have one single node along the cylinder's thickness: this guarantees to have nodes on the top circular face that are exactly overlapping nodes on the bottom circular face
- The Homtools plug-in is used to apply boundary conditions on the geometry that can be periodic, since the RVE only represents a part of the real phantom
- The load is created by means of Boundary Conditions and set to the value of $1\mu\text{m}$, as in the real experiment

Once FE displacement images are extracted, these can be compared with the ones coming from the experimental procedure, which in turn would give the properties that were now plugged as the input of the simulation. Simulations have been conducted for different frequencies of actuation and different anisotropic ratio values, in order to have a plethora of possible comparisons.

When exploiting the Matlab curve-fitting sequence, the experimental curve, given by the relationship between acquired shear moduli data and the related frequency, tends to fall in a smaller area compared to the computational curve (provided by a trial and error process) which usually possesses a wider Gaussian shape. Thus, the results in terms of comparison between displacement images show some level of discrepancies with the experimental ones, albeit still being qualitatively comparable, with a higher degree of elongation with the increase in frequency and anisotropic ratio values.

On the other hand, when directly plugging experimental values of shear moduli in the simulation via the UMAT subroutine, computational and experimental images are very much alike. This would represent a good validation of the experimental and numerical procedure.

Subsequently, various post-processing steps are conducted on the FE displacement data:

- Coordinates and displacement values are extracted by means of a Python sequence that recalls the Abaqus simulation
- These are fed as input data to a Matlab sequence. The sequence applies 2D Fourier Transform to the data and allows for visualization of the power spectrum of the given simulation where x and y coordinates are given by wave numbers in

the x and y direction, while the amplitude of the wave is represented by the color intensity.

- A plot that describes the relationship between the power density and the wave number in the two in-plane directions is computed. The plot allows for the detection of the λ^{-1} parameter: by means of simple mathematical relations this leads to the acquisition of the wave number, needed to apply the LFE theory that could be implemented to easily acquire shear modulus values, given a precise knowledge of both the level of anisotropy and the density value for the real anisotropic phantom.

Results acquired from these post-processing techniques highlight that the power spectrum is an effective tool to have an immediate visual representation of how different anisotropic ratio values affect the analyses, with high degrees of elongation when the shear moduli in the two main directions highly differ.

Although being visually representative, this analysis lacks in quantitative accuracy: this is ultimately provided by the aforementioned plots, where changes between different simulation settings are not as easily identifiable, still are quantitatively observed by simply scrolling on different points of the plot.

Conclusions and future developments

All the described processes are meant to be used as a starting point to harvest the vase of knowledge researchers have regarding the MRE technique.

The displayed results show encouraging outcomes as far as the comparison between experimental and computational studies are concerned: this assures the presence of integrity in the choice of the various steps performed both in the simulation and in reality.

Moreover, the post-processing steps on the displacement data point out the possibility of having further insight on the performed analysis and, if successful, may represent a numerical exact comparison between values of shear modulus plugged as input of the simulation and those re-acquired by the LFE.

However, discrepancies, such as diverse modes of vibrations in the computational images, are still present and this may be due to the fact that properties between the two works are not exactly the same. To have a more effective evaluation and comparison between the two, one should acquire mechanical properties values from the single components of the anisotropic phantom used at UIC and apply a homogenization procedure that would simulate the presence of a composite phantom in the Abaqus reproduction.

Still, this work has set as its intention to be a stepping stone for a wider knowledge of a technique that could represent a major breakthrough in the field of early diagnosis and therapies of conditions that are severely affecting the lives of many.

SOMMARIO

Background

L'elastografia a risonanza magnetica (MRE) è una tecnica di imaging che sfrutta la propagazione delle onde di taglio meccaniche per sondare le proprietà meccaniche dei tessuti. L'effetto più immediato della tecnica è che tali onde viaggiano più velocemente quando attraversano tessuti più rigidi, riducendo la loro velocità attraverso tessuti più morbidi. Dopo aver fornito l'eccitazione meccanica e aver visualizzato il modo in cui le onde si muovono all'interno del tessuto stesso, la tecnica MRE prevede come terzo ed ultimo passaggio l'inversione dei dati di spostamento al fine di recuperare valori quantitativi delle proprietà meccaniche.

La diagnostica medica ha evidenziato su vari distretti corporei la relazione esistente tra rigidità dei tessuti e presenza di una patologia: è il caso della fibrosi e della cirrosi epatica, ma esistono molti altri esempi. Uno di questi è il tessuto muscolare scheletrico, che può essere gravemente colpito da una serie di disturbi neuromuscolari, come l'atrofia o la distrofia muscolare di Duchenne, che hanno un effetto invalidante sul paziente ed esibiscono come primo campanello di allarme l'ispessimento del tessuto stesso. La MRE, in tale contesto, diventa uno strumento utile e potente per valutare preventivamente la presenza di livelli anormali di rigidità nei tessuti, consentendo così una diagnosi precoce e il trattamento di condizioni gravi.

La sfida per la MRE del tessuto muscolare scheletrico è data dalla viscoelasticità intrinseca e dall'anisotropia di tale tessuto che rende difficile l'implementazione dell'inversione per avere dati riguardanti il modulo di taglio.

Questo problema è stato in parte risolto in un precedente lavoro sperimentale svolto presso la University of Illinois at Chicago: un campione di materiale anisotropo composto da filamenti di PDMS inseriti in una matrice di plastica morbida è stato progettato per assomigliare alla struttura del tessuto muscolare scheletrico. Successivamente, è stato vibrato armonicamente in modo assiale e sono state recuperate le immagini di spostamento. Per ovviare al problema dell'anisotropia intrinseca del campione, è stata proposta una tecnica innovativa denominata Transformation Elastography, che si limiterebbe a distorcere la

geometria considerata consentendo di avere proprietà che risulterebbero isotrope nel sistema di riferimento appena creato. Ciò consentirebbe eventualmente l'inversione e la ricostruzione delle proprietà meccaniche.

Obiettivo del lavoro

Lo scopo di questo specifico lavoro di tesi è quello di fornire ulteriori approfondimenti riguardo al mondo della MRE, ribaltando la consueta planimetria dei passaggi impostati, introducendo così una “Formulazione Diretta” del problema: ciò avviene creando una simulazione agli Elementi Finiti in Abaqus, dove le proprietà del materiale servono come input della simulazione e il risultato è dato dall'estrazione di immagini di spostamento, mentre in una tipica procedura MRE il punto di partenza sarebbe rappresentato dalle stesse mappe di spostamento. Il lavoro si pone come obiettivo finale la possibilità di comprendere meglio quale ruolo l'anisotropia e le proprietà meccaniche giocano nella propagazione delle onde all'interno del tessuto muscolare scheletrico e servirà infine come prezioso strumento per acquisire maggiori conoscenze su questa tecnica innovativa e possibilmente vantaggiosa.

Metodi e risultati

Come accennato in precedenza, al fine di creare un Problema Diretto, che sostanzialmente invertirebbe il percorso teorico seguito dalla MRE sperimentale sul campione anisotropo, la simulazione di Abaqus condotta in questo studio ripercorre passo passo l'esperimento precedentemente citato, condotto presso la UIC: per questo motivo, le proprietà di input vengono fornite alla simulazione o direttamente inserendo il valore esistente del modulo di taglio in una subroutine UMAT, o grazie a una sequenza Matlab di “curve-fitting” che implementa equazioni che tengono conto della viscoelasticità del materiale. Tutte le altre impostazioni di Abaqus (Mesh, Step, Load, PBC, ecc.) sono state adattate in modo tale da essere il più coerenti possibile con l'esperimento MRE.

Riassumendo:

- La geometria della simulazione rappresenta una piccola parte del campione reale, per questo si chiama RVE (Representative Volume Element) e ha la forma di un cilindro molto sottile

- Le proprietà meccaniche vengono fornite come input per la simulazione attraverso
 - L’inserimento dei valori sperimentali trovati a UICc in una subroutine UMAT, collegata alla simulazione Abaqus
 - La creazione di un approccio per “tentativi ed errori” necessario per adattare le curve sperimentali a quelle numeriche: quest’ultime erano il risultato di equazioni con vari parametri, che tenessero conto della viscoelasticità del materiale
- La mesh viene creata in modo da avere un unico nodo lungo lo spessore del cilindro: questo garantisce di avere nodi sulla faccia circolare superiore che sono esattamente sovrapposti ai nodi sulla faccia circolare inferiore
- Il plug-in Homtools viene utilizzato per applicare condizioni al contorno sulla geometria che possano essere periodiche, poiché l’RVE rappresenta solo una parte del campione reale
- Il carico è creato tramite l’applicazione di condizioni al contorno ed è impostato al valore di $1\mu\text{m}$, come nell’esperimento reale

Una volta estratte le immagini di spostamento FE, queste possono essere confrontate con quelle provenienti dalla procedura sperimentale, che a sua volta darebbe le proprietà che vengono ora inserite come input della simulazione. Sono state condotte simulazioni per diverse frequenze di attuazione e diversi valori di rapporto anisotropo, in modo da avere una vasta gamma di possibili confronti.

Quando si sfrutta la sequenza di adattamento della curva di Matlab, la curva sperimentale, data dalla relazione tra i dati dei moduli di taglio acquisiti e la relativa frequenza, tende a ricadere in un’area minore rispetto alla curva numerica (data da un processo di “tentativi ed errori”) che possiede una forma gaussiana più ampia. Pertanto, i risultati in termini di confronto tra immagini di spostamento mostrano piccole discrepanze con quelle sperimentali, pur rimanendo qualitativamente confrontabili, con un grado di allungamento maggiore all’aumentare dei valori di frequenza e rapporto anisotropo.

D'altra parte, quando si inseriscono direttamente i valori sperimentali dei moduli di taglio nella simulazione tramite la subroutine UMAT, le immagini computazionali e sperimentali

sono molto simili. Ciò rappresenterebbe una buona validazione della procedura sperimentale.

Successivamente, vengono condotte varie fasi di post-elaborazione sui dati di spostamento FE:

- Le coordinate e i valori di spostamento sono estratti tramite una sequenza Python che richiama la simulazione di Abaqus
- Questi sono inseriti come dati di input in una sequenza Matlab. La sequenza applica la trasformata di Fourier 2D ai dati e consente la visualizzazione dello spettro di potenza della simulazione data dove le coordinate x e y sono date da numeri d'onda nella direzione x e y, mentre l'ampiezza dell'onda è rappresentata dall'intensità del colore.
- Viene calcolato un grafico che descrive la relazione tra la densità di potenza e il numero d'onda nelle due direzioni piane. Il grafico permette di rilevare il parametro λ^{-1} : tramite semplici relazioni matematiche si ottiene l'acquisizione del numero d'onda, necessario per applicare la teoria LFE che potrebbe essere implementata per acquisire facilmente i valori del modulo di taglio, previa una precisa conoscenza sia del livello di anisotropia che del valore di densità per il campione anisotropo reale.

I risultati acquisiti da queste tecniche di post-elaborazione evidenziano che lo spettro di potenza è uno strumento efficace per avere una rappresentazione visiva immediata di come i diversi valori del rapporto anisotropo influenzino le analisi, con alti gradi di allungamento quando i moduli di taglio nelle due direzioni principali sono molto diversi.

Pur essendo visivamente rappresentativa, questa analisi manca di accuratezza quantitativa: questo è in definitiva fornito dai suddetti grafici, dove i cambiamenti tra le diverse impostazioni di simulazione non sono così facilmente identificabili, ma sono in ogni caso osservabili quantitativamente semplicemente scorrendo su diversi punti del grafico.

Conclusioni e sviluppi futuri

Tutti i processi descritti sono pensati per essere utilizzati come fonte di alimentazione del vaso di conoscenza che i ricercatori hanno sulla tecnica MRE.

I risultati visualizzati mostrano esiti incoraggianti per quanto riguarda il confronto tra studi sperimentali e computazionali: questo assicura la presenza di integrità nella scelta dei vari passaggi eseguiti sia nella simulazione che nella realtà.

Inoltre, le fasi di post-processing sui dati di spostamento evidenziano la possibilità di avere ulteriori approfondimenti sull'analisi eseguita e, in caso di successo, possono rappresentare un confronto numerico esatto tra i valori del modulo di taglio inserito come input della simulazione e quelli riacquisiti dalla LFE.

Tuttavia, sono ancora presenti discrepanze, visibili ad esempio nelle diverse modalità di vibrazione nelle immagini computazionali, e ciò può essere dovuto al fatto che le proprietà tra le due analisi non sono esattamente le stesse. Per avere una valutazione e un confronto più efficace tra i due lavori, potrebbe essere necessario acquisire i valori delle proprietà meccaniche dai singoli componenti del campione anisotropo utilizzato presso UIC e applicare una procedura di omogeneizzazione che simuli la presenza di un campione composito nella simulazione di Abaqus.

In ogni caso, questo lavoro vuole dare un contributo per una più ampia conoscenza di una tecnica che potrebbe rappresentare un importante passo avanti nel campo della diagnosi precoce e della terapia per patologie che stanno gravemente influenzando la vita di molti.

1 INTRODUCTION

1.1 ELASTOGRAPHY

Knowledge of hardness and softness of a tissue can be a useful tool to assess pathological status of a patient. This is no new discovery for medical doctors that for centuries have exploited traditional methods with senses such as hearing of sounds or auscultation, visual perception, and manual palpation and were able to characterize biological tissues by assessing their response to deformation^{1 2}. An example of this may be given by the fact that many tumors affecting a variety of different tissues such as breast, thyroid and prostate³, that may be sometimes neglected by preoperative CT and MRI images, are easily detected by the physician's touch^{4 5}. Nevertheless, limitations are present within these traditional "senses" methods as well, as they are restricted to the body surface, there is no precise identification of location inside the body, and perception is a qualitative measure subject to intra and inter observer variability⁶.

On the other hand, conventional imaging modalities (CT, MRI for example) are incapable of determining elastic properties of tissue, since their depicted parameters span over a much narrower range with respect to the shear modulus of human soft tissue.

An example of the different ranges of application of MRI parameters T1 and T2 and shear modulus of human soft tissue is depicted in *Figure 1.1*^{7 8}.

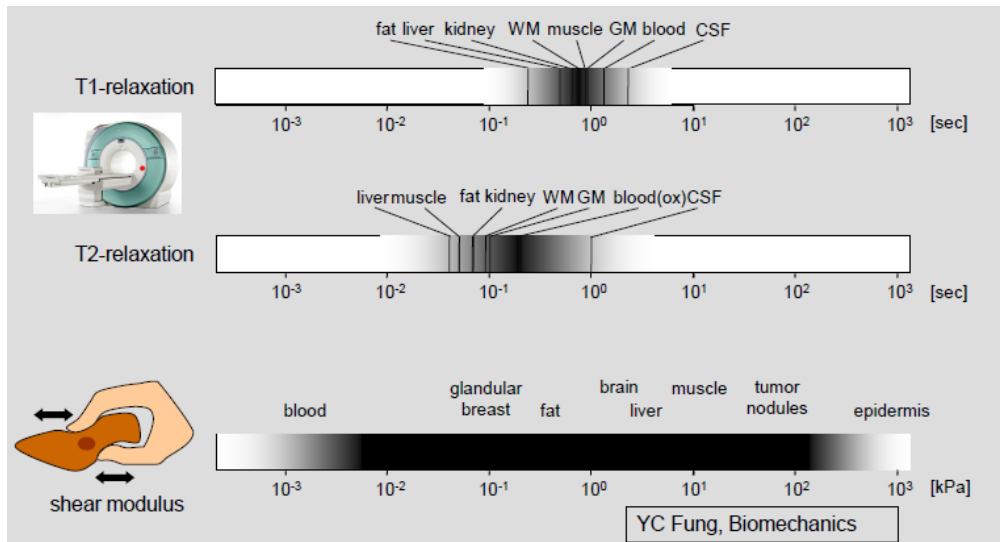


Figure 1.1: MRI T1 and T2 parameters' range VS range of shear modulus in human tissues. Adapted from Fung

During the last thirty years scientists, engineers and medical doctors have recognized the importance and benefit of precisely assessing tissue's mechanical properties and a cooperation began in order to overcome the aforementioned constraints, by developing a novel technique named "elastography".

Elastography has the final purpose of acquiring the value for the tissue's Young's Modulus E , visible by means of color maps; two consequences arise from the acquisition: first of all, different tissues that display different Young's Modulus values, can be easily differentiated one from the other; the second consequence derives from the knowledge of E itself, which leads to the tissue's stiffness' characterization⁹. Elastography, in such a way, is said to be a diagnostic technique that measures mechanical properties of tissues, amongst which stiffness plays a predominant role, through the use of images¹⁰. Harmonic vibrations are non-invasively introduced inside the tissue thanks to an actuator system that contextually measures their velocity through the body component of interest. No needles are required in order to lead such vibrations, nor any other kind of aggressive and intrusive modality: for this reason, elastography has the advantage of being non-invasive and sensitive to pathological changes and sometimes referred to as a "remote palpation by imaging" technique¹¹.

A good example of tissue in which this technique can be used as a non-invasive alternative to the current most exploited diagnostic techniques is the liver; hepatic fibrosis is a severe disease that entails the stiffening of the tissue: this may be worsened reaching the state of cirrhosis that could eventually lead to the development of hepatocellular carcinoma and to liver failure with need for transplantation^{12 13}: the diagnostic tool considered as the gold standard to determine the presence of such a condition is liver biopsy. However, this technique has several limitations and the big disadvantage of using a needle to obtain a sample of the tissue, resulting in the patient's risk and discomfort¹⁴, which in turn can be cause for the patient's refusal, along with morbidity and an alarming rate of mortality^{15,16}. Moreover, the fact that liver tissue samples come in very small sizes and the analysis is subject to the doctor's subjective and qualitative assessment has led the scientific community to raise questions on the accuracy and reproducibility of the technique¹⁷⁻¹⁹, while considering the option of an alternative, less invasive methodology²⁰. This is where elastography may take place, since it represents a better alternative to biopsy and in particular "Magnetic

Resonance Elastography” is the most rigorous technique to diagnose chronic liver diseases²¹⁻²³.

Elastography finds its interpretation in a plethora of different techniques, that share the same theoretical basis (*Figure 1.2*⁸). In this work, focus will be given to magnetic resonance elastography with brief mentions to ultrasound elastography.

What differentiates these two modalities of elastography application is the imaging method they exploit to generate maps of displacement inside the examined tissue: they both lead to the reconstruction of mechanical properties of the examined piece.

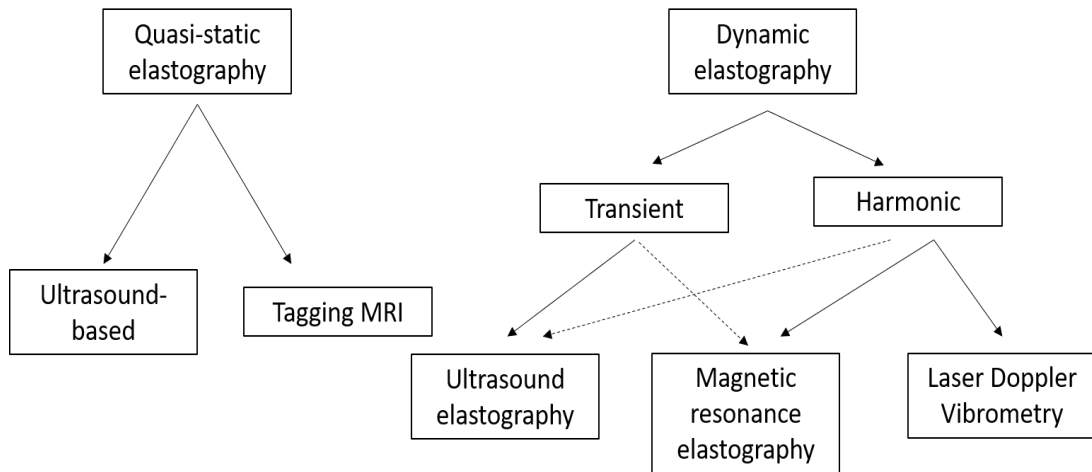


Figure 1.2: Different elastographic modalities. Adapted from Klatt

Ultrasound elastography, alternatively named “ultrasonography”, falls simultaneously under the two different macro-categories of quasi-static and dynamic elastography.

In quasi-static elastography a constant stress is applied to the tissue under examination: this test allows for the acquisition of the strain ε resulting from the stress σ . On a theoretical basis, Hook’s Law could return the value for the Elastic Modulus E as a result of its simple linear formula

$$\sigma = E\varepsilon \quad [1.1]$$

Nevertheless, practice lacks the familiarity with the value for the applied stress σ , which in turn prevents the identification of E; furthermore, these static approaches heavily depend on unknown boundary conditions.

The final result of the quasi-static methods is an “elastogram”, which is the strain value ε in the form of a strain map: this eventually provides an indirect indication of the tissue’s stiffness ¹⁰.

Ultrasound is one of those techniques retrievable at one stage under the elastographic category of quasi-static methods: first experiments and studies with these method were carried out by the Ophir Group ²⁴ in the 1990s and the technique is now of wide implementation in the case of lesions occurring in the breast area; the tissue gets compressed and strain values are consequently extracted by means of derivation of the displacement calculated through conventional ultrasound images. Its limitations lie in the fact that the applied stress needs to be controlled by an operator and the unsophisticated compression modality allows for examination of superficial body components solely (see *Figure 1.3*) ⁹.

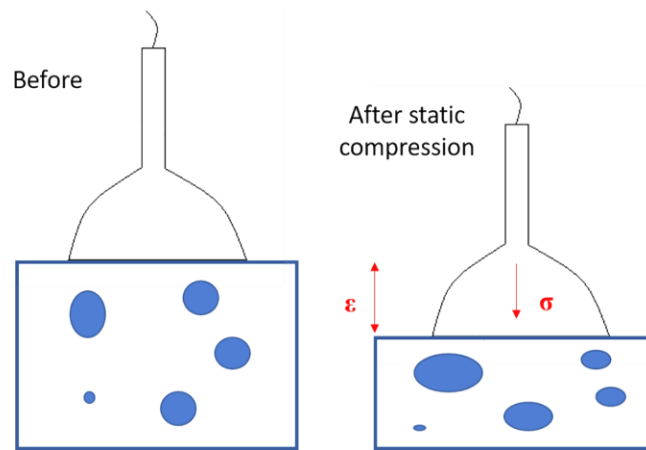


Figure 1.3: Compression modality in a quasi-static ultrasound based elastography technique. Adapted from Gennisson

In dynamic elastography, on the other hand, a time varying input excitation is employed, and this travels through the body in the form of waves. Modalities of force application can be twofold: either by a transient stimulus or by a harmonic oscillatory actuation that stimulates the tissue: ultrasonography utilizes both the transient and the harmonic excitation, while magnetic resonance elastography is only feasible through the latter modality.

With solid media, after propagation of mechanical waves two wave types are visible: longitudinal/compressional waves and shear waves.

Longitudinal waves are able to travel through all types of mediums (liquid, solid and gaseous); their direction of wave motion (V_l) is parallel (both in the same and the opposite way) to the tissue's displacement direction (\mathbf{u}).

Shear waves instead only proceed through solid bodies and their direction of propagation (V_s) is perpendicular to the oscillation (\mathbf{u}) they provide (Figure 1.4).

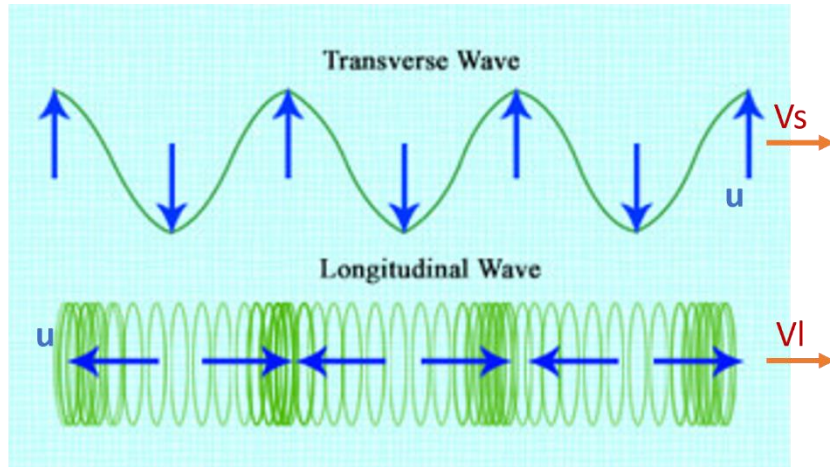


Figure 1.4: Top: transverse wave; Bottom: longitudinal wave

Shear waves propagate inside the body with a velocity that spans from 1 m/s to 50 m/s and, much slower than what occurs with longitudinal waves (where it can get up to 1500 m/s and at high frequency values). Moreover, due to absorption at high frequency values, shear waves only get produced at low frequencies that get up to 2000 Hz.

The velocity value is linearly associated with the shear modulus for the tissue μ and, in turn, by means of simplifying assumption of incompressibility inside biological matter the shear modulus can lead to identification of the Young's Modulus E ⁹.

$$\mu = \rho V \quad [1.2]$$

$$E = 3\mu \quad [1.3]$$

In these last years, research has mainly addressed shear wave propagation because of the greater dynamic range provided by shear modulus μ , with respect to the slimmer range (one order of magnitude) given by longitudinal waves ²⁵.

However, the Ultrasound technique belonging to the dynamic elastography group is used with both these types of waves (longitudinal and shear).

Compressional ultrasound waves are largely used in diagnostic imaging: the waves are sent towards a transducer that has been positioned on the area of interest. Ultrasound transducers are devices that can, not only transmit, but also detect vibrations. These vibrations, after hitting the desired tissue or component of interest, get reflected back to the transducer in the form of echoes. Finally, a computer converts them into images²⁶. This diagnostic modality allows for pregnancy detection as well as visualization of several body districts such as the heart, blood vessels, muscles and abdomen.

Figure 1.5 shows main components needed for the diagnostic visualization via US⁸.

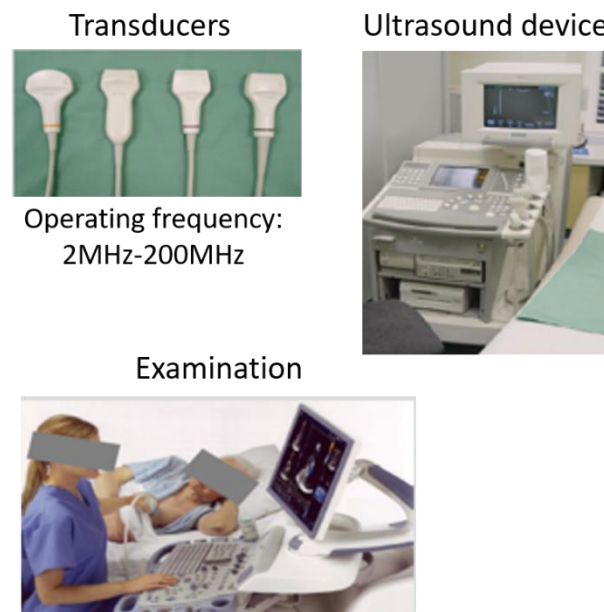


Figure 1.5: Main Ultrasound components. Adapted from Klatt

What allows discrimination between different body components is the presence of contrast within the image itself: contrast is given by the impedance property (Z parameter) that characterizes different tissues, and that represents the resistance opposed by materials to sound. It also gives an estimation of the distance/depth of the surface where the sound wave gets reflected.

$$Z = \rho c \quad [1.4]$$

where ρ is the density of the material and c the compression wave velocity

$$d = \frac{c \times t}{2} \quad [1.5]$$

d represents distance from the transducer, c is the compression wave velocity and t is the wave travel time.

Table 1.1 shows density and related Z values for different substances.

Table 1.1: Impedance values as a function of density

substance	c [m/s]	Z [g·cm ⁻² ·s ⁻¹]	ρ [g/cm]
air	331	43	0.013
fat	1470	$1.42 \cdot 10^5$	0.97
water	1492	$1.48 \cdot 10^5$	0.998
brain	1530	$1.56 \cdot 10^5$	1.02
muscle	1568	$1.63 \cdot 10^5$	1.04
bone	3600	$6.12 \cdot 10^5$	1.70

1.2 MAGNETIC RESONANCE ELASTOGRAPHY

1.2.1 MRI: THE BASIS TO MRE

Magnetic Resonance Elastography is one of the aforementioned types of Elastography and, as hinted by the name itself, it is based on the well-known Magnetic Resonance Imaging technique. For this reason, before presenting conceptual explanations of this novel technique a brief overview on MRI will be provided.

The starting point for an MRI diagnosis is the presence of nuclei (usually protons) inside the body: these possess a spin associated with a magnetic moment, whose vector sum produces a macroscopic magnetization M . The M magnetization vector can be sensed under the condition that spins possess a coherent direction: condition that gets observed only in the presence of an external magnetic field B . In this way, at thermal equilibrium the magnetization vector M becomes parallel to B (*Figure 1.6*).

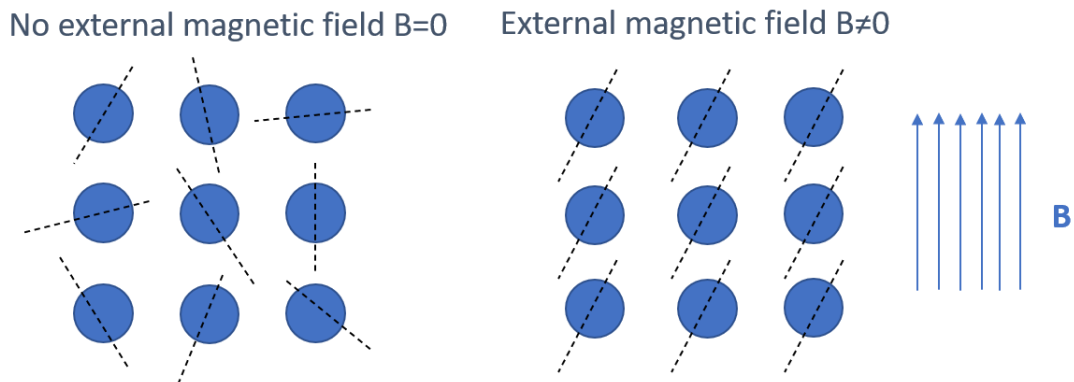


Figure 1.6: Behavior of magnetic moments of protons with and without an external magnetic field

B.

Nuclei that possess a spin are able to precess on their axis with a certain frequency, which is given by merging the external magnetic field and the body magnetic moments. This results in the so called “Larmor frequency”, whose formulation is given by

$$\omega = \gamma B \quad [1.6]$$

where γ represents the gyromagnetic ratio, that is to say the ratio of its magnetic moment to its angular moment.

The final goal of Magnetic Resonance Imaging is the retrieval of the transversal component of the M magnetization vector, by means of an RF coil system that possesses frequency equal to the Larmor frequency: this latter condition is known as the Resonance Condition

$$\Omega_1 = \gamma B \quad [1.7]$$

where Ω_1 is the frequency of the RF pulse; this prerequisite is needed in order to flip with an angle of α the magnetization vector to reach its perpendicular component M_t . The α angle needs to be as large as possible, ideally with a value of $\alpha = 90^\circ$: as a matter of fact, over time, the system is drawn to the condition of its thermal equilibrium; this means that the parallel component of M , M_l , tends to acquire its initial value, while the perpendicular component M_t is driven to zero. The α value is determined both by the RF pulse duration τ and its amplitude B .

The evolution of the magnetization vector over time is the combination of the rate of loss of M_t , caused by interaction between spins, and the rate of regain of M_l due to spin-lattice interaction, as follows

$$\frac{d\mathbf{M}}{dt} = \gamma(\mathbf{M} \times \mathbf{B}) - \frac{M_x \mathbf{e}_x + M_y \mathbf{e}_y}{T_2} - \frac{M_z \mathbf{e}_z + M_0 \mathbf{e}_z}{T_1} \quad [1.8]$$

Spin-spin interaction is cause for the dephasing, which consequently leads to loss of signal. The dynamics of the presented formula are shown in *Figure 1.7*⁸

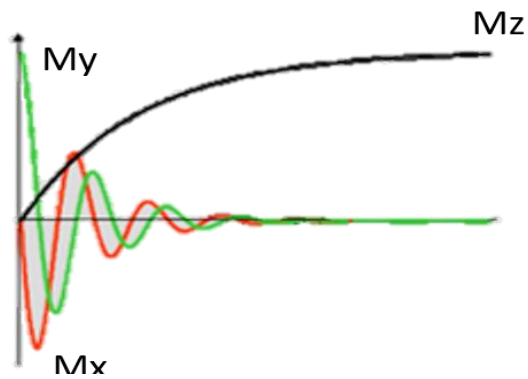


Figure 1.7: Bloch equation representation. Adapted from Prof Klatt

Various sequences for The RF pulse can be implemented with several modalities, and each provides different behaviors of the transverse magnetization. The most used one for MRI diagnostic procedures is the “spin echo” sequence: here a 90° pulse drives the magnetization vector M into its transverse component M_t ; then a 180° pulse corrects for the dephasing effect due to the inhomogeneities of the field. The actual MR signal is readout during an echo as seen in *Figure 1.8*.

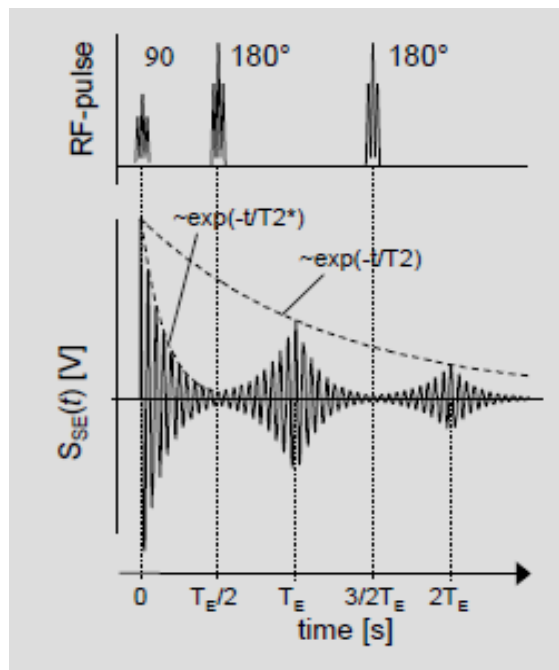
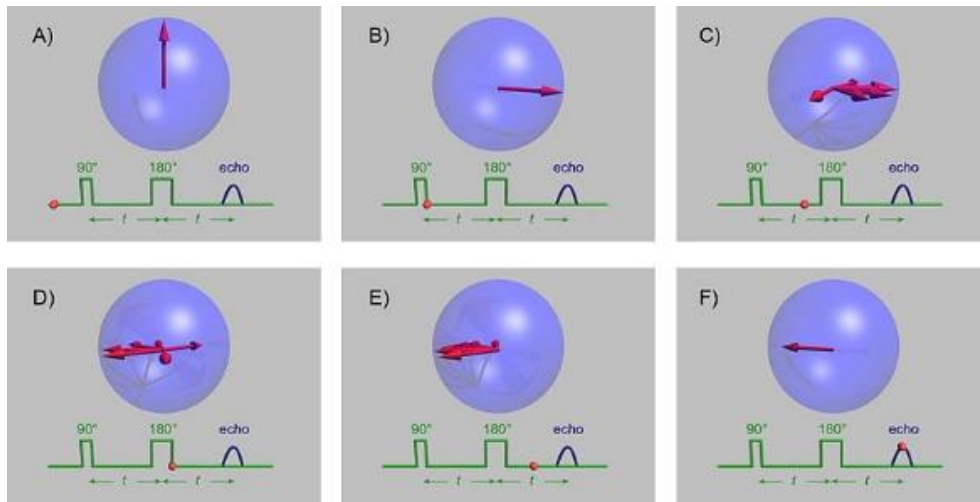


Figure 1.8: a) spin motion during a spin echo sequence

b) spin echo sequence in terms of RF pulse and corresponding signal. Adapted from Prof Klatt

Three main components are comprised in the hardware setup for an MRI system: the magnet, the RF coils and the gradient coils. The RF coils not only determine the presence of the transverse magnetization but also serve as antennas to measure voltage changes; gradient coils (in all three directions of motion), on the other hand, are necessary to encode the spatial variation of the magnetic field, since different points in space entail different frequency

values and consequently a change in the MR signal. The fact that these coils are active in all three directions allows for a diversification of the acquired signal: the gradient along the z direction allows to obtain the selection of a specific slice of the object that is being assessed, thus the value for Mt in that specific slice; as for the x direction, this is related to the phase encoding, which means that every x coordinate has a different phase, while the y direction is appointed to the frequency encoding, such that every y coordinate has a different frequency.

In this way every voxel becomes singularly identifiable, because it has its specific frequency and accumulated different phase: eventually a 2D Fourier Transform is applied on the Mt transverse magnetization, which, in this way, allows for acquisition of the MR signal in the so called k-space. The signal is then read line by line starting from the bottom left point as seen in *Figure 1.9*⁸ and each line is acquired in one Repetition Time TR until the whole k-space is completed; the desired image will be finally given by an inverse Fourier Transform, that provides visualization of the MR signal in the form of two different images: one for the magnitude and one for the phase of the transverse magnetization Mt (*Figure 1.10*⁸)²⁷.

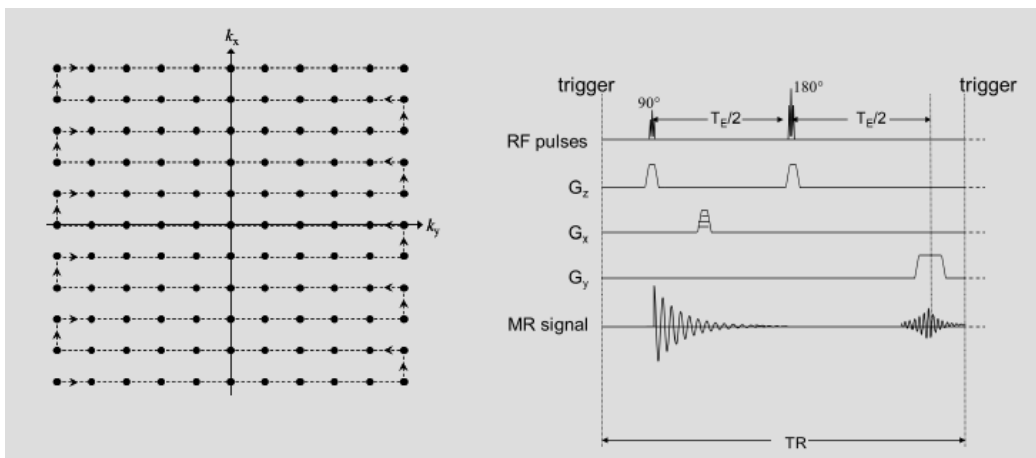


Figure 1.9: a) readout of k-space starting from bottom left point

b) spin echo sequence repeated for every TR. Adapted from Klatt

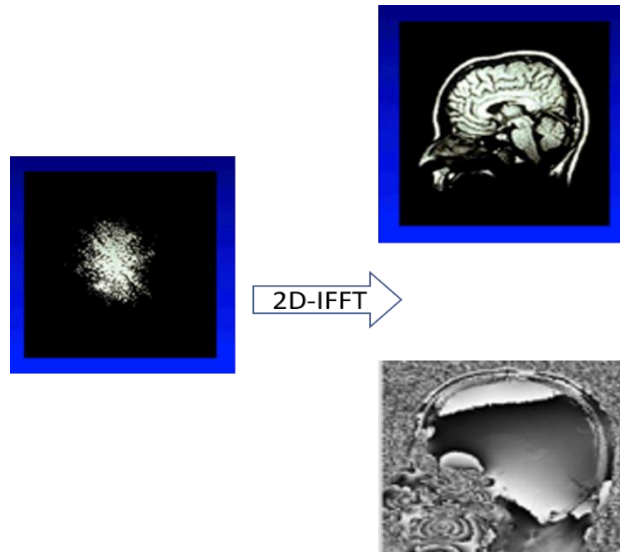


Figure 1.10: Application of the Inverse Fourier Transform going from K-space to the image. Adapted from Prof Klatt

MRI is not restricted to one single modality, instead it can detect different kinds of motion. The oscillation considered in Magnetic Resonance Elastography is the “intravoxel coherent motion”, thus this will be the one here described. Within intravoxel coherent motion, voxels are capable of moving inside the matter; however, the relative position of spins one with respect to the other remains static. This results in the fact that, since they precess coherently, all spins within one voxel are in phase, bringing the macroscopic magnetization to its maximum.

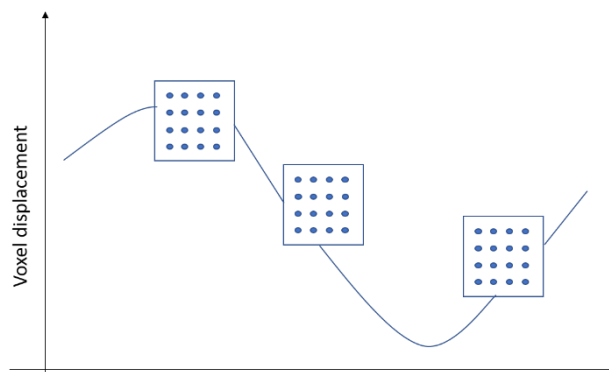


Figure 1.11: Schematic representation of intravoxel coherent motion

1.2.2 THE MAGNETIC RESONANCE ELASTOGRAPHY TECHNIQUE

Magnetic Resonance Elastography differs from MRI because of the addition of two components that are essential for such a technique:

- 1) A mechanical excitation signal: this is explicated by means of mechanical waves that travel inside the material
- 2) A Motion Encoding Gradient (MEG), which can be defined as the mean through which vibration of voxels get encoded within a phase value φ .

To clarify, a Motion Encoding Gradient is used for vibration estimation and it is not to be confused with the MRI gradients (G_z , G_y , G_x), which are used for position encoding instead.

Fundamental prerequisite for a correct MRE analysis is that the wave motion excitation signal is synchronized with the MEG: in order to satisfy this condition, the MEG phase must be zero at its starting point in time ($t=s$). This is given by the relation

$$\theta_k = \omega_k s \quad [1.9]$$

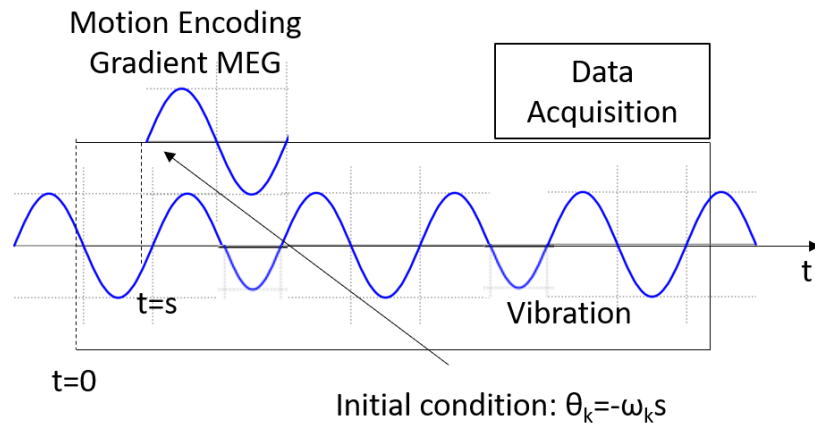


Figure 1.12: synchronization between excitation signal and MEG starting point

Reaching a steady state condition of the harmonic vibration is a further condition for the MEG application. In this way all voxels possess the same frequency.

One of the fundamental goals for an MRE analysis is the acquisition of snapshots of the waves that move inside the tissue. This movement is expressed in the form of displacement values that are in units of micrometers: the MEG is important because it represents the starting point of calculations that can lead to this ultimate objective.

As a matter of fact, the deflection (\mathbf{u}) given by the vibrations can be combined with Motion Encoding Gradients to obtain the phase of the transverse magnetization.

This last parameter can, in turn, lead to the extraction of the ‘‘Encoding Efficiency’’ ξ_n .

Mathematical steps are hereby shown

$$K(t) = K_0 \sin(\omega_k t + \theta_k) \quad [1.10]$$

\mathbf{K} is the Motion Encoding Gradient

$$u(t) = Y_n \sin(\omega_n t + \theta_n) \quad [1.11]$$

\mathbf{u} is the deflection

$$\phi(s) = \gamma \int_s^{s+\tau_k} \mathbf{K}(t) + \mathbf{u}(t) dt \quad [1.12]$$

γ represents the gyromagnetic ratio, ϕ is the phase of Mt and it is a function of the start time s of the MEG.

$$\xi_n = \frac{\phi_n^0}{Y_n} \quad [1.13]$$

where ϕ_n^0 is retrievable from the definition of phase

$$\phi(s) = \phi_n^0 \sin(\omega_n s + \theta_n + \Delta\theta_n) \quad [1.14]$$

Encoding efficiency is the actual tool that allows for the transformation from MR phase images, expressed with radians, to displacements, that, as mentioned before, are expressed in micrometres.

Sometimes the analysis may deal with the presence of mechanical vibrations that possess multiple frequency values: this approach also allows to increase spatial resolution. In this case, the value for the encoding efficiency must be high enough to include all the frequency values taken into consideration.

Displacement values that result from these steps are provided by the system in the form of complex (with a real and an imaginary component) matrices, and from now on are going to be called with the name of wave images. Wave images are provided for each applied external frequency.

Before finally reaching the identification of mechanical properties (stiffness, elasticity and viscosity values for a tissue), which is the ultimate objective of an MRE experiment and that we know to be possibly beneficial in the subsequent treatment of many diseases²⁸, data processing right before and after acquisition of the wave images needs to be performed.

This step comprises various passages, six in particular:

- 1) The phase difference calculation: this is used to correct for static magnetic field inhomogeneities, that lead to the acquisition of an accumulated phase, since they entail the presence of differences in phase from one pixel to another. Such a calculation can be performed by means of “complex division”
- 2) The phase wraps correction: after application of complex division needed to minimize errors given by magnetic field inhomogeneities, the image may still be corrupted by the presence of wraps. The unwrapping procedure imposes that the difference between one pixel and the next one should be less than 2π .

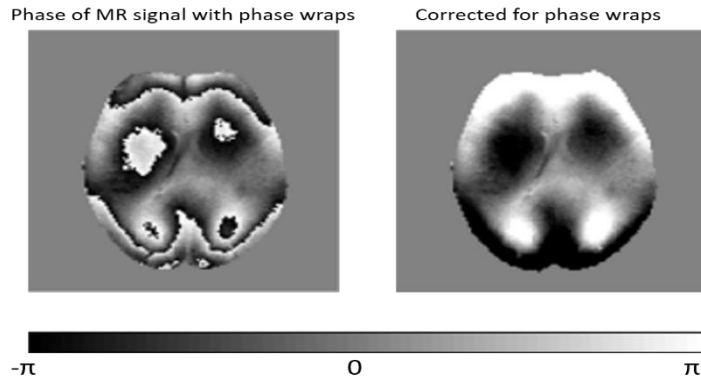


Figure 1.13: Correction of phase wraps. Adapted from Prof Klatt

- 3) The Fourier Transform along time: this is the fundamental step through which complex wave images (images of displacement \mathbf{U}) are calculated for each frequency of applied vibration
- 4) Application of a low pass filter as tool of spatial filtering: this helps attenuating errors that are present in derivatives of digital data
- 5) Wave inversion: this represents the fundamental step. Images of complex shear modulus \mathbf{G} are here acquired by means of the “Algebraic Helmholtz Inversion” algorithm.
- 6) Fitting to rheological models: the experimental complex shear modulus \mathbf{G} can now be compared to known rheological models. Viscoelastic biological models are usually described by the Springpot model; furthermore, this model only has two independent parameters and shows good reproducibility. The error function between the theoretical \mathbf{G} and the experimental one can be defined as

$$\sum_{n=1}^N |G_{exp}(\omega_n) - G_{model}(\omega_n)|^2 \quad [1.15]$$

where N represents the number of given data and G_{exp} is the shear modulus resulting from the experiment.

Focus will now be given to the fifth step of inversion. The “Algebraic Helmholtz inversion” can be exploited only with samples that fall in the category of linear elastic solid with assumptions of local homogeneity and isotropy.

The inversion procedure takes off from the equation of motion of a linear elastic solid

$$\rho \frac{\partial^2}{\partial t^2} \mathbf{u} = (\lambda + \mu) \nabla(\nabla \cdot \mathbf{u}) + \mu \Delta \mathbf{u} \quad [1.16]$$

where ρ is the density, \mathbf{u} is the deflection, λ and μ are the 1st and 2nd Lamè constants.

Equation 1.16 subsequently switches to the frequency domain, where derivatives are expressed in the form $i\omega$ (where i is the complex unit)

$$-\rho\omega^2 \mathbf{U}(\omega) = (G_L(\omega) + G_S(\omega)) \nabla(\nabla \cdot \mathbf{U}(\omega)) + G_S(\omega) \Delta \mathbf{U}(\omega) \quad [1.17]$$

G_L and G_S are respectively the complex moduli of the 1st and 2nd Lamè parameters (λ and μ). Under the assumption of incompressibility an exact solution for $G_S(\omega)$ is the one expressed in equation 1.20

$$\nabla \cdot \mathbf{U} = 0 \quad [1.18]$$

$$-\rho\omega \mathbf{U} = G_S \Delta \mathbf{U} \quad [1.19]$$

$$\mathbf{G}_S(\omega) = \frac{-\rho\omega^2 \mathbf{U}(\omega)}{\Delta \mathbf{U}(\omega)} \quad [1.20]$$

1.3 SKELETAL MUSCLE AS AN ANISOTROPIC MEDIUM

The MRE technique spans over a vast range of applications throughout the entire body. This research study focuses on its use to detect and analyze mechanical behavior of skeletal muscle: this tissue may be affected by several pathologies that have an effect on the mechanical properties of the tissue itself²⁹; furthermore, its ability to constantly contract and get released strongly affects these very same properties^{30 31}.

Skeletal muscle tissue can also be considered a suitable representative for all soft tissues, as it shares with them several characteristics: more specifically, three of those are worth mentioning

1. A density value near to the one of water

$$\rho = 1kg/dm^3 \quad [1.21]$$

2. Poisson's coefficient as an incompressible medium

$$\nu = 0.5 \quad [1.22]$$

3. This Poisson's ratio value entails the presence of a linear relationship between the value for the Young's Modulus E and the shear modulus μ , as

$$E = 3\mu \quad [1.23]$$

1.3.1 ANISOTROPIC BEHAVIOUR OF SKELETAL MUSCLE

Skeletal muscle's organization is often defined as "hierarchical": each layer is comprised of sublayers, that are made up of increasingly smaller components up to the point where the microscope reaches the intersections created by actin and myosin, the proteins which are responsible for the contraction ability of such a tissue, by means of the so called "cross-bridge cycle". As a matter of fact, each muscle is composed by fascicles, that create an envelope around little groups of muscle cells, called fibres. These present scattered nuclei

along their structure and their first microscope-visible element are the myofibrils which in turn are made up of myofilaments. At the myofilaments level myosin and actin are finally visible^{32,33}.

The hierarchical organisation is given by the repetition of geometrical patterns, which in turn provide the characteristic of anisotropy for this tissue, which is also viscoelastic and presents a non-Hookean behaviour under large deformations³⁴. All of this is visible in the length-tension curve for skeletal muscles (*Figure 1.14*).

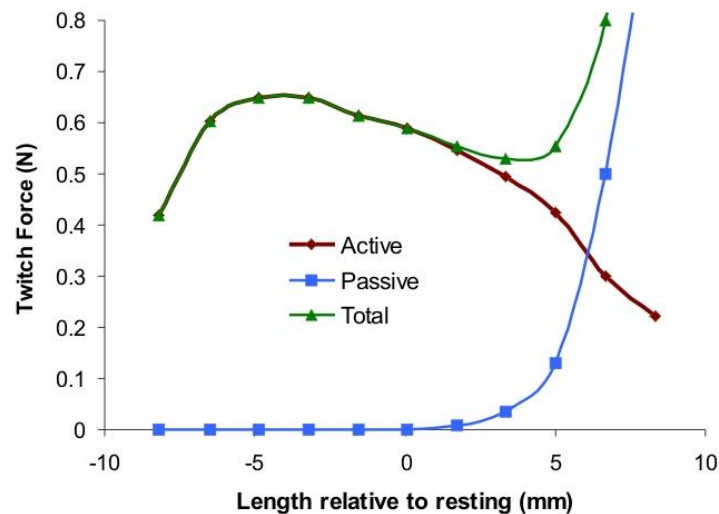


Figure 1.14: Length-Tension curve for skeletal muscle tissue

Anisotropy and viscoelasticity are major characteristics of such a tissue, that need to be taken into consideration when approaching any kind of study relating muscles: thus, it is clear that the theoretical Helmholtz inversion algorithm (that stands upon isotropy hypotheses) will need to be somehow modified in order to provide meaningful results in the muscle application.

1.3.2 WAVES IN ANISOTROPIC MEDIA

Anisotropy is a characteristic of materials that, when forced into different directions of strain, show different mechanical properties. In order to flank the wave discussion with the anisotropic world, analysis may start by considering a plane wave, presenting the form

$$u_i = u_{0i} e^{i(\mathbf{k}\mathbf{x} - \omega t)} \quad [1.24]$$

In this kind of formulation, waves, which in anisotropic media are present in the form of modes, are characterised by the presence of two main parameters: the direction of propagation \mathbf{k} and the direction of displacement, also known as polarization \mathbf{u} .

Also, in the formula, u_{0i} represents the initial polarization and amplitude of the wave; \mathbf{k} is the wave vector defined also as $|\mathbf{k}| = \omega/c$, where c is the wave speed.

Since assumptions of isotropy are not hereby respected, the two Lamè parameters (μ and λ) are not sufficient to resolve the wave equation; in order to find solution for a three dimensional space, the number of differential equations needed is equal to three. Up to now, no analytical solution has been found for such a configuration. When taking into account the plane wave, the existing relationship between its directions (of displacement and of polarization) allows for the presence of wavefields in anisotropic materials.

Inserting this wave type into the wave equation we obtain

$$\det \left(\sum_{j,k,l=1}^3 (C_{ijkl} k_j k_k - \rho \omega^2 \delta_{i,l}) u_{0i} \right) = 0 \text{ for } i = 1,2,3 \quad [1.25]$$

$$\delta_{i,l} = \text{Kronecker delta}$$

$$\omega = \text{angular frequency}$$

$$C_{ijkl} k_j k_k = \text{elasticity tensor}$$

Non-trivial solutions are found for frequencies ω that satisfy the characteristic equation.

In this case, having a 3D space, the solutions are three and those represents the modes by which the waves propagate: these three solutions allow for the existence of a relationship between $[\omega, \mathbf{k}]$ pairs. For a given ω , \mathbf{k} is the representation of waves that travel in different directions describing a surface^{35(chap1.4)}.

1.3.3 WAVES IN TRANSVERSE ISOTROPIC MEDIA

This section is specifically intended to provide further insight on the specific type of wave propagation that occurs in skeletal muscle tissue.

This kind of tissue falls under the category of the so called “transversely isotropic materials”. Transversely isotropic materials show properties which are isotropic on a plane, while being different on the perpendicular vector to the said plane.

Isotropic materials can be fully described by the Lamè constants which are a total of 2 independent parameters. This is not the case for transversely isotropic material that require five independent parameters (two Young Moduli, one shear stiffness, and two Poisson’s ratios) to be fully described. The elasticity tensor \mathbf{C} provides a good representation for different kind of materials: in the transversely isotropic case C_{1212} gets substituted by a combination of C_{1111} and C_{1122} : shear deformations and axial ones are described by the same constants in that plane, and the existence of some kind of isotropy on the plane described by direction 1 and 2 is thus validated. In the out of plane direction (direction 3), instead, strains related to shear are described by C_{1313} , which has no correlation with any other matrix element. Voigt notation allows for identification of the elasticity tensor \mathbf{C} in this way

$$\mathbf{C} = \begin{pmatrix} C_{11} & C_{12} & C_{13} & 0 & 0 & 0 \\ C_{12} & C_{11} & C_{13} & 0 & 0 & 0 \\ C_{13} & C_{13} & C_{33} & 0 & 0 & 0 \\ 0 & 0 & 0 & C_{44} & 0 & 0 \\ 0 & 0 & 0 & 0 & C_{44} & 0 \\ 0 & 0 & 0 & 0 & 0 & \frac{C_{11} - C_{12}}{2} \end{pmatrix} \quad [1.26]$$

Here relationship between stress and strain values is presented: what links the two set of values is the \mathbf{S} matrix, also known as the compliance tensor (\mathbf{C}^{-1}), that helps better understanding the concept of transverse isotropy.

The \mathbf{S} matrix acquires the \mathbf{C} elasticity tensor: this is a positive definite matrix meaning it has the possibility to be inverted.

$$\epsilon = \mathbf{S} \cdot \boldsymbol{\sigma} = \begin{pmatrix} 1/E_1 & -\nu_{21}/E_1 & -\nu_{31}/E_3 & 0 & 0 & 0 \\ -\nu_{21}/E_1 & 1/E_1 & -\nu_{31}/E_3 & 0 & 0 & 0 \\ -\nu_{13}/E_1 & -\nu_{13}/E_1 & 1/E_3 & 0 & 0 & 0 \\ 0 & 0 & 0 & 1/\mu_{13} & 0 & 0 \\ 0 & 0 & 0 & 0 & 1/\mu_{13} & 0 \\ 0 & 0 & 0 & 0 & 0 & 1/\mu_{12} \end{pmatrix} \cdot \begin{pmatrix} \sigma_{11} \\ \sigma_{22} \\ \sigma_{33} \\ 2\sigma_{23} \\ 2\sigma_{13} \\ 2\sigma_{12} \end{pmatrix} \quad [1.27]$$

The last three diagonal parameters (non-zero parameters) of the matrix show shear deformations, which are independent from axial deformation: μ represents the shear modulus values (in different directions) that associates stresses and strains. μ is also related to the Young's Modulus and the Poisson ratio in such a way ^{35(pp74-80)}.

$$\mu_{12} = \frac{E_1}{2(1 + \nu_{21})} \quad [1.28]$$

Apropos of what was previously said about skeletal muscle, defined as a transversely isotropic material, the definition lays upon the presence of fibres in such a tissue. Their direction (fibres are visualized in the plane of symmetry) shows a preferential pattern, while in the orthogonal direction to the fibres alignment an unorganised bundle of material is present and this shows no preferential direction: forces acting along the direction of the fibres produce a preferred direction for the mechanical parameters. For this reason, rules related to transversely isotropic materials also work for the description of waves that travel in this kind of tissue.

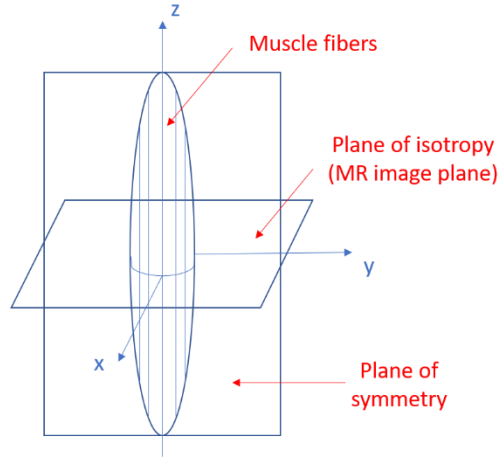


Figure 1.15: Sketch of skeletal muscle as a transversely isotropic material. x and y define the plane of isotropy.

To account for the viscoelasticity of skeletal muscle, MRE analysis needs to focus on shear waves.

With shear waves the polarization direction is opposite (meaning perpendicular) to the propagation direction (on the other hand they would be named longitudinal waves). By considering the volumetric variations to be null (as a matter of fact this tissue has high water levels, thus making it almost incompressible), the number of independent parameters necessary to fully describe the behavior of the transversely isotropic material scales to three (one ratio of Young's moduli, perpendicular and parallel to the fibers, and two shear moduli³¹): in this way solutions for the wave velocity c are given by three different modes, that are the longitudinal one (not taken into consideration because of incompressibility assumptions), the ST mode and the FT mode. In the FT mode the wave polarization and the muscle fibres lay in the same, thus it does not concern shear waves that propagate along the fibers (as previously defined shear waves only allow for mismatched propagation and polarization directions); in the ST mode polarization has a perpendicular direction with respect to the fibers.

The velocity c can be extracted for each of the two modes

$$\rho c_{FT}^2 = (4\mu_{13} - \mu_{12} - E_3)(n_3^4 - n_3^2) + \mu_{13} \quad [1.29]$$

$$\rho c_{ST}^2 = \mu_{12}(n_1^2 + n_2^2) + \mu_{13}n_3^2 \quad [1.30]$$

n = direction of propagation

μ =shear modulus

Looking at equation 1.30, if waves propagated strictly in the fibers' direction ($n_3=1$; $n_1=n_2=0$) the slow mode wave velocity would be described solely by μ_{13} .

Waves that propagate in the fibers' direction only account for the slow mode velocity, while waves propagating in a direction perpendicular to the fibers ($n_1^2+n_2^2=1$; $n_3=0$) can both be defined the slow mode wave and the fast mode wave equation.

Further and alternative description of the behavior of transversely isotropic materials can start from the evaluation of the three independent parameters that, as hinted at before, could result as the combination of the parallel and perpendicular (with respect to the fibers' direction) tensile and shear moduli (E^\perp ; E^\parallel ; μ^\perp ; μ^\parallel). New simplifying parameters can then be defined, and these are named tensile anisotropy ζ and shear anisotropy ϕ

$$\zeta = E^\parallel / E^\perp \quad [1.31]$$

$$\phi = \frac{\mu^\parallel}{\mu^\perp} - 1 \quad [1.32]$$

The ζ and ϕ definitions allow for an additional way of defining velocity for slow and fast shear waves. These new formulas show the dependence on the angle ϑ that lays between the propagation direction and the fibers' direction.

$$c_s^2 = \frac{\mu^\perp}{\rho} (1 + \phi \cos^2(\vartheta)) \quad [1.33]$$

$$C_f^2 = \frac{\mu}{\rho} (1 + \phi \cos^2(2\vartheta) + \zeta \sin^2(2\vartheta)) \quad [1.34]$$

From acquisition of velocity values, the wavelength is given by the velocity “c” over the applied frequency and the wavenumber is given by

$$k = 2\pi/\lambda \quad [1.35]$$

The viscoelastic behavior of soft tissues (and skeletal muscle tissue in this case) can be analytically described exploiting the complex nature of the shear modulus (real parts are for storage modulus, while imaginary parts are for loss modulus), following extraction of values of c in the aforementioned way ^{36 37}

$$\mu_{\perp} = \mu_{\perp R} + j\mu_{\perp I} \quad [1.36]$$

$$\mu_{\parallel} = \mu_{\parallel R} + j\mu_{\parallel I} \quad [1.37]$$

The magnetic resonance elastography technique allows to decide for the direction of encoding and excitation, but also for the visualized image plane: wave fronts that arise from the heart of the Field Of View FOV exhibit different patterns depending on the a priori settings ^{38 39 40 35(pp106-109)}.

2 PREVIOUS WORK AND MOTIVATION

2.1 STUDIES AT UIC AND THEIR RATIONALE

2.1.1 THE INVERSE PROBLEM

The work that is intended to be presented in this written composition sets its ground basis on experiments that have been previously carried out by the author in collaboration with the Acoustics and Vibration Laboratory at the University of Illinois at Chicago for the period going from August 2019 up to May 2020.

As explained in previous chapters (1.2.2) the conclusive step for the MRE analysis of a sample/phantom entails the use of an inversion algorithm that allows passage from displacement values to corresponding shear modulus values ⁸ and that brings about the resolution of the so called “Inverse problem”.

A large range of inversion/reconstruction modalities have been presented by several authors throughout the years and these differ one from the other for inputs, physical assumptions and computational costs.

Amongst these, the one technique employed for such experiments at UIC, has been the direct inversion (DI) method, that presents less of a computational cost with respect to iterative methods and shows heavier dependence on displacement data quality ⁴¹. As a matter of fact, direct methods (that also account for local homogeneity of stiffness values) allow for the use of least squares in order to retrieve stiffness values for each voxel i , performing an inversion of the harmonic viscoelastic equation pixel by pixel.

$$\mathbf{G}_i(\omega) = \frac{-\rho\omega^2(\Delta U)_i^T \mathbf{u}_i}{(\Delta U)_i^T (\Delta U)_i} \quad [2.1]$$

At UIC experiments were carried out onto three different specimens: a gelatin homogeneous and isotropic sample, a mouse-muscle sample and an anisotropic phantom. The latter had been previously customized by team members of the same Lab and consisted of an array of PDMS filaments comprised into a soft plastic matrix. This phantom was fabricated in order to have a biomimetic structure that could represent the one found in skeletal muscle tissue^{42,43}.

Each of the three samples (firmly positioned into a glass case) was inserted inside a 10mm vertical bore tabletop MR scanner (Researchlab, Pure Devices GmbH, Würzburg, Germany) with a 0.587T permanent magnet and the MRE analysis was performed by means of two diverse actuation modalities: a piezoelectric actuator, that provided axial harmonic vibration to the samples, and a stepper motor actuator, which was able to propagate torsional harmonic vibration.

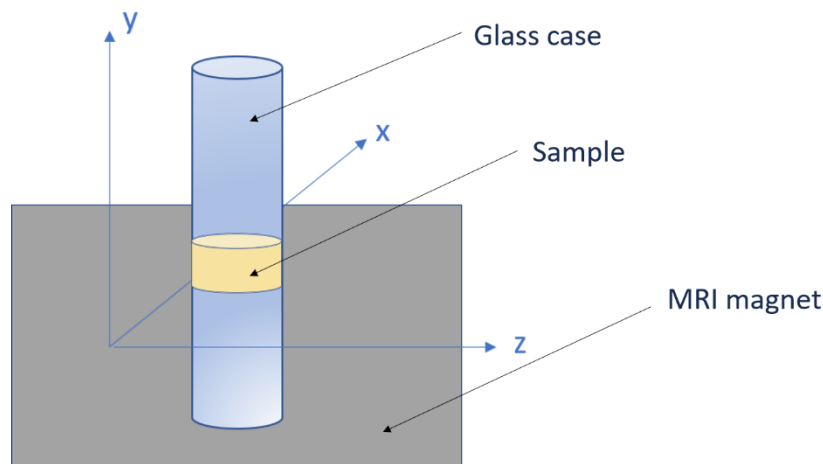


Figure 2.1: Schematic visualization of the UIC setup

Inversion of displacement values found in the wave images, needed to retrieve shear modulus values, was performed differently for each of the samples:

- Homogeneous isotropic gelatin served as a control variable and inversion was immediately performed by directly feeding data from the displacement maps as input inside the DI algorithm.

- As for the mouse sample and the anisotropic phantom, direct inversion yielding the Helmholtz inversion as a theoretical basis was not possible because of the intrinsic anisotropic properties of these two specimens. To be able to employ DI methods, a fictitious isotropy has to be introduced and this has been done by means of application of a novel theory named Transformation Elastography (TE): in this way, wave images get distorted and their reference system switches from a circular to an elliptical one, allowing to have speed and wavelengths of the transmitted waves that are independent on their direction of propagation relative to the fibers' direction inside the phantoms ^{36,38,39}.



Figure 2.2: The examined sample. From left to right: gelatin sample, anisotropic phantom, mouse muscle sample

2.1.2 THE NOVELTY OF THE TORSIONAL ACTUATION

Apart from the implementation of the TE theory onto experimental data, the major novelty that was brought about during experiments at UIC was the introduction of a new kind of actuation. This was provided by means of a stepper motor actuator, able to transmit torsional vibration to the samples.

MRE has proven to be a useful technique that can possibly be beneficial in case of presence of many severe conditions (e.g. neuromuscular disorders)²⁸, being also able to penetrate deeply inside the tissue and to encode motion in all directions⁴⁰; however, it had never been approached from a different perspective, that is to say in the assessment of the response of the tissue to torsional deformation. This response can be detected when using a stepper motor actuator, which is a DC motor that rotates on its axis. The key goal of the research study carried at UIC was to face such modality of excitation, maintaining a constant comparison with the axial excitation modality (given by the piezoelectric actuator). As in the case of axial excitation, vibrations were provided with the “geometric focusing” approach, that is to say starting from the outer boundaries converging to the centre of the phantom.

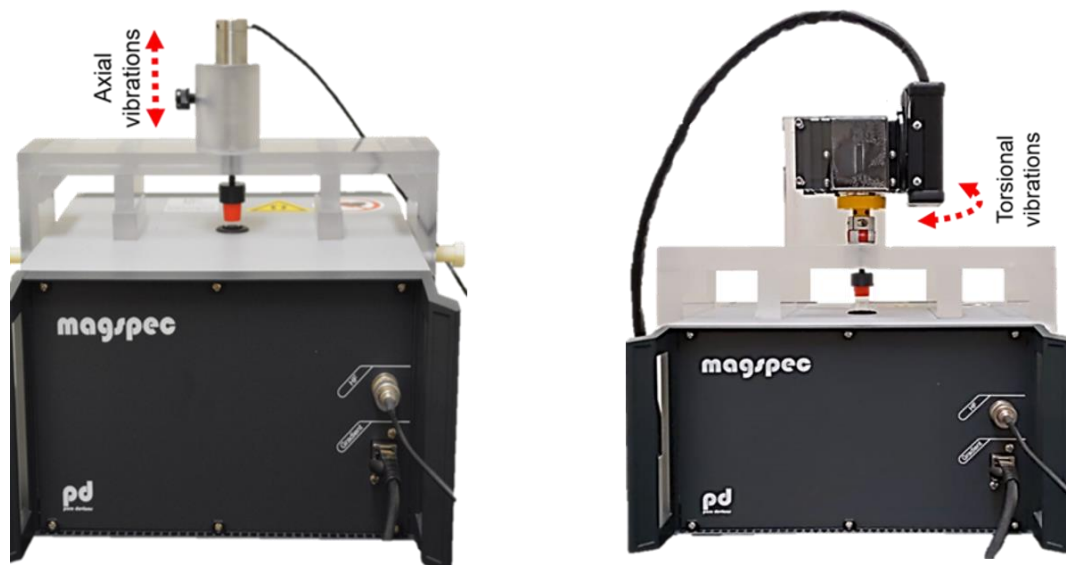
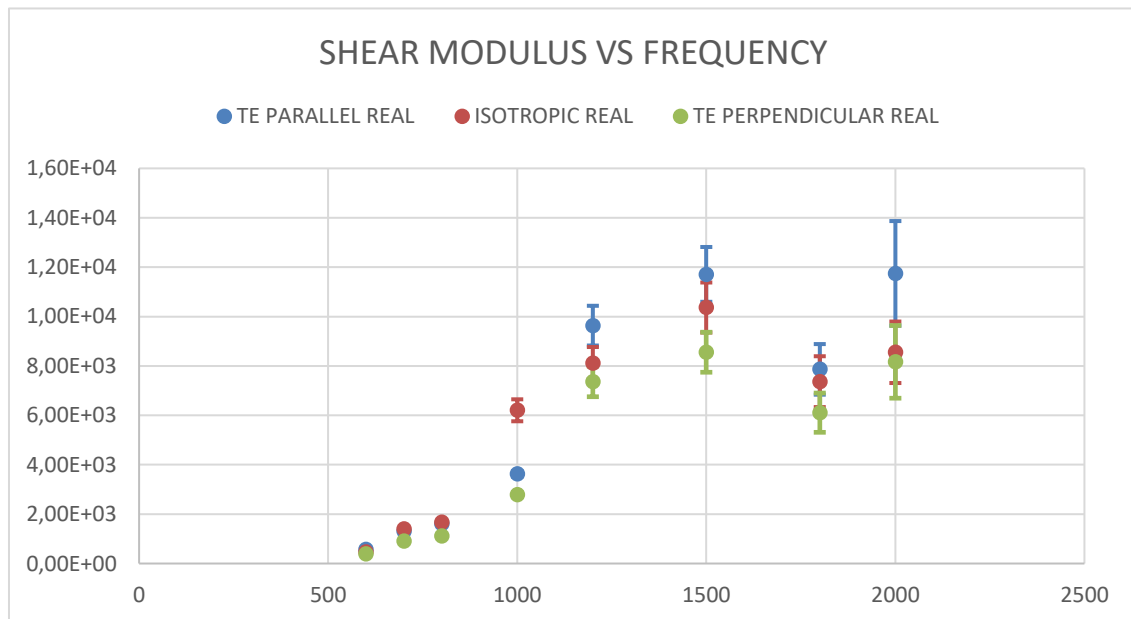


Figure 2.3: Actuator systems. From left to right: piezoelectric actuator and stepper motor actuator

2.1.3 THE RESULTS

Results following experiments done at UIC can be divided into two macro-categories:

- Results given by piezoelectric actuation of the samples: in this first case the analysis started from the implementation of the setup that would provide an axial vibration to the three samples, moving on to the extraction of displacement maps in the form of wave images, and finally reaching the stage of inversion that ultimately led to the extraction of frequency-dependent shear moduli for each specimen. As mentioned before, inversion approaches were different depending on whether the samples were isotropic or anisotropic.



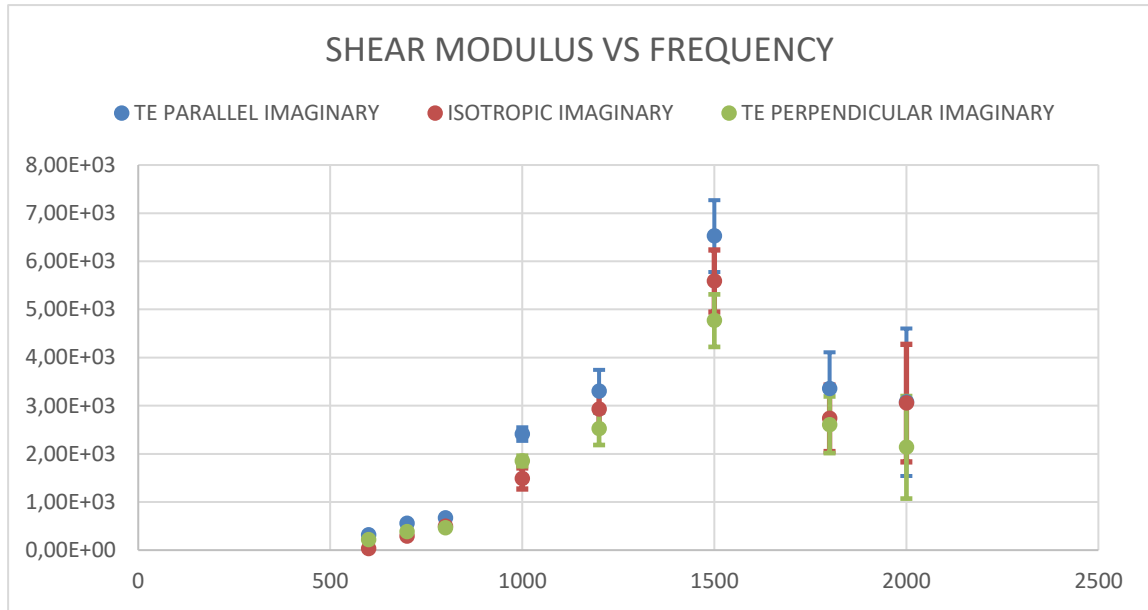


Figure 2.4: Shear modulus trend as a function of frequency for an anisotropic phantom. Double arrows represent standard deviation values. Top: real part; Bottom: imaginary part

- Results given by stepper motor actuation of the samples: as for this case, final stage of the analysis reached the visualization of wave images, while inversion of displacement values was not finalized. As a matter of fact, when applying a torsional actuation perpendicular to the cylinder's axis, fast shear waves get produced, whose velocity values depend on the wave's propagation direction with respect to the axis of symmetry³⁸; thus a geometric distortion is needed as in the previous case and it is given by

$$r(\theta) = \frac{r}{1 + \phi \cos^2(2\theta) + \zeta \sin^2(2\theta)} \quad [2.2]$$

However, the expression for such a distortion requires the presence of a further parameter, named Tensile Anisotropy (marked by ζ), that was not known at the time.

The expression for the tensile anisotropy value is

$$\zeta = \frac{E_{\parallel}}{E_{\perp}} - 1 \quad [2.3]$$

And this could be retrieved by means of mechanical tests directly performed on each sample.

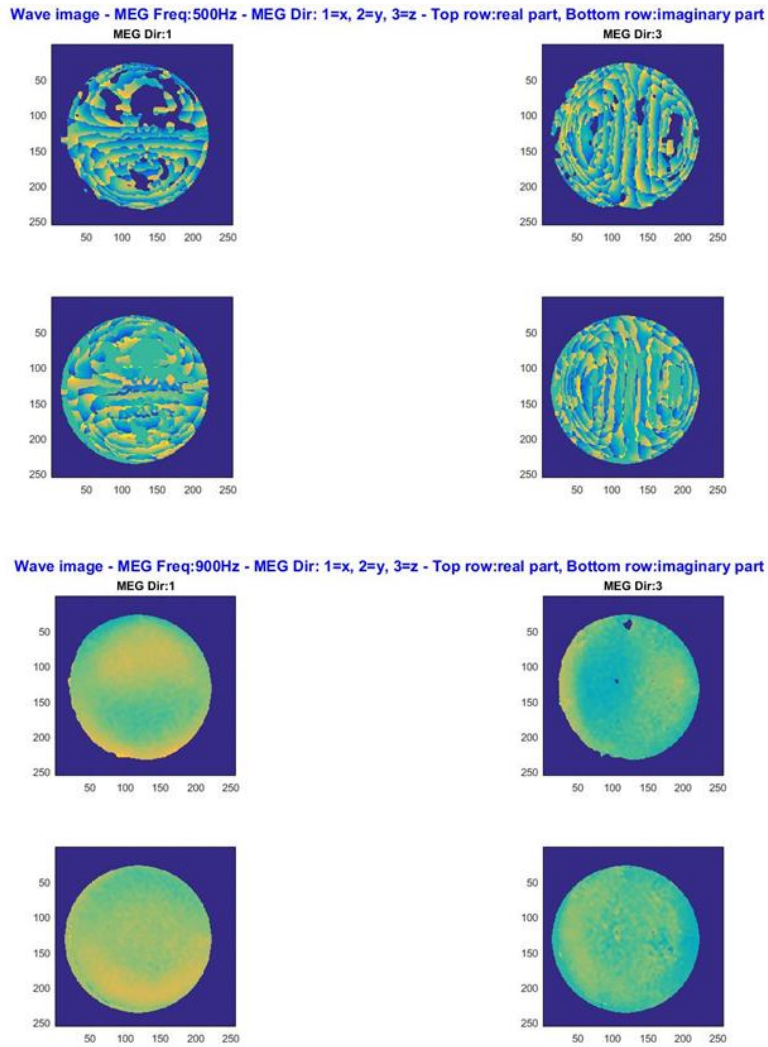


Figure 2.5: wave images for anisotropic phantom after torsional excitation

Top: a)500Hz x direction

b)500Hz z direction

Bottom: a)900Hz x direction

b)900Hz z direction

2.2 STATE OF THE ART AND MOTIVATION FOR THE PRESENT WORK

2.2.1 THE DIRECT PROBLEM

As mentioned in previous chapters, the MRE experimental procedure imposes the transformation from displacement values to mechanical properties: such a transformation yields the presence of an inversion. The inversion procedure, named Helmholtz inversion, has been theoretically presented, still it requires the existence of radical assumptions (of isotropy and homogeneity) that are not feasible in a biological medium, least of all in the skeletal muscle tissue⁵.

For this reason, an alternative approach may result more beneficial in order to better understand the propagation of waves inside a viscoelastic and anisotropic material: this approach aims to reverse the typical MRE procedure and it is thus called “direct problem”. In the direct problem, mechanical properties are given as input to the formulation, rather than found as a result: the obtained outcome, instead, is the extraction of the displacement fields given the mechanical properties of the material.

In this work, mechanical properties are not simply hypothesized, instead they are plugged in the direct problem formulation, starting from the results that were previously acquired with experiments that were held in the Acoustics and Vibrations Laboratory at the University of Illinois at Chicago.

2.2.2 AN EXPLANATORY EXAMPLE REGARDING THE DIRECT FORMULATION

In order to better elucidate what the direct formulation entails an experiment that has been carried out by Yasar et al. will be here presented⁴⁴.

In their experiment, the MRE procedure was applied over a range of frequency that spanned from 200Hz up to 7750 Hz on an Ecoflex phantom, which is a silicon material and was chosen because of its viscoelastic properties able to mimic those of soft tissues.

The used phantom is homogeneous isotropic and cylindrical, the excitation is provided on its outer boundary with a displacement value of $1\mu\text{m}$ and, given the symmetry of the cylinder around its axis, the mechanical properties that were gained as a result of the MRE experiment

were plugged into a 2D computational problem. Eventually this allows the comparison between the experimental displacement fields with those obtained consequently to the simulation.

Figure 2.6 shows a sketch of the applied vibration on the cylindrical phantom, as well as the acquired displacement profiles on the top face of the cylinder at 500Hz along the radial direction⁴⁵

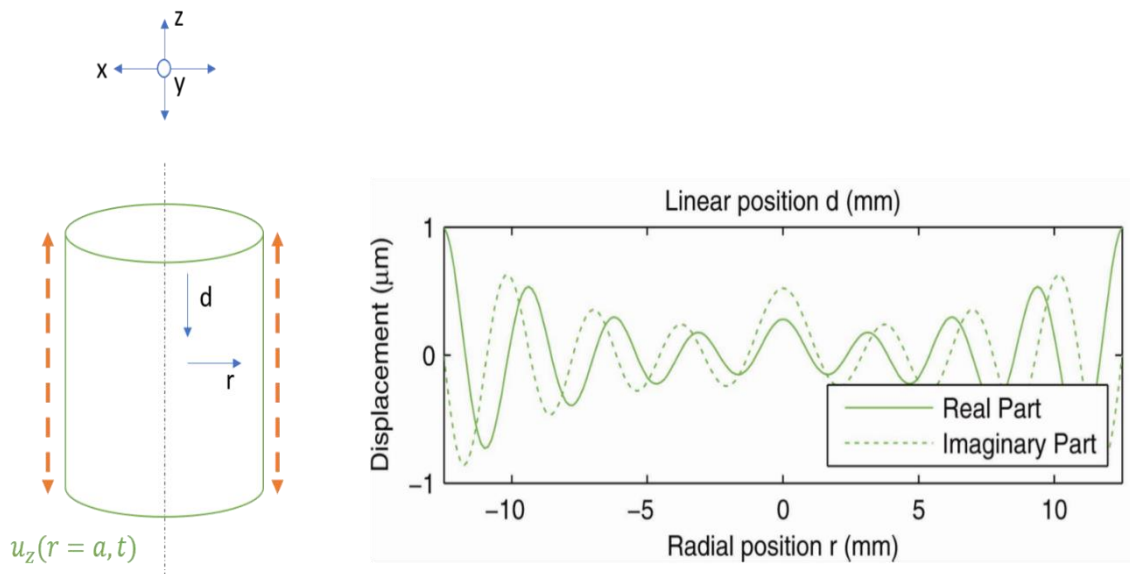


Figure 2.6: (left) sketch of the applied displacement on the outer boundaries of the Ecoflex phantom; (right) displacement profile on the cylinder top surface as a function of radial position. Image re-adapted from Yasar et al.

This experiment shows that the numerical model was able to fit the experimental results in an appropriate way, despite the presence of little inaccuracies and differences between the two that are mainly given by reservations regarding the density value that has to be plugged in the numerical simulation. In this case a value of $\rho=1 \text{ kg/dm}^3$ was chosen applying a somewhat simplifying assumption. Unfortunately, density values give a major contribution to displacement values and little discrepancies with the real values for the density may lead to big errors in the visualization of displacements.

Having said that, visualizing the peak to valley amplitude of the displacement profiles for the simulation and for the experimental results, four valleys and five crests are visible in both

cases, validating the simulation procedure over the experimental results and vice versa (Figure 2.7)⁴⁵.

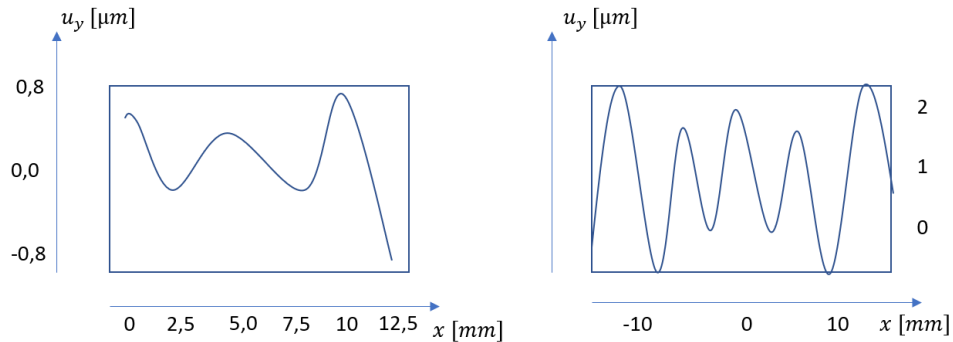


Figure 2.7: Displacement profiles acquired at 1500 Hz of the top surface of the cylinder along the radial direction spanning from -12.5 mm to 12.5 mm (because of axi-symmetry only half path is displayed). (Left) results from the numerical simulation; (right) results from the MRE experiment. Adapted from Yasar et al.

2.2.3 MOTIVATION FOR THIS WORK

Skeletal muscle tissue can be affected by a series of pathologies and severe disorders that may represent a serious threat to the lives and well-being of people: such disorders are usually neurologically related and examples may be given by Duchenne’s muscular dystrophy, spasticity and atrophy. These pathologic conditions come with a structural change of the affected tissue, that may represent an alarm bell for the presence of the disease itself²⁸. It is thus important to be able to monitor the progression of the ailment by tracking changes in the material properties, both from a diagnostic and a successive therapeutic point of view.

The specific aim of this thesis work is to realize a computational finite-element simulation, that would mimic the anisotropic phantom, used during previous experiments at UIC, that in turn was constructed coherently with the fibrous structure of a real skeletal muscle specimen. The simulation follows the rules of the direct problem formulation, having mechanical properties given as input of the problem and visualization of wave images as the result.

The mechanical properties used as input are not simply taken from literature works or inferred on the basis of known real muscle properties, instead they have been directly derived from MRE experiments on the anisotropic phantom and subsequently rearranged in different forms to fit the requests of the simulation software.

This simulation will eventually help understanding the contribution of the material's properties of anisotropy and viscoelasticity on the propagation of the waves in the very same material. Furthermore, it will serve as a source of comparison with the wave images that were extracted during the previous actual experiments and that were later used to extract the very same properties that are now going to be employed as input for the analysis.

After visualization of the computational wave images, conclusions may be drawn on the experimental results obtained at UIC, of course after consideration of the differences in the basic setting of the two works.

3 MATERIALS AND METHODS

The aim of this work is to recreate the geometry and mechanical features of the anisotropic phantom that is currently at the Acoustics and Vibrations Lab of the University of Illinois at Chicago, by means of a computational simulation, that would in turn provide the visualization of the wave displacement inside the phantom, subsequent to the insertion of the mechanical properties gathered from actual experiments.

The computational simulation has been executed by means of a commercial finite element program named ABAQUS (Dassault Systems Simulia Corp., Johnston, RI, USA).

3.1 THE STARTING RVE GEOMETRY: ONE-ELEMENT-THICK CYLINDER

The anisotropic phantom presents a circular cross-sectional area with a radius of $r=4$ mm. It is made up of a biomimetic muscle matrix of Alumisol Soft Plastic (ASP: low hardness, heat-activated silicone) and biomimetic muscle fibers of PDMS (Dow Sylgard 184); the fibers take up 1 cm in length along the height of the cylinder (*Figure 3.1*).



Figure 3.1: Anisotropic phantom

The computational geometry that should represent the one of the anisotropic phantom is a representative volume element (RVE) which is slightly simplified by “cropping” a smaller

slice of the cylindrical MRE phantom: it is a very thin cylinder with a radius of $r=4$ mm and a height of $h=0.66$ mm. The reason for such a reduced geometry is that the mesh will eventually need to have a single element on the cylinder thickness in order to be able to apply periodic boundary conditions on the top and bottom face of the cylinder as shown in *Figure 3.2*.

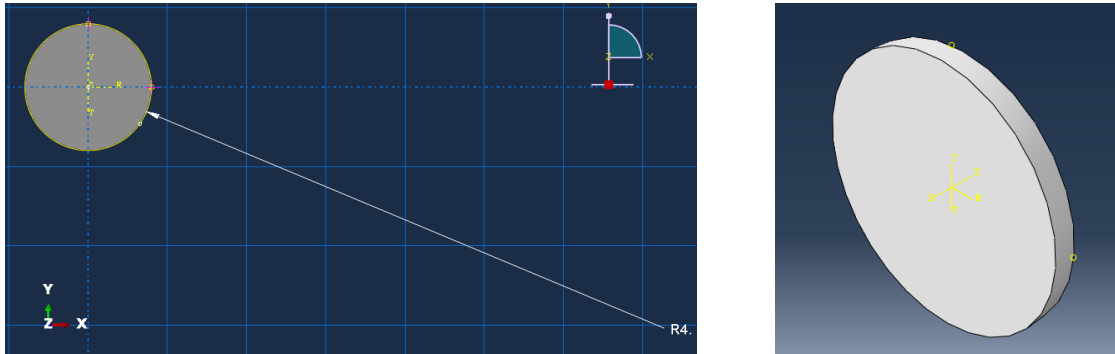


Figure 3.2: Starting RVE geometry

3.2 MECHANICAL PROPERTIES ACQUISITION

3.2.1 A FIRST ATTEMPT: DERIVING GLOBAL PROPERTIES FROM THE SINGLE CONSTITUENTS

ABAQUS requires to plug in the simulation the material properties for the sketched geometry; this is not divided in a twofold manner, having both the fibers and the matrix that are present in the actual phantom. As a first trial, instead, a homogenization procedure has been applied on the geometry which appears uniform. The homogenization is needed in order to derive the global mechanical properties of the composite transversely isotropic material starting from the mechanical properties of the single components (matrix and fibers).

Professor E. Barbero has provided a Matlab code (see Appendix A) that eventually returns the elasticity matrix C for an orthotropic material⁴⁶. This is created starting from the elasticity tensors both for the matrix and the fibers (C_m and C_f) and the fiber volume fraction V_f .

C_m and C_f are obtained by inverting the S matrixes (S_m for the matrix and S_f for the fibers) which have been constructed by including the values of the Young Modulus, the Poisson ratio and the Shear Modulus for the two elements. These have been gathered by prior literature knowledge and both elements have been considered as isotropic ($E_1=E_2=E_3$; $\nu_{21}=\nu_{12}=\nu_{13}=\nu_{31}=\nu_{21}=\nu_{23}=\nu_{12}=\nu_{32}=\nu_{23}$).

Values for the shear modulus have been acquired considering

$$G_{12} = \frac{\frac{E_{12}}{2}}{1 + \nu_{12}} \quad [3.1]$$

And then $G_{13}=G_{23}=G_{12}$.

Once the elasticity tensor C for the whole geometry has been extracted, this gets inverted to the corresponding S matrix and finally values for the Young Modulus, the Poisson ratio and the Shear modulus are acquired for each direction and can be plugged into ABAQUS.

In this first trial, the direction of the fibers has been assumed to be the first direction (x direction), while the cylinder grows in height along the z direction.

Dealing with transversely isotropic materials ABAQUS allows for a specific properties selection which is named Elastic-Engineering constants.

As far as the fiber volume fraction is concerned, this has been calculated taking into account the actual anisotropic phantom geometry.

The PDMS filaments each have a diameter of $d=200\mu\text{m}$ and a length of $l=7\text{mm}$. 16 filaments are placed one next to the other and this is vertically repeated stacking 20 layers of filaments. This leads to a fiber volume (V_{fibers}) of

$$V_{\text{fibers}} = (200 * 10^{-6})^2 * \frac{\pi}{4} * (7 * 10^{-3}) * 16 * 20 = 7.0371 * 10^{-8} \quad [3.2]$$

With a total volume of (V_{tot})

$$(8 * 10^{-3})^2 * \frac{\pi}{4} * 0.01 = 5.02 * 10^{-7} \quad [3.3]$$

The fiber volume fraction is then calculated as the ratio between V_{fibers} and V_{tot}

$$V_f = \frac{V_{fibers}}{V_{tot}} = 0.1399 \cong 0.14 \rightarrow 14\% \quad [3.4]$$

3.2.2 FITTING THE REAL EXPERIMENT TO THE COMPUTER SIMULATION: AN ACCURACY COMPROMISE

Albeit the aforementioned approach allows to provide the computational simulation with the exact properties of the whole material (by homogenizing the properties of its two main components), it lacks in taking into account features that are beyond the Elastic moduli and Poisson's ratios of the phantom: namely the presence of a viscoelastic nature and the necessity of conducting the analysis within a frequency range, to simulate the experiments performed at the University of Illinois at Chicago.

In order to couple all these elements with the already retained experimental results, a Matlab code has been developed: this allows to compare experimental curves, visible thanks to the fitting of UIC experimental results (see Section 2.1.3), with fictitious curves created by the tuning of various viscoelasticity parameters.

An example of such a comparison is hereby provided in *Figure 3.3*.

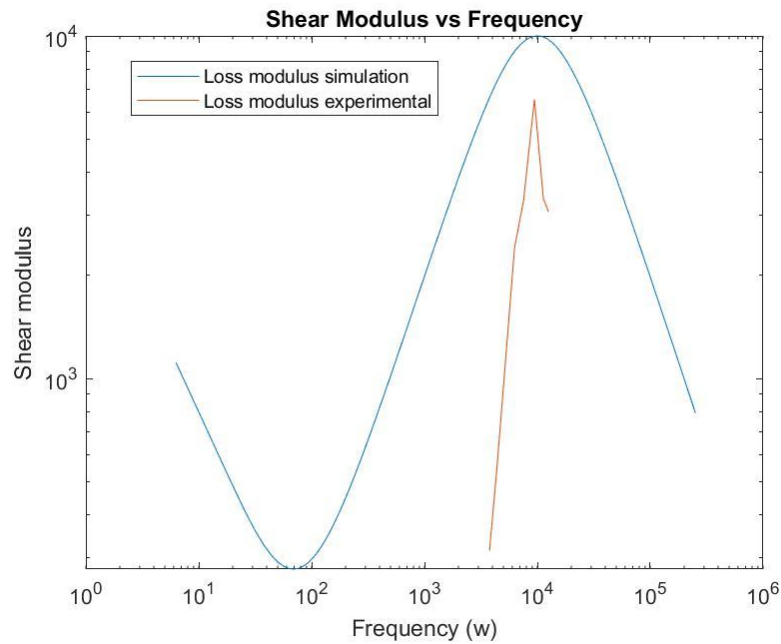


Figure 3.3: Fitting of computational and custom-made results for the loss modulus with actual loss modulus values from experiments held at UIC

Extensive explanation of this methodology with a list of the relative employed viscoelastic parameters will be provided in the following section, while the whole Matlab code will be displayed in Appendix A.

3.3 FREQUENCY DEPENDENT MATERIAL PROPERTIES: TAKING VISCOELASTICITY INTO ACCOUNT

By definition viscoelasticity is the property that a material has when it shows an intermediate behavior between that of an entirely elastic material (only responds to normal deformations) and one of an entirely viscous material (only responds to shear deformations),

thus responding to both normal and viscous deformations. Moreover, the characteristic of viscoelasticity provides a strain rate that depends on time (*Figure 3.4*).

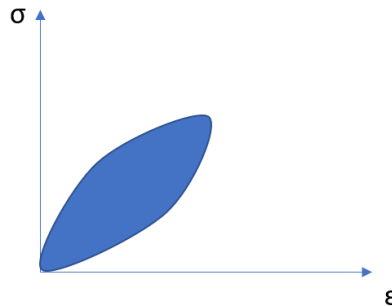


Figure 3.4: Stress-strain curve for a viscoelastic material. The blue area represents the loss of energy between a loading-unloading cycle (hysteresis)

Skeletal muscle tissue is known to be a viscoelastic material and consequently this property affects the way in which waves propagate in the medium; it is, thus, advisable to be taking this aspect into account by performing analyses in a dynamic range of frequencies.

When considering viscoelastic materials, the correspondence principle can be applied: this allows for the transition from an elastic solution (if present) to the corresponding complexed-value viscoelastic solution^{31,47}. Following this reasoning, the shear modulus is represented with its real and imaginary part, the latter accounting for the losses.

$$G^*(\omega) = G_s(\omega) + iG_l(\omega) \quad [3.5]$$

G_s =storage modulus (real part)

G_l =loss modulus (imaginary part)

The finite element modelling program ABAQUS allows to include this further material feature by means of the property tab that possesses tools able to describe the frequency domain viscoelasticity. This describes materials whose behavior is dependent on frequency and that, when undergoing small steady-state harmonic oscillations, are subject to dissipative losses because of internal damping effects.

The frequency dependence can be expressed with different modalities: the one used in this work applies Prony series that give the definition of the storage and loss modulus (G_s and G_l) that depend upon frequency values and that have several parameters as visible hereby⁴⁸.

$$G_s(\omega) = G_0 \left[1 - \sum_{i=1}^N g_i^P \right] + G_0 \sum_{i=1}^N \frac{g_i^P \tau_i^2 \omega^2}{1 + \tau_i^2 \omega^2} \quad [3.6]$$

$$G_l(\omega) = G_0 \sum_{i=1}^N \frac{g_i^P \tau_i \omega}{1 + \tau_i^2 \omega^2} \quad [3.7]$$

N is the number of elements in the Prony series and it is user-defined.

What needs to be plugged into ABAQUS are the different parameters that are visible in equations 3.6 and 3.7, depending on the chosen N value.

These are given thanks to the presence of experimental results of shear storage and loss modulus as a function of frequency that were provided by tests carried out at UIC (see graphs in section 2.1.3) as in *Table 3.1*

The parameters ($G_0, g_1, g_2, g_3, \tau_1, \tau_2, \tau_3$ for $N=3$) are qualitatively retrieved by several trial and error experiments in Matlab (see Appendix A), until the trial curves resemble, having a good fitting, the ones resulting from the experiments (*Figure 3.5 and 3.6*); finally, the parameters are inserted in the property tab in ABAQUS.

Table 3.1: : Parallel and perpendicular shear modulus values using both isotropic assumption and transformation elastography theorem as a function of frequency for an anisotropic phantom

FREQUENCY	PARAMETER	ISOTROPIC ASSUMPTION	ANISOTROPIC RATIO	TE
800	μ^{\perp} REAL	1.68E+03	1.44765	1.11E+03
	μ^{\parallel} REAL	1.68E+03		1.61E+03
	μ^{\perp} IMAGINARY	4.97E+02		4.61E+02
	μ^{\parallel} IMAGINARY	4.97E+02		6.68E+02
1000	μ^{\perp} REAL	6.20E+03	1.3015	2.79E+03
	μ^{\parallel} REAL	6.20E+03		3.63E+03
	μ^{\perp} IMAGINARY	1.49E+03		1.85E+03
	μ^{\parallel} IMAGINARY	1.49E+03		2.41E+03
1200	μ^{\perp} REAL	8.11E+03	1.30705	7.37E+03
	μ^{\parallel} REAL	8.11E+03		9.63E+03
	μ^{\perp} IMAGINARY	2.93E+03		2.52E+03
	μ^{\parallel} IMAGINARY	2.93E+03		3.30E+03

More specifically the steps that were followed are:

- Retrieval of values for the shear loss and storage modulus from experiments held at UIC. These are visible in Table 3.1
- Creation of a scatter plot that relates frequency values in Hertz with shear modulus values in Pascals via the command *loglog*
- Definition of storage and loss modulus as expressed in equations 3.6 and 3.7
- Appointment of random values to the parameters present in equations 3.6 and 3.7. These are chosen in such a way that the computational curve resembles and follows the same path as the experimental curve: an iterative trial and error process is therefore implemented. An example of values is given

$$a = 35000$$

$$g1 = 0.05$$

$g_2 = 0.002$
 $g_3 = 0.5$
 $t_1 = 0.085$
 $t_2 = 0.5$
 $t_3 = 0.00009$

Examples of suitable fitting curves and related parameters are given in *Figure 3.5* and *3.6*

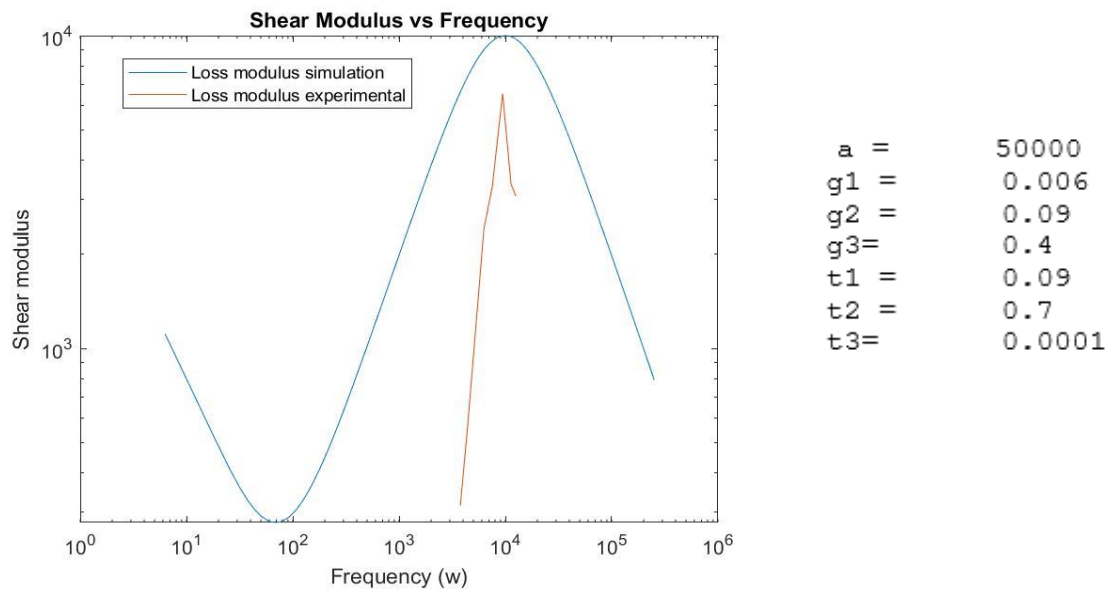


Figure 3.5: Visualization of the experimental curve compared to the computational curve and relative viscoelastic parameters (first example)

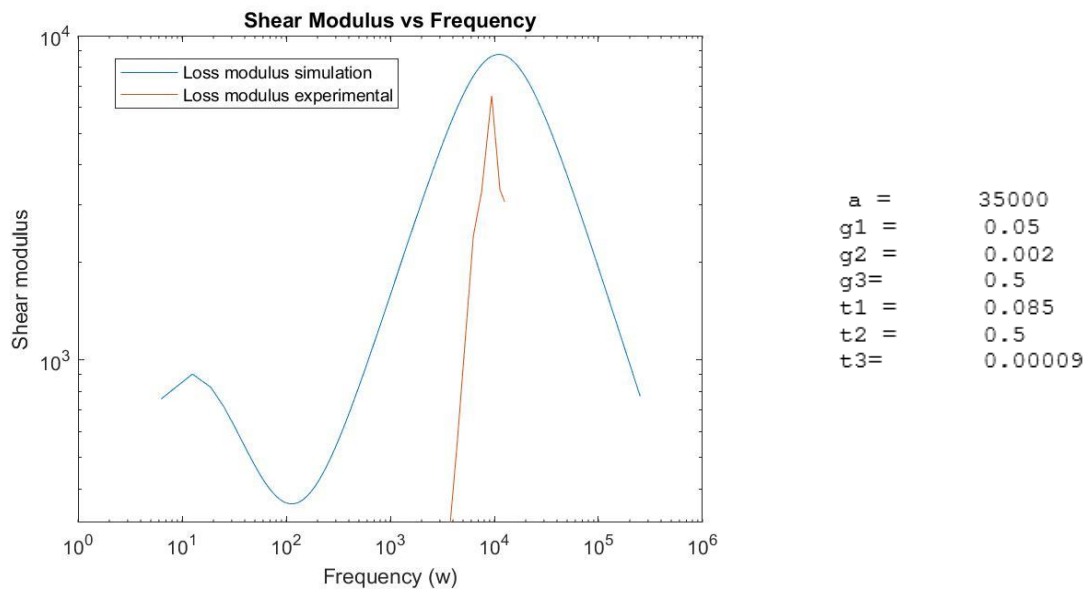


Figure 3.6: Visualization of the experimental curve compared to the computational curve and relative viscoelastic parameters (second example)

3.4 MESHING THE GEOMETRY

A mesh is a collection of geometrical features that define the shape of an object. Since the geometry part present in this study does not represent the whole (in length) anisotropic phantom the constructed mesh must be suitable in order to have a subsequent tool able to provide the “duplication” of the existing RVE as many times as needed to replicate the real geometry.

For this reason, the nodes on the top surface must correspond to the nodes on the bottom surface of the cylinder and only one mesh element must be present along the thickness.

To do so, a partition is drawn on the part: it consists of a little vertical line that connects the two ends of the thickness and it is necessary so that, in the mesh tab, one single node can be set on this feature (*Figure 3.7*).

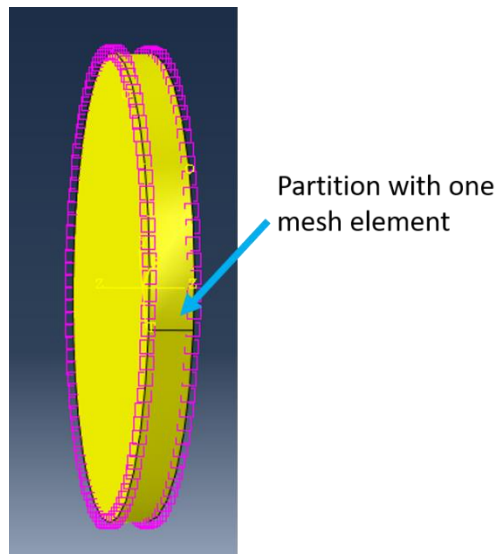


Figure 3.7: Visualization of the nodes distribution along the geometry

Moreover, in order to have corresponding nodes on the two circular faces, the mesh must be neatly organized with the possibility of including symmetry axes and slices on the geometry. In this case the number of seed for the circular boundary was set to 100: the result with matching nodes is visible in *Figure 3.9*

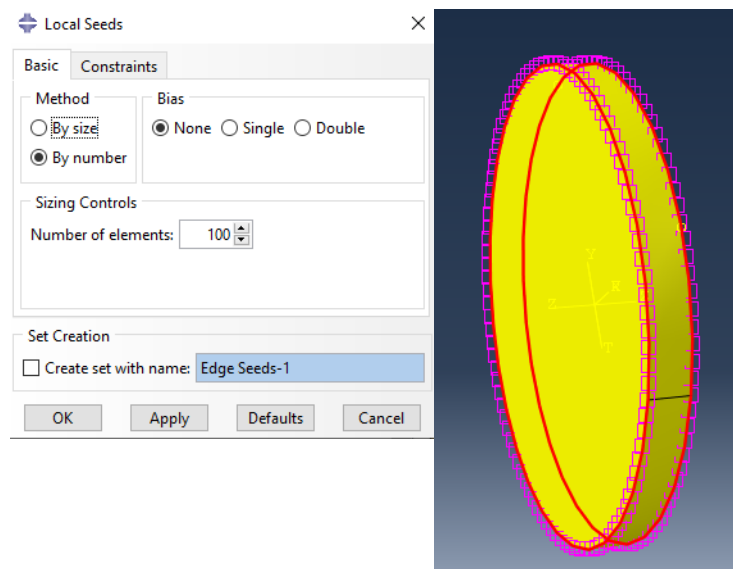


Figure 3.8: Seeds built along the circular boundary

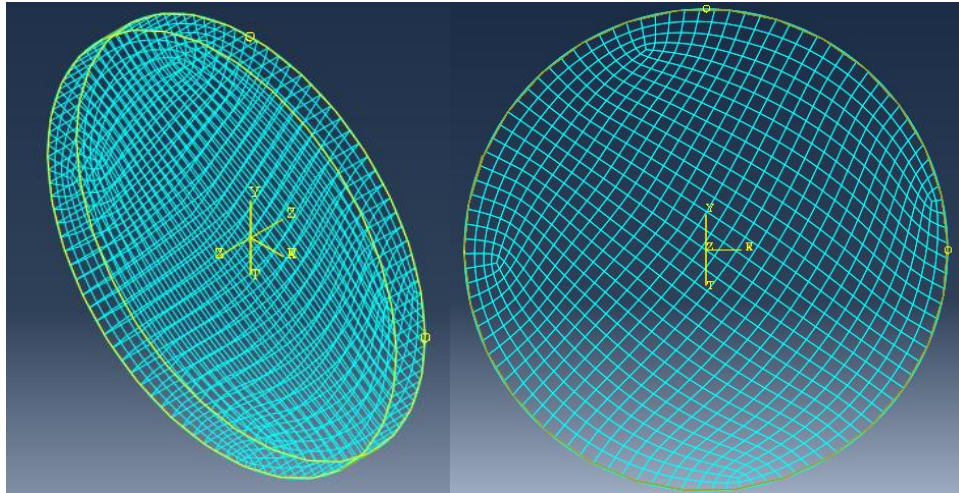


Figure 3.9: (left) 3D visualization of the meshed part; (right) top/bottom face of the meshed parts: it is evident that nodes correspond on the two faces

3.5 HOMTOOLS: APPLYING PERIODIC BOUNDARY CONDITIONS TO THE RVE

As mentioned before, the displayed geometry is simply used to represent the real one used in the MRE experiments (not surprisingly, it is called Reference Volume Element). Despite being effectively representative, a further tool is needed in order to simulate an infinite repetition of the RVE: this is provided by Homtools.

Homtools is a ABAQUS downloadable plug-in which consists in a set of Python scripts that allow to apply periodic boundary conditions (PBCs) to the RVE.

Subsequent to the creation of two reference points (RP-1 and RP-2), the plug-in allows to select the two circular geometries and create the periodicity feature needed to account for the whole real geometry.

The necessary steps are (Figure 3.10):

- Creation of two reference points (RP-1 and RP-2)
- In the Macro Nodes section select first RP-1 and as a second Macro Node RP-2

- In the Boundary Sets section select as a first set the first circular geometry, which is on the bottom face, and as a second set the other circular geometry which is on the top face
- Remove the circular outline of the two circular faces from the entities that are going to be affected by the periodicity condition
- In the Periodicity Vector section only apply periodicity along the thickness of the RVE: in this case $x=0$, $y=0$, $z=0.66$ (depth of the cylinder)

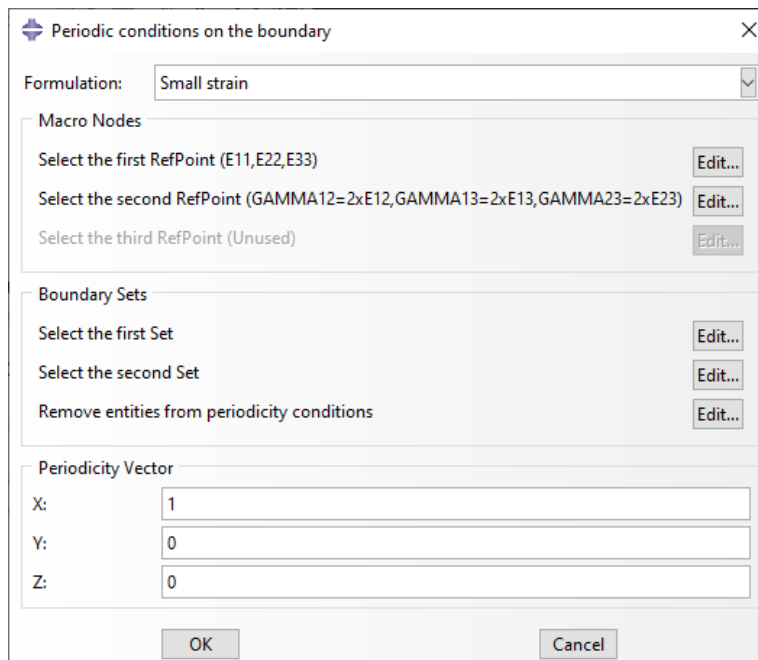


Figure 3.10: Setting procedure for the Homtools toolbox. Each request must be filled as explained in the bulleted list above

In the Interaction tab, under the Constraint Manager selection, periodicity equations for each element of the top and bottom faces are created.

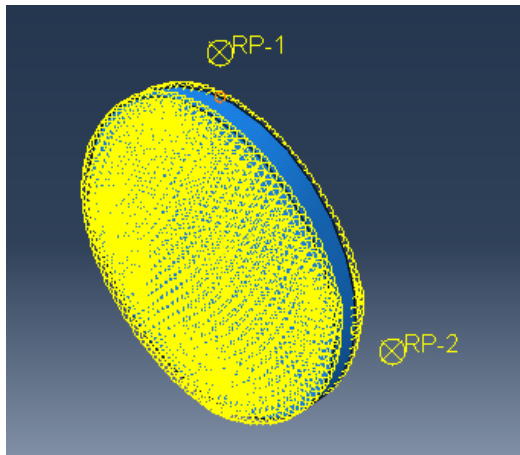


Figure 3.11: Visualization of the geometry after application of periodic boundary conditions (PBCs)

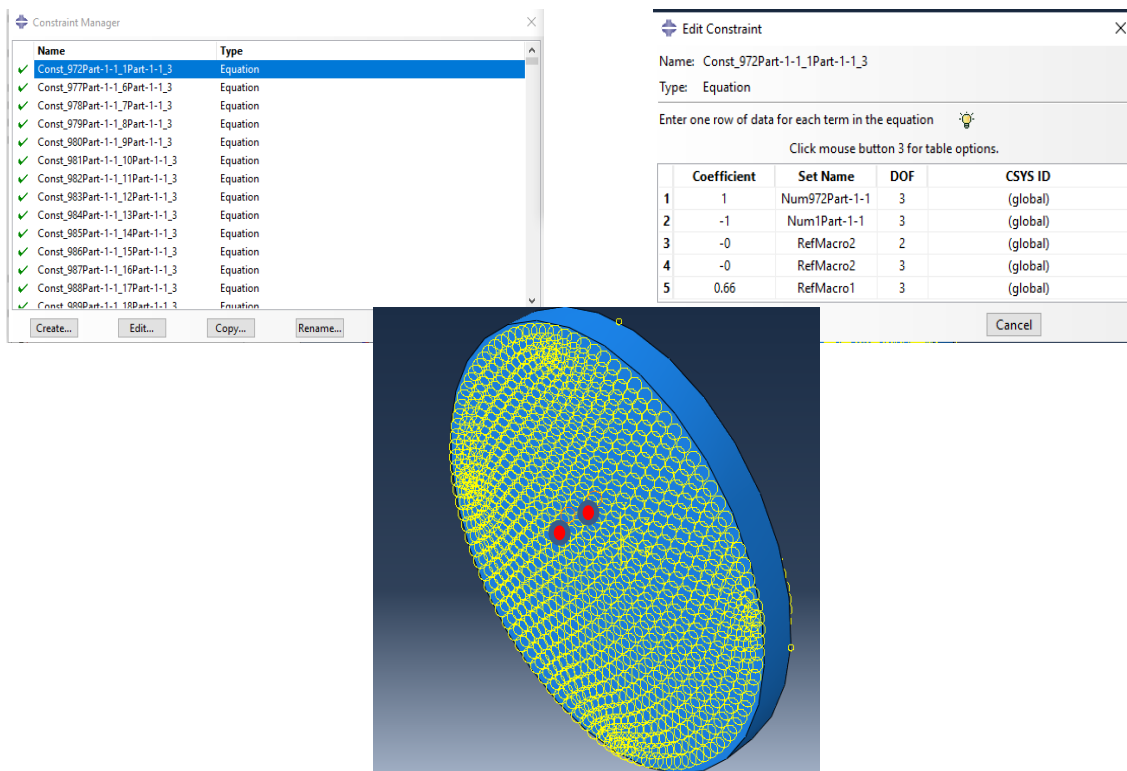


Figure 3.12: (top left) Visualization of the Constraint Manager tab with equations for each point in the top face and its corresponding one in the bottom face; (top right) Detailed explanation of the applied equations for the boundary condition for the single couple of points in the geometry; (bottom) Visualization of the two matching points to which the equations are related (posteriorly highlighted in red)

3.6 LOAD

The applied load is represented solely by the boundary conditions applied on the geometry. This is made possible because of the previous application of periodic boundary conditions by means of Homtools (see section 3.5).

Firstly, on the outer boundary of the cylinder a boundary condition (BC-1) is applied, by imposing the displacements along the first and second direction to be null, while those along the third direction (z) to be equal to $1\mu\text{m}$ (*Figure 3.13*)

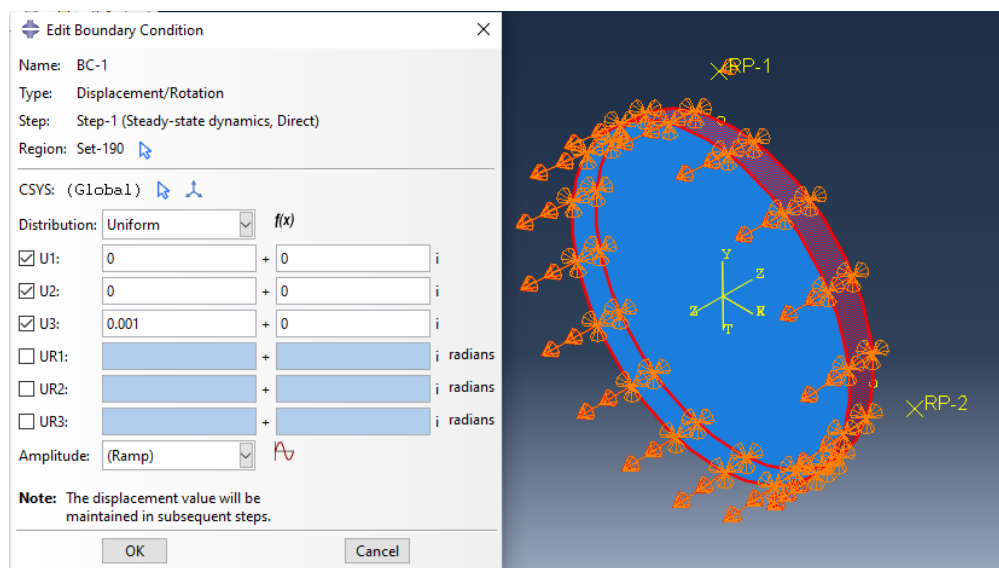


Figure 3.13: Representation of the first applied boundary condition

The second boundary condition (BC-2) is applied on the first reference point (RP-1) that was previously created by means of the Homtools plug-in and its displacement in the z direction is set to 0 (*Figure 3.14*).

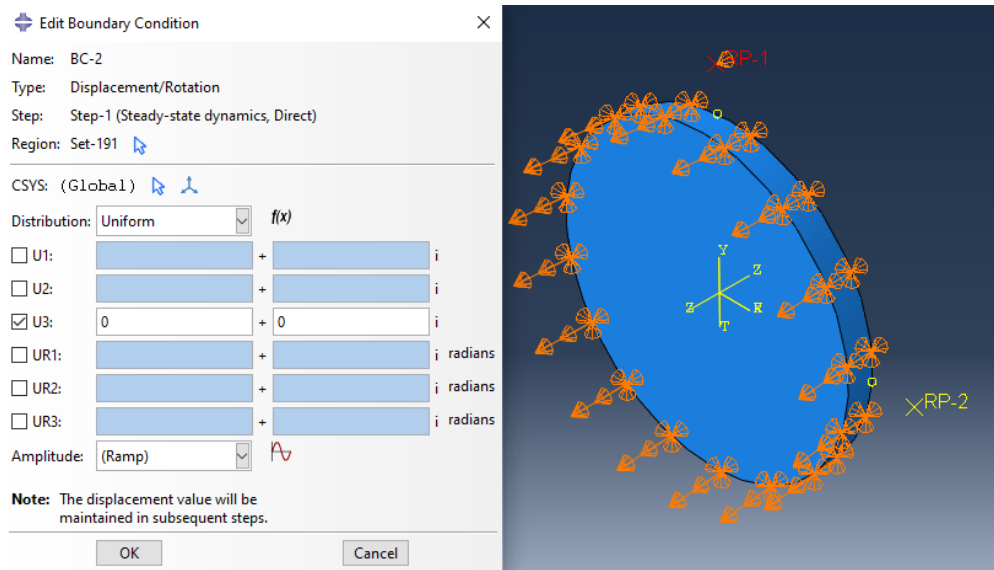


Figure 3.14: Representation of the second applied boundary condition

3.7 DIRECT SOLUTION STEADY-STATE DYNAMIC ANALYSIS

Since the aim of this project is to duplicate and compare experiments already performed at UIC, the applied kind of load of the simulation needs to be coherent to the mechanical stimulation that was proposed for the anisotropic phantom. The stimulation taken into consideration is the one supplied by the piezoelectric actuator that possesses a driver fed with a sinusoidal alternating current: for this reason, following the initial step, a somewhat harmonic stimulation needs to be put in place. This is made possible by the following selection in the Step tab

Create Step → Linear perturbation → Steady-state dynamics → Direct.

Steady-state dynamic analysis allows to evaluate the response of a system subject to harmonic excitation when it has reached the steady state both in amplitude and in phase. The tool able to apply the load at different frequency sweeps is the one given by the direct steady-state dynamic technique.

This tool allows to choose the upper and lower frequencies of actuation and the number of considered points. Moreover, for more than three points, the bias value provides closer

spacing of the results points either toward the middle or toward the ends of each frequency interval with points closer to the ends of the frequency interval with increasing values for the bias parameter.

For the purposes of this work, the lower ever considered frequency has been set to 500Hz while the upper has been set to 2000Hz: when these two frequency values were set as part of a unique experiment, four points between them were taken into consideration in a linear fashion (alternatively a logarithmic spacing between the frequency values can be selected). Alternatively, experiments have been performed iteratively taking into consideration couples of adjacent frequencies. The bias parameter has been held to 1 for each simulation (*Figure 3.15*)

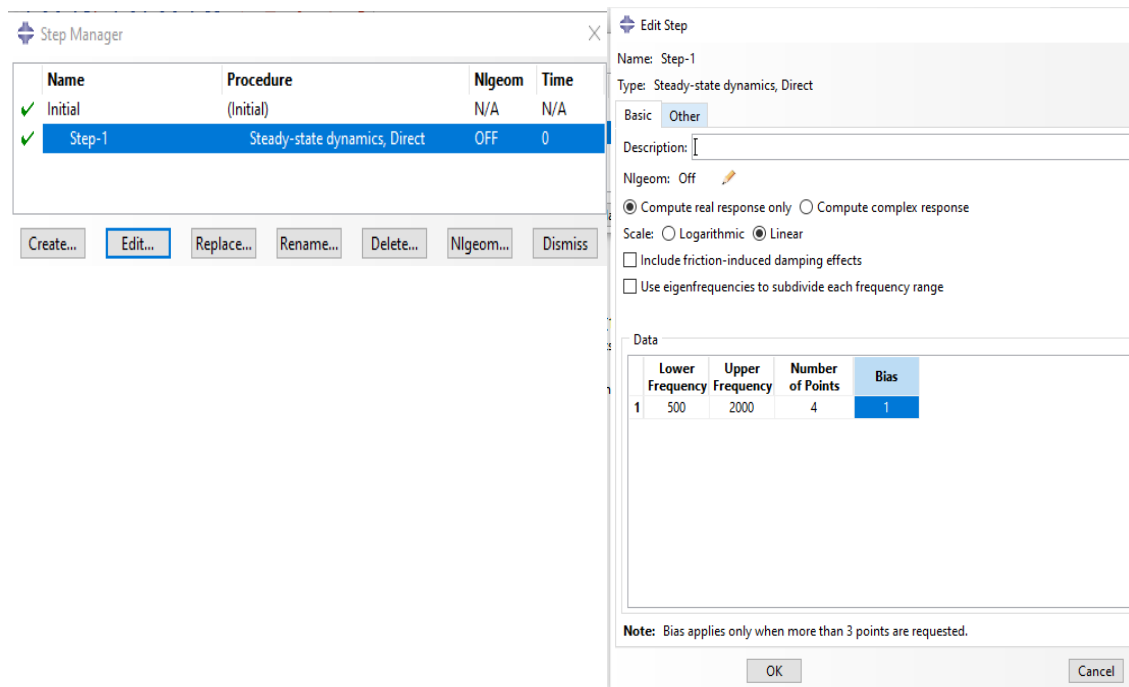


Figure 3.15: Setting of the Step tab in the ABAQUS simulation

3.7.1 IMPLEMENTATION OF THE UMAT USER SUBROUTINE

ABAQUS/Standard in its most basic functionalities does not allow for a variety of applications that could be useful to the user: For our purposes, the computational simulation should be one that combines the presence of viscoelasticity in the material properties with an analysis held in the frequency domain: this is not made possible by means of the basic functionalities held by ABAQUS/Standard; for this reason, the software provides users with an extensive array of user subroutines that allow them to adapt ABAQUS to their particular analysis requirements.

The one that successfully satisfies our requirements is a subroutine called UMAT, which is able to define any complex, constitutive model for materials that cannot be modeled with the available ABAQUS material models⁴⁹.

One particular UMAT is visible in Appendix B and was written specifically to take into consideration viscoelasticity properties as a function of frequency in order to satisfy the relations in equations 3.6 and 3.7 (red underlined section of Appendix B).

Subsequently, ABAQUS is allowed to plug into its property tab those values that are specified in the UMAT subroutine and recalled by means of the function *props*.

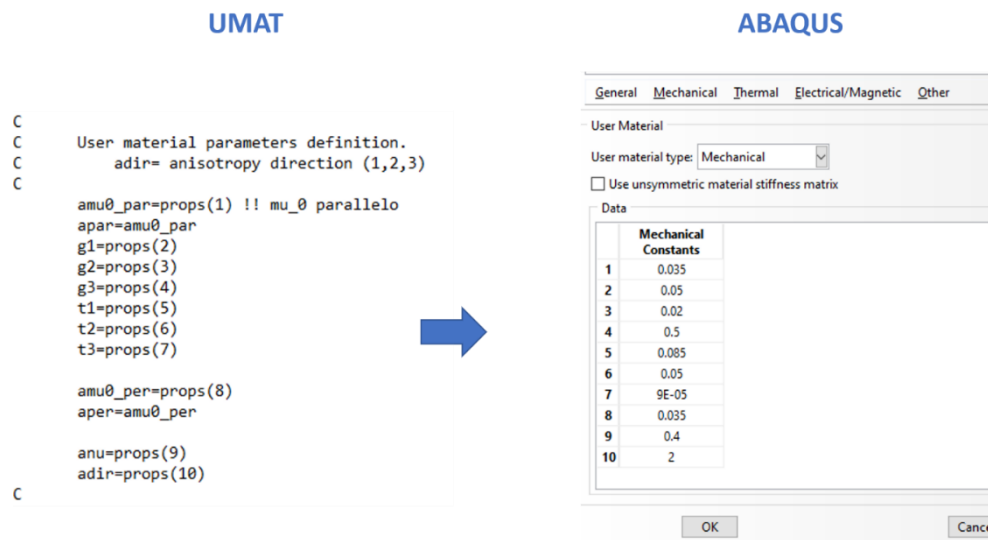


Figure 3.16: Transfer of viscoelasticity parameter, shear modulus and direction values from the UMAT subroutine to ABAQUS property tab

Additionally, the subroutine defines the creation of the stiffness matrix C, the damping matrix D and the stress tensor.

3.8 A BETTER EVALUATION OF DISPLACEMENT IMAGES VIA FOURIER TRANSFORM

Once the ABAQUS simulation is completed, different kind of maps are available to the user: for the sake of this work we are interested in displacement maps that are found under the “Visualization” tab, by selecting “Primary” and subsequently U (u3 since we are investigating displacements in the z direction).

One way to effectively analyze the pattern of displacement inside the anisotropic phantom is given by the use of the 2D Fourier Transform: as a matter of fact, spatial changes inside an image (occurring both in the x and y direction taking the cross-sectional area) can be better characterized by 2D spatial frequencies and the 2D Fourier Transform is a useful tool to determine the relation between the intrinsic anisotropy of the material and its response to forced external deformation given by the MRE experiment³¹.

This approach is based on the extraction of local wavenumber from the displacement wavefields that result from the MRE experiment via Local Frequency Estimation (LFE); this methodology allows to avoid taking into consideration the equations for wave motion in order to perform an inversion, that yields the extraction of mechanical parameters.

LFE ground basis is the relation between the wave speed and the wavenumber k

$$c = \frac{\omega}{k} \quad [3.8]$$

In the case of fibers aligned along the in-plane direction, harmonic excitation and out of plane displacements, shear waves propagate with speed described as

$$c^2 = \mu_l \cos^2(\vartheta) + \mu_t \sin^2(\vartheta) \quad [3.9]$$

Which from equation 3.8 yields

$$\frac{\omega^2}{k^2} = \mu_l \cos^2(\vartheta) + \mu_t \sin^2(\vartheta) \quad [3.10]$$

Where μ_l is the shear modulus parallel to the fibers, μ_t is the shear modulus perpendicular to the fibers, θ is the angle between propagation direction and fibers' axis and ρ is density.

Once the value for the wavenumbers k has been extracted by Fourier Transform (in this case with the methodology explained below), it is fed to equation 3.10 to obtain the values for μ_l and μ_t ⁵⁰.

The 2D Fourier Transform will be applied via a Matlab code and the resulting k-space images will be compared to the displacement images given by the simulation.

In order to perform this task, further intermediate steps are necessary: this requires the use of a Python script (see Appendix B) that is able to read the .odb file (output database) coming from the ABAQUS simulation that contains the output data from the analysis.

3.8.1 SPLITTING THE GEOMETRY IN A QUARTER SEGMENT

In view of the last step that yields the visualization of displacement in the form of Fourier maps, one could argue that a thicker mesh needs to be seeded onto the geometry in order to better visualize peaks in the Fourier transform.

Unfortunately, this does not seem to be possible on the existing geometry, because of the constraint of having an exact match of nodes on the two in plane faces. For this reason, the circular geometry has been split into four triangular slices and consequently meshed.

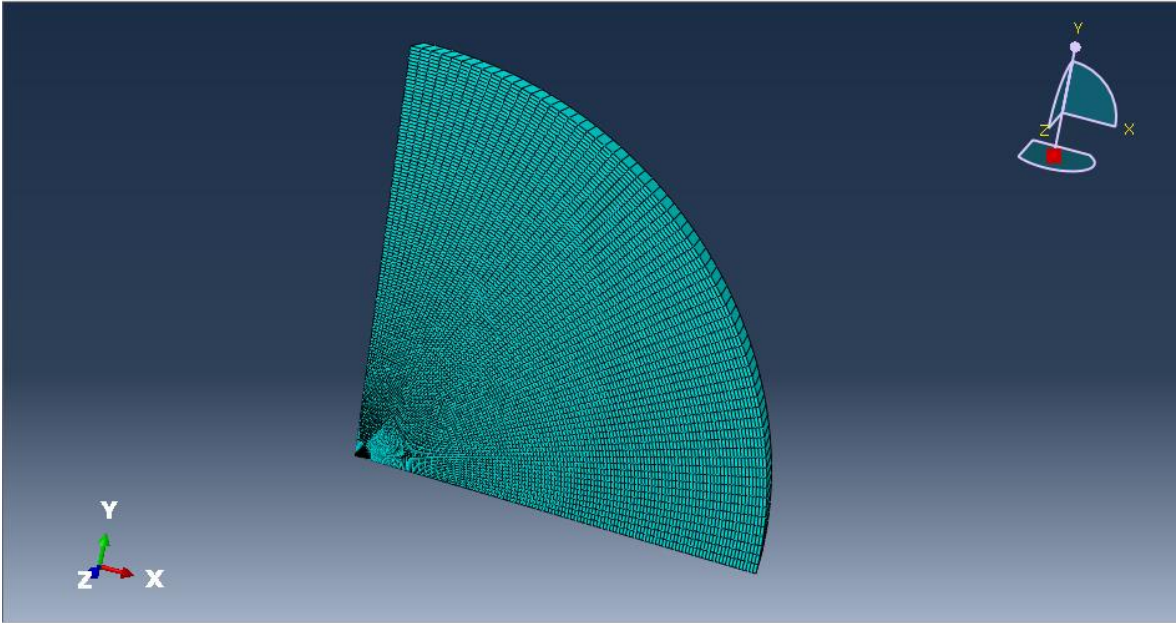


Figure 3.17: Slice of the global geometry that corresponds to $\frac{1}{4}$ of the total, meshed with a higher number of seeds.

This shrunk geometry maintains the very same features of the bigger geometry, that is to say properties that are inserted in the “Mechanical constants” tab via the UMAT subroutine, a steady state dynamic step and a load with boundary conditions and periodic boundary conditions as those used for the complete circular figure.

Once the geometry has been redefined and the mesh made more crammed, one can proceed with the extraction of values for the coordinates and the displacement data of the smaller slice via the Python code.

The Python file “disp.py” contains a series of commands:

- The .odb file for the desired simulation is imported and accessed
- The main features of the .cae file are extracted and introduced into the Python code: this includes the time frame, the coordinates and the displacement data
- Two text-based documents are created: the first one named “coord.txt” contains the x, y and z coordinates for each node of the geometry under examination; the second one named “tryout.txt” contains the displacement values in the x, y and z direction for each node of the geometry
- The values for the coordinates and the displacements are visible via PuTTY, a serial console interface

Once the text files have been extracted from the simulation output, these are imported in two Matlab sequences (see Appendix A: the first sequence has been named “mirroring” because it implements the duplication of the sliced geometry in the vertical and horizontal direction: in this way, all for slices, that compose the whole geometry, are meshed equally and with many more seeds than in the original setup, which allows for more detailed analyses. Importing of x, y and z coordinates, in addition to displacement data in the z direction (coming from the text files) is required to correctly launch the code. Data from the text file is altered depending on the anisotropy direction (whether the laying direction for the fibers is along the x or y coordinate), consequently two couples of text files are present when the simulation is performed considering both directions for the anisotropy.

The user needs can extract values for the coordinates in all three directions, by taking all the values along the rows and in turn the second, the third and the fourth column of the coordinates matrix, to account respectively for the x, y and z direction. The same extraction is done for displacement values in the z direction, this time taking items along all the rows and along the fourth column of the displacement matrix. This is feasible by Matlab commands.

The outcome of this first Matlab code is the retrieval of x and y coordinates for the entire circular geometry, in addition to its displacement values in the z direction. Moreover, the code creates a Matlab mesh for the entire circular geometry after fitting the surface by means of the “griddata” command, in which the meaningful scattered parameters to be interpolated to produce gridded data are

$$u_{3r} = f(x, y) \quad [3.11]$$

Where u_{3r} represents the displacement in the z direction for the smaller slice, while x and y represent x and y coordinates of the smaller slice.

Once the values for the z displacement of the whole geometry have been fetched, these are fed into the second Matlab sequence that implements the 2D Fourier Transform.

The code creates a regular grid onto which data from displacement, relative to the nodal coordinates, are organized, by taking into consideration the need for a compromise value

between xmax and dx in order to ultimately have logarithmic scale images with a narrow coordinates' values range while keeping an acceptable level of visibility of the image itself.

Finally, a 2D Fast Fourier Transform (FFT) is performed and the k-space for the images of displacement is acquired. The k-space can be defined as the spatial frequency information for an image (in our particular case) in terms of space, which is occupied by frequency and phase encoding data⁵¹. In this representation the position for each pixel corresponds to the wavelength while the color intensity is related to the wave amplitude.

What could ideally come from the logarithmic Fourier maps is ratio between the two direction, that could be compared to the anisotropic mechanical ratio fed into the Abaqus simulation.

Furthermore, this kind of evaluation could benefit from the increase in the density value for the material: as a matter of fact, the idea of using the Fourier Transform is to visualize clear elongated peaks in the map; sometimes these peaks are not visible in the standard configuration because of too high wavelength values. To that end, different measures can be adopted such as increasing frequency of actuation or increasing density. The latter has been embraced following the relations

$$\lambda = \frac{c}{f} \quad [3.12]$$

And

$$c^2 = \frac{\mu}{\rho} \quad [3.13]$$

Thus

$$\lambda = \sqrt{\frac{\mu}{\rho}} * \frac{1}{f} \quad [3.14]$$

$$\lambda \cong \frac{1}{\sqrt{\rho}} \quad [3.15]$$

This means that, in order to halve the wavelength, the density ρ must be increased x4 times. Trials have been made with values of density multiplied by 4 and by 9.

The whole process is outlined in Figure 3.18
Error! Reference source not found.

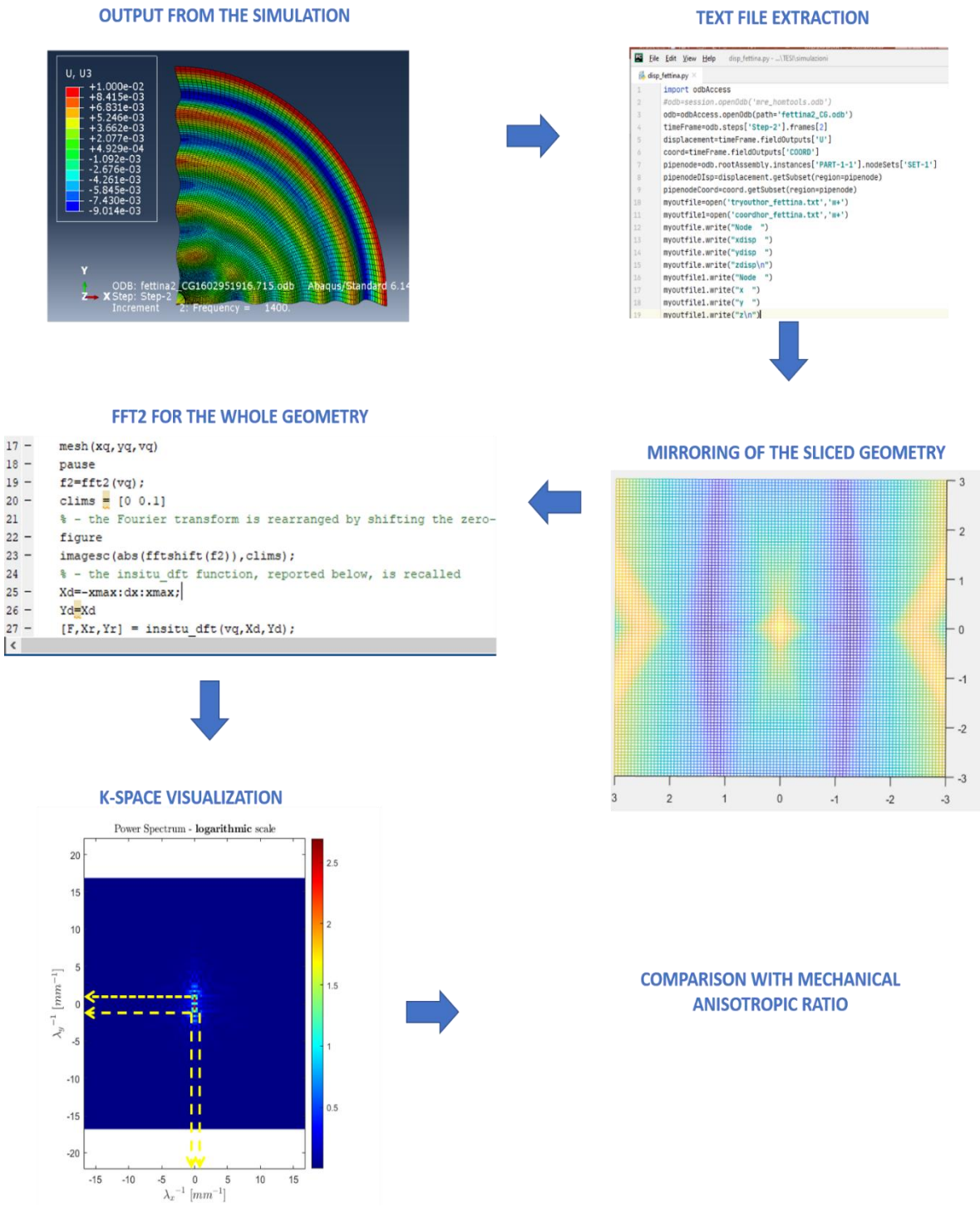


Figure 3.18. Outline of the process that, starting from the output database given by the ABAQUS simulation ultimately allows the extraction of the k-space, via a Python and Matlab cod

For the sake of visualization of displacement data, this smaller geometry can be mirrored twice in order to recreate the initial circular geometry, this time having a thicker mesh. This can be done in the Visualization tab by selecting View → ODB Display Option → Toggle on the the XZ and YZ planes, needed to copy the model results.

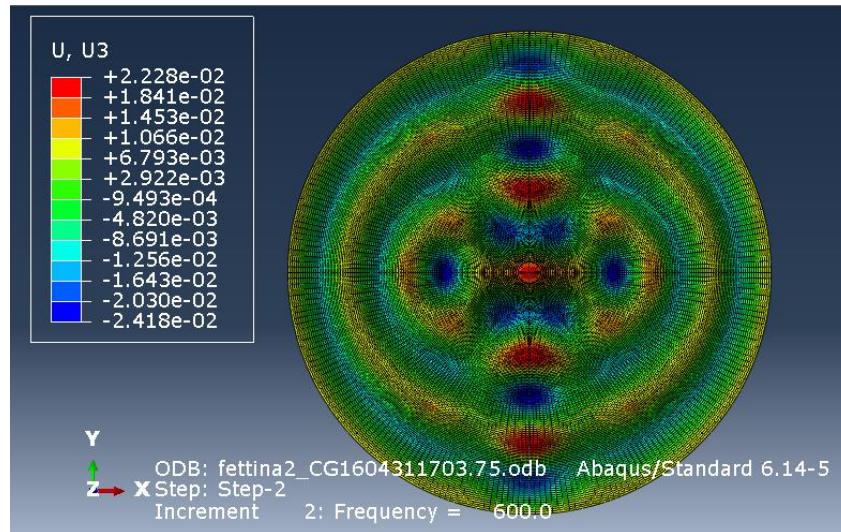


Figure 3.19: Visualization of the smaller geometry after mirroring operation. Picture arising from the 3rd simulation at 600Hz with an anisotropic ratio of 0.5

3.8.2 WAVE NUMBER VS. ANISOTROPIC RATIO: A QUANTITATIVE COMPARISON

The Matlab sequence provides the user with a final power spectrum map that displays the wave numbers in the x and y direction as axes, while the color intensity is related to the mean square amplitude of the wave.

To have a more quantitative evaluation of these maps, one could create plots displaying the power density value on the y-axis and the value of λ^{-1} for both directions on the x-axis.

This could be visualized either by a 2D plot or a 3D plot, by means of a surface.

The application of the Fourier Transform has a result the creation of a matrix of 101x101 complex-valued elements. Such elements are the values of the power density for each point in space. In order to visually analyze them, their complex nature has to be somewhat simplified. For this reason, for each matrix element, its absolute value is computed. Furthermore, the Fourier Transform gets shifted so that the zero-frequency component goes to the center of spectrum.

To create a surface from the Fourier Transform matrix the lines computed in Matlab are:

$$f2shift = abs(fftshift(f2)) \quad [3.16]$$

$$surf(f2shift) \quad [3.17]$$

where $f2$ is the matrix resulting from the Fourier Transform.

A visual representation of such surface may be given by *Figure 3.23*

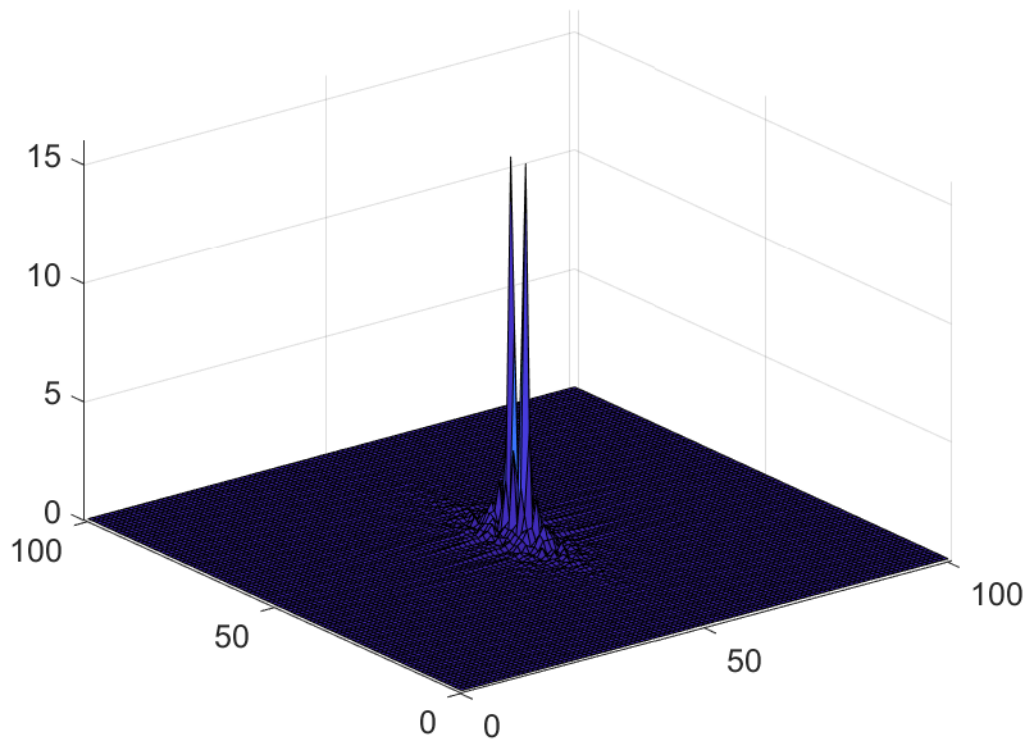


Figure 3.20: Example of surface created from the evaluation of the Fourier transform matrix. A_x^{-1} and A_y^{-1} lay on the in-plane axes, while the vertical axis represents the power density

Alternatively, this very same surface could be differently visualized in this way: by means of a 2D “flattening” on the two planes, followed by a superimposition of the results.

Matlab allows to do so by computing:

```
plot(f2shift(51,:))  
hold on [3.18]  
plot(f2shift(:,51))
```

The parameter set to a value of 51 was chosen because of the shifting of the zero -frequency component to half of the spectrum (101x101 matrix).

An example of this type of plot is provided in *Figure 3.24*

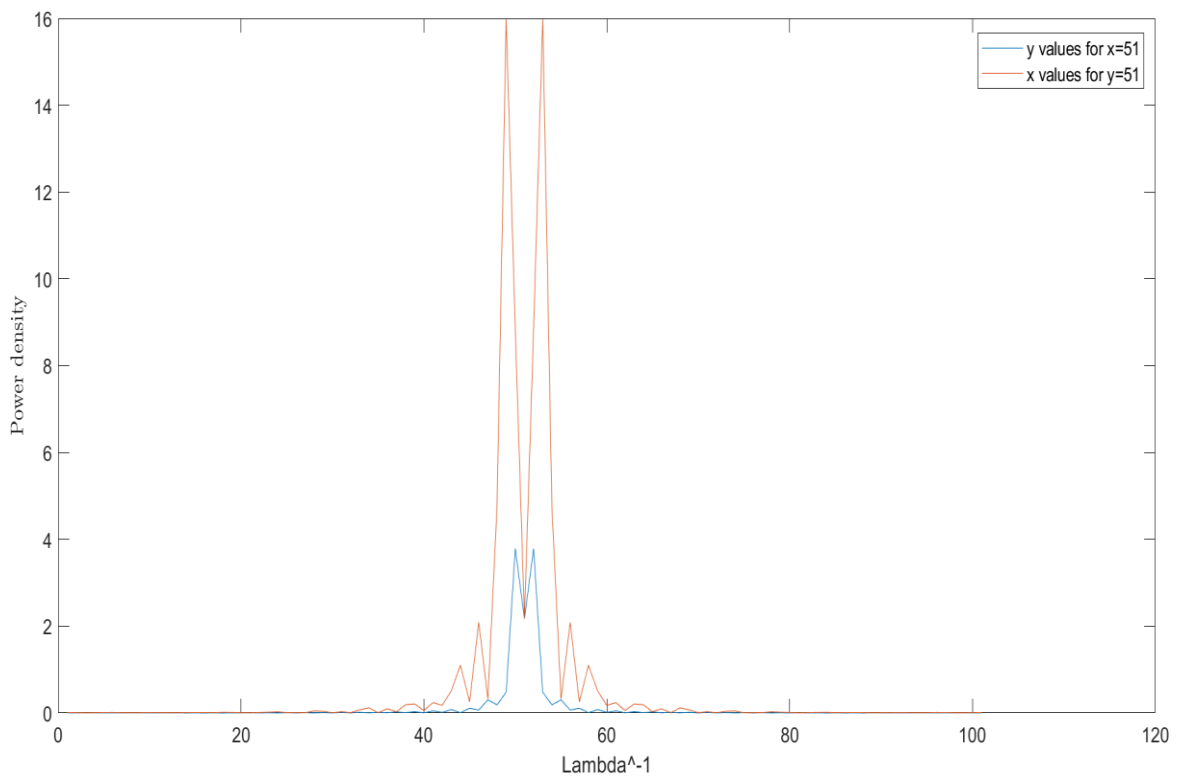


Figure 3.21: Power density as a function of λ^{-1} for both x (red line) and y direction (blue line)

This kind of visualization, repeated for different fibers' volume fraction values (i.e. anisotropic ratio values), allows for a numerical distinction between different degrees of anisotropy, by computing the value of the power density for the same value of λ_x^{-1} and λ_y^{-1} . The creation of such plots represents the first step towards the implementation of the LFE technique (see Section 3.8). As a matter of fact, the quantitative visualization of λ^{-1} values yields to the extraction of the k parameter by means of the equation

$$k = \frac{2\pi}{\lambda} \quad [3.19]$$

Which by means of simplifications leads to the extraction of the shear modulus

$$\mu = \frac{\omega^2 \rho}{k^2} \quad [3.20]$$

3.9 BYPASSING THE PROPERTIES FITTING: A MORE PUNCTUAL ASSESSMENT OF THE WHOLE PROCESS

As visible in paragraph 3.2.2 the properties that are inserted in the Abaqus simulation result from a Matlab fitting that is not able to perfectly match the experimental curves.

As a result of this, displacement images sometimes show several modes of vibrations, instead of a single radial one and are not always relatable to the experimental displacement images. For this reason, a further trial has been put in place, which consists in directly taking values of shear moduli from the UIC experimental results and conducting FE simulations at each frequency matched to the corresponding chosen value.

This approach allows for a better visual comparison of displacement maps between the simulation and the experiment. However, it compels the user to execute one analysis at a time, instead of having a high range of exploitable frequencies for the same set of properties.

Table 3.2: Results of shear moduli from UIC experiments

FREQUENCY (Hz)	PARAMETER	TE (Pa)
600	μ^{\perp} REAL	3.89E+02
	μ^{\parallel} REAL	5.69E+02
	μ^{\perp} IMAGINARY	2.16E+02
	μ^{\parallel} IMAGINARY	3.15E+02
700	μ^{\perp} REAL	9.10E+02
	μ^{\parallel} REAL	1.31E+03
	μ^{\perp} IMAGINARY	3.85E+02
	μ^{\parallel} IMAGINARY	5.55E+02
800	μ^{\perp} REAL	1.11E+03
	μ^{\parallel} REAL	1.61E+03
	μ^{\perp} IMAGINARY	4.61E+02
	μ^{\parallel} IMAGINARY	6.68E+02
1000	μ^{\perp} REAL	2.79E+03
	μ^{\parallel} REAL	3.63E+03
	μ^{\perp} IMAGINARY	1.85E+03
	μ^{\parallel} IMAGINARY	2.41E+03
1200	μ^{\perp} REAL	7.37E+03
	μ^{\parallel} REAL	9.63E+03
	μ^{\perp} IMAGINARY	2.52E+03
	μ^{\parallel} IMAGINARY	3.30E+03
1500	μ^{\perp} REAL	8.56E+03
	μ^{\parallel} REAL	1.17E+04
	μ^{\perp} IMAGINARY	4.77E+03
	μ^{\parallel} IMAGINARY	6.52E+03
1800	μ^{\perp} REAL	6.11E+03
	μ^{\parallel} REAL	7.86E+03
	μ^{\perp} IMAGINARY	2.60E+03
	μ^{\parallel} IMAGINARY	3.35E+03

2000	μ^{\perp} REAL	8.17E+03
	μ^{\parallel} REAL	1.17E+04
	μ^{\perp} IMAGINARY	2.14E+03
	μ^{\parallel} IMAGINARY	3.07E+03

Starting from Table 3.2, one value of shear modulus is chosen: in this work the highest value was selected, which corresponds to a frequency of 1500Hz.

Subsequently the UMAT subroutine needs to be modified by commenting the lines which provide the definition of the shear moduli, through the use of several parameters (green underlined section of Appendix B), and the actual values of shear moduli simply get typed in. Everything related to the commented formulas in the UMAT subroutine will simply be disregarded in the Property Tab of the Abaqus simulation.

In order to compare different anisotropic ratio values the parameter that needs to be alternated is amuR_per .

Subsequently, the analyses conducted thus far for other simulation settings can be replicated in this particular case.

4 RESULTS AND DISCUSSION

4.1 VARYING FIBERS MECHANICAL PROPERTIES: APPLYING DIFFERENT MATLAB FITTINGS TO THE EXPERIMENTAL DATA

The material's different reactions to the external application of a harmonic impulse is determined by the properties that are a priori inserted as input of the ABAQUS simulation. As mentioned before, these properties need to take into consideration the anisotropic and viscoelastic nature of the material whilst adapting the simulation to the frequency domain. This is made possible via the Matlab code (see Appendix A) that implements the equations (3.6 and 3.7) that relate the shear modulus values to the angular frequency ω . Five different trials have been recorded each of which presents different values for the viscoelasticity parameters that compose the equations 3.6 and 3.7. Five simulations are shown below: each presents different values for G_0 (a), g_1 , g_2 , t_1 , t_2 , t_3 along with the plots of the simulation curve compared to the experimental curve.

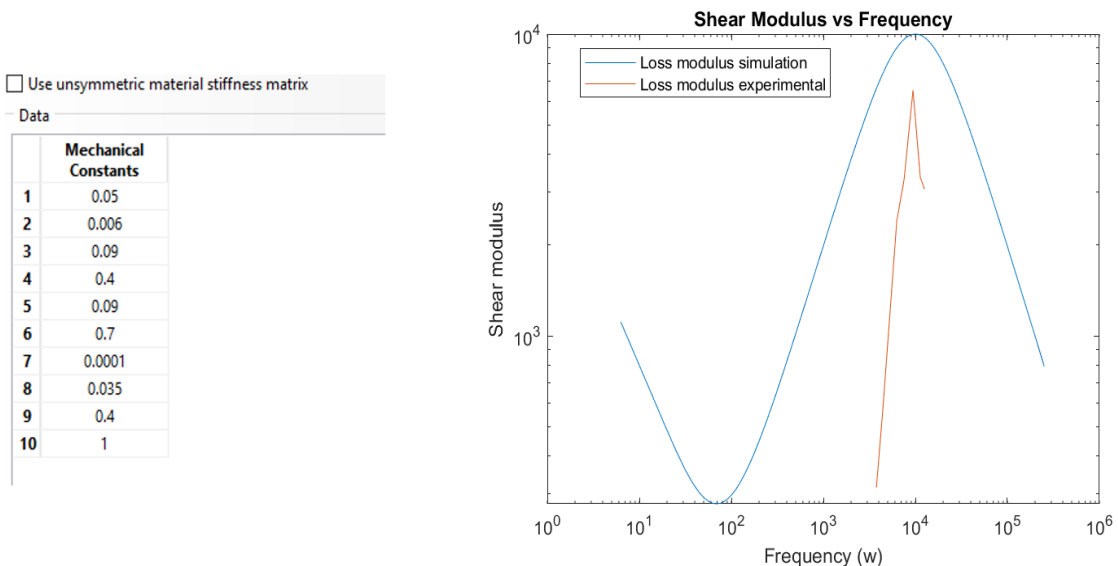


Figure 4.1: First simulation: (left) the first seven mechanical properties represent the viscoelasticity parameters; (right) the corresponding curve fitting: the blue curve represents the computational simulation, the red curve represents the experimental data

Data	
Mechanical Constants	
1	0.025
2	0.04
3	0.06
4	0.7
5	0.09
6	0.7
7	0.0001
8	0.0175
9	0.4
10	1

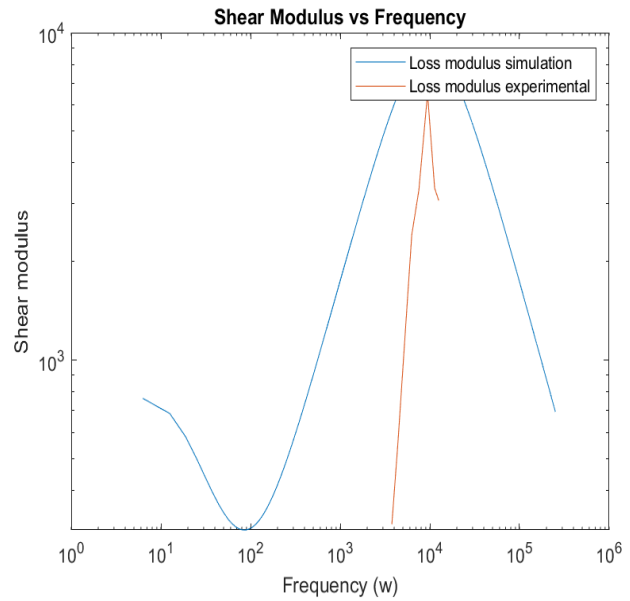


Figure 4.2: Second simulation: (left) the first seven mechanical properties represent the viscoelasticity parameters; (right) the corresponding curve fitting: the blue curve represents the computational simulation, the red curve represents the experimental data

Data	
Mechanical Constants	
1	0.03
2	0.05
3	0.04
4	0.45
5	0.09
6	0.7
7	0.0001
8	0.021
9	0.4
10	1

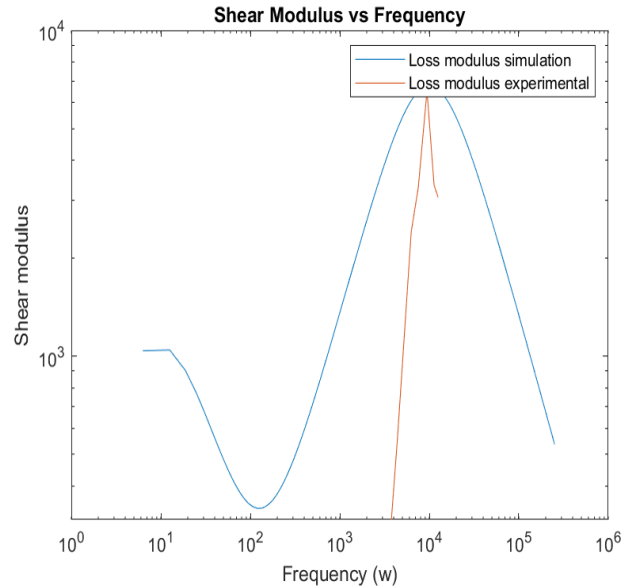


Figure 4.3: Third simulation: (left) the first seven mechanical properties represent the viscoelasticity parameters; (right) the corresponding curve fitting: the blue curve represents the computational simulation, the red curve represents the experimental data

Use unsymmetric material stiffness matrix

Data

Mechanical Constants	
1	0.03
2	0.05
3	0.04
4	0.55
5	0.09
6	0.7
7	0.0001
8	0.021
9	0.4
10	1

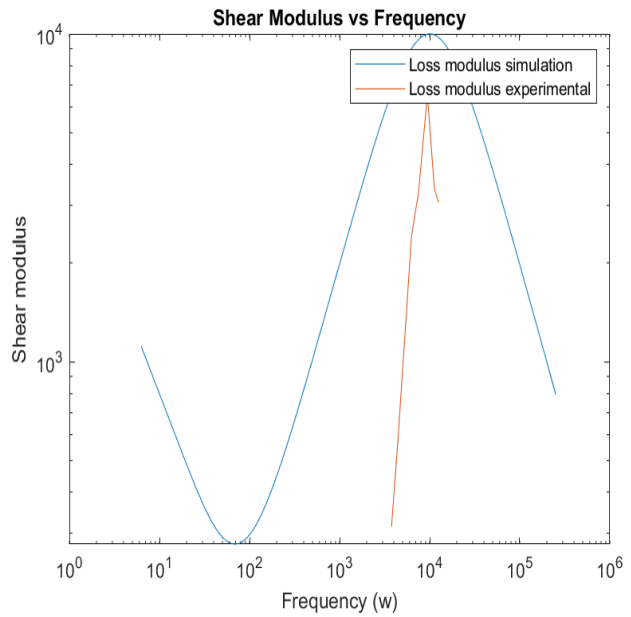


Figure 4.4: Fourth simulation: (left) the first seven mechanical properties represent the viscoelasticity parameters; (right) the corresponding curve fitting: the blue curve represents the computational simulation, the red curve represents the experimental data

Mechanical Constants	
1	0.035
2	0.05
3	0.002
4	0.5
5	0.085
6	0.5
7	9E-05
8	0.0245
9	0.4
10	1

=====

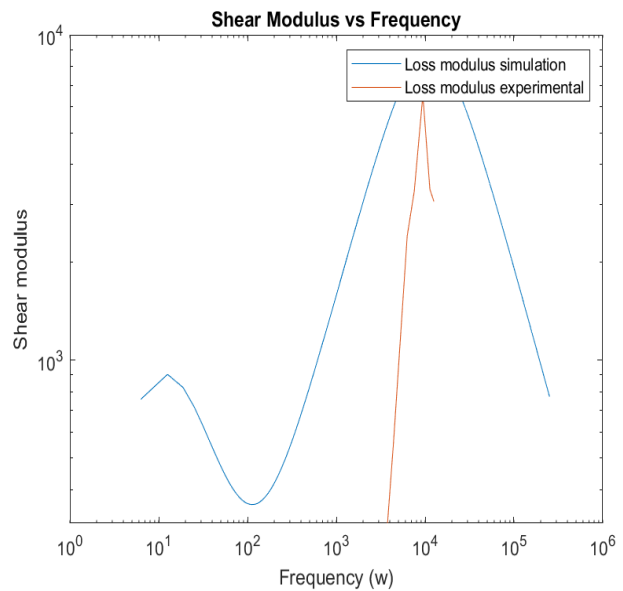


Figure 4.5: Fifth simulation: (left) the first seven mechanical properties represent the viscoelasticity parameters; (right) the corresponding curve fitting: the blue curve represents the computational simulation, the red curve represents the experimental data

Simulations have been conducted via a trial and error approach and, by evaluating the difference in the curves between the different simulations, conclusions have been drawn regarding the role that most parameters play:

- G_0 (here named as “a”) shifts the curve to the top when increasing its value
- By increasing g_1 a further hump to the left of the main hump gets created
- By increasing g_2 the left hump (given by g_1) vanishes, while the curve bursts to the top approaching the limit towards 0
- t_2 seems to have very little influence on the curve
- By increasing t_3 the curve shifts to the left

Table 4.1 summarizes values of each viscoelastic parameter for each simulation

Table 4.1: Values of viscoelastic parameters for each Matlab simulation

Parameters	Simulation 1	Simulation 2	Simulation 3	Simulation 4	Simulation 5
G0	50000	25000	30000	30000	35000
g1	0.006	0.04	0.05	0.05	0.05
g2	0.09	0.06	0.04	0.04	0.002
g3	0.4	0.7	0.45	0.55	0.5
t1	0.09	0.09	0.09	0.09	0.085
t2	0.7	0.7	0.7	0.7	0.5
t3	0.0001	0.0001	0.0001	0.0001	0.00009

4.2 EXPERIMENTAL DISPLACEMENT DATA VS. SIMULATION DISPLACEMENT DATA: A VISUAL COMPARISON

One of the declared goals of this thesis work is to come up with a valid comparison between the images of displacement acquired at the end of the ABAQUS simulation with those given by the experimental work carried out at the Acoustics and Vibrations Lab at UIC.

Initially computational simulation on the geometry was conducted by imposing the anisotropy direction along the x coordinate (direction 1) to the comparison purposes this would not have been useful: as a matter of fact, the actual anisotropic phantom used in the laboratory tests had fibers aligned in the vertical direction within the cross-section.

For this reason, images shown below, are organized with experimental displacement data on the left and computational images resulting from geometries in which the fibers are aligned in the vertical direction on the right.

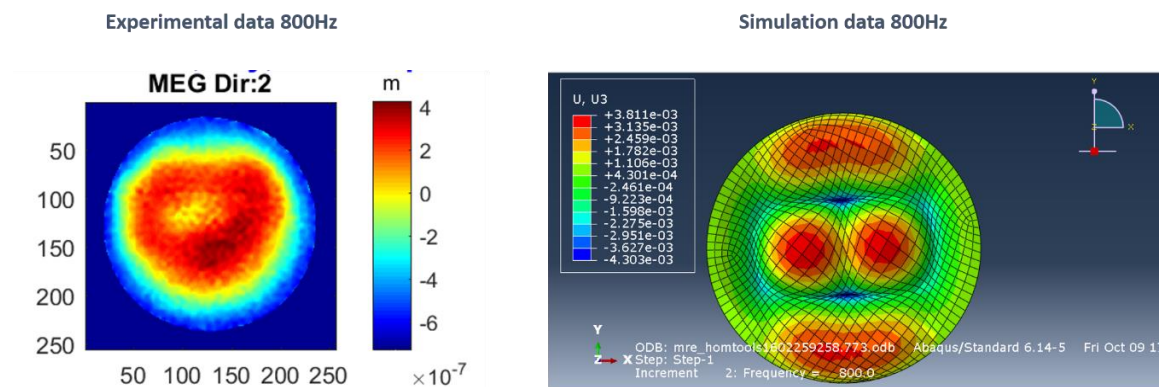


Figure 4.6: Images resulting from properties of the first simulation, evaluated at 800Hz with an anisotropic ratio value of 0.6

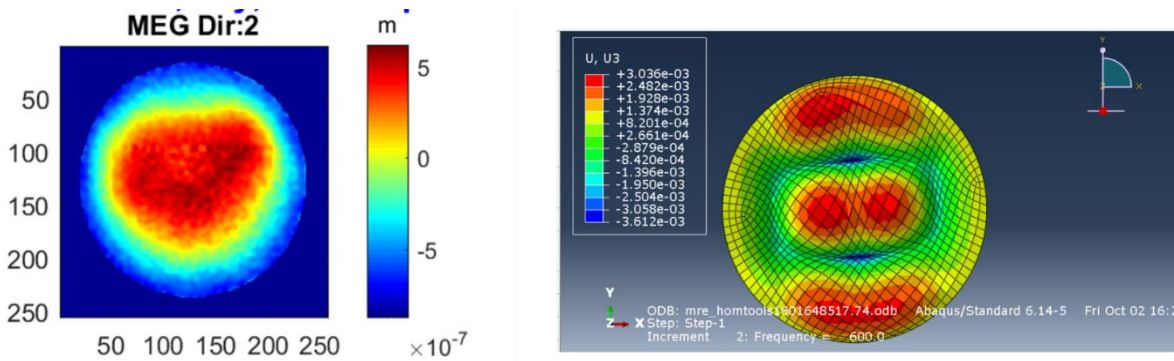


Figure 4.7: Images resulting from properties of the third simulation, evaluated at 600Hz with an anisotropic ratio value of 0.7

The first and most visible feature in both couple of images is the presence of an elongated ellipsoidal shape in the horizontal direction. This is consistent with the fact that fibers are aligned in the vertical direction within the cross section, because of the wave propagation pattern that tends to be faster along the stiffest material direction, thus with a longer wavelength along the fibers direction, as depicted in *Figure 4.8*.

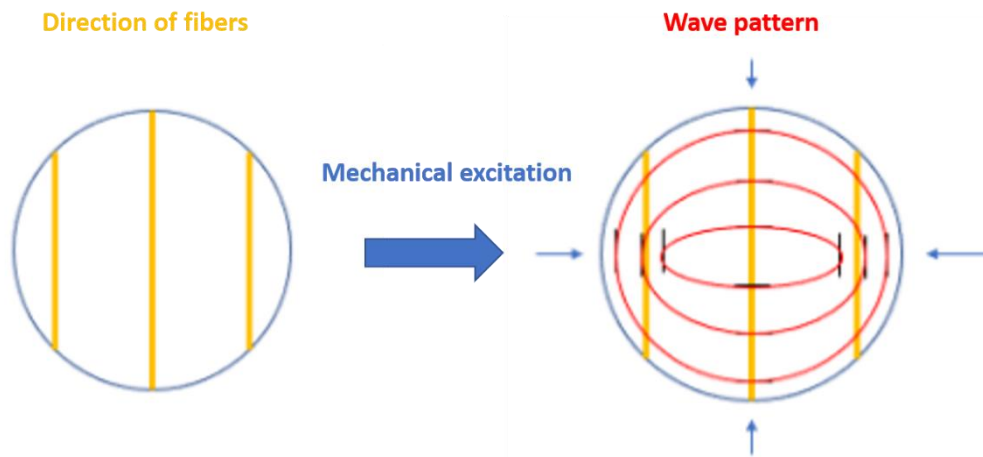


Figure 4.8: Visual explanation of the wave pattern inside a phantom with fibers aligned in the vertical direction

The fact that both the experimental data and the computational data present the same elongation may represent a partial validation of both the simulation settings in ABAQUS and the experimental procedure. More quantitative comparison would be required for a more detailed validation.

It is to be noted that properties between the actual experiment and the computational simulation are extensively different, despite the attempt of fitting the two curves in the Matlab plot, thus differences in the two displacement maps may be given by this property mismatch.

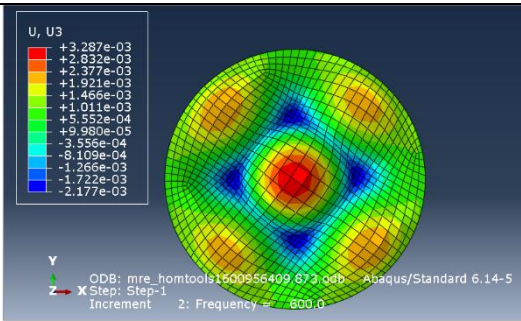
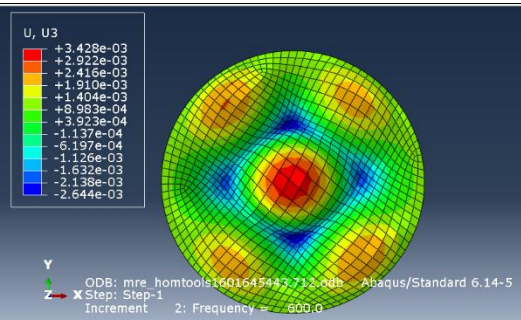
4.3 VARYING OF FIBERS ANISOTROPIC RATIO

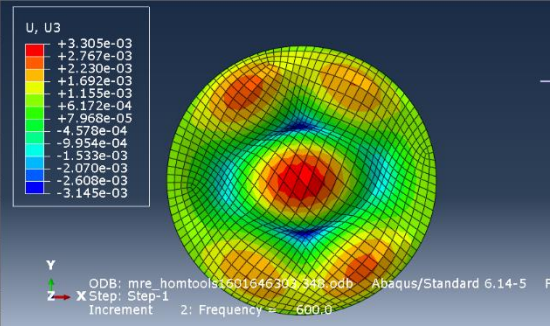
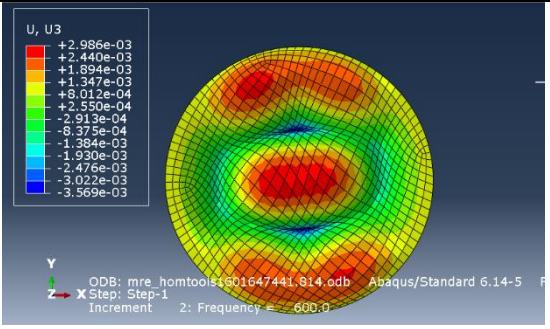
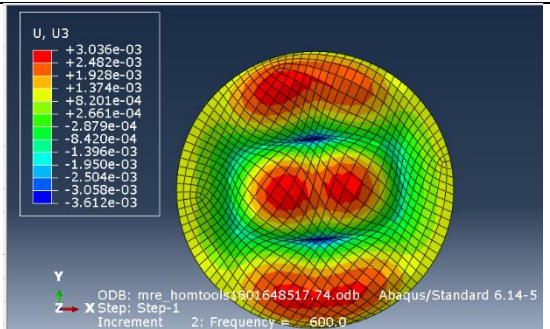
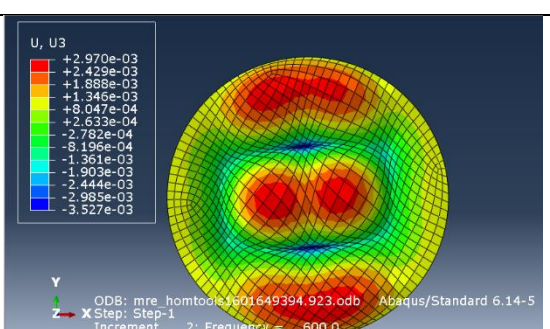
To demonstrate the impact given by the presence of fibers within a homogeneous matrix, one could perform different attempts within a simulation: this would maintain the same mechanical and viscoelastic properties, while progressively changing the anisotropic ratio, namely the factor by which the shear modulus in the direction perpendicular to the fiber is scaled with respect to the shear modulus in the direction parallel to the fibers.

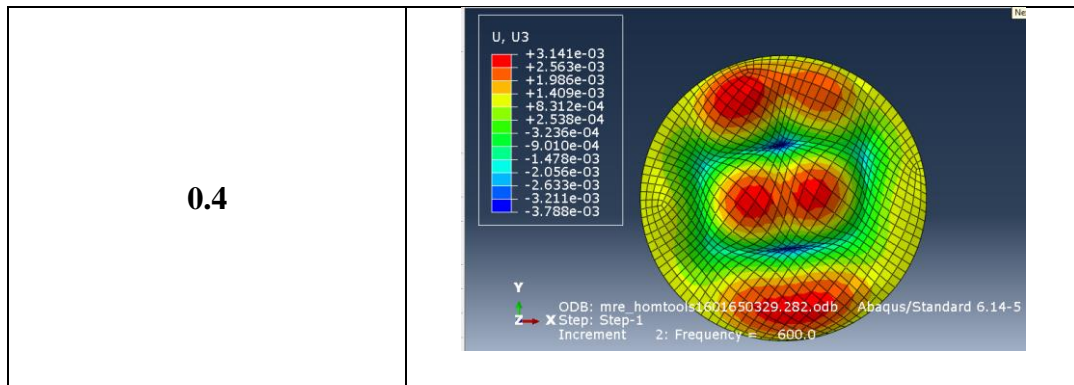
In ABAQUS this can be modified in the Property tab, changing the 8th entry in the Mechanical Constants table.

Table 4.2: Changes in the displacement images' pattern as the anisotropic ratio value increases the mismatch between parallel and perpendicular (to the fibers) direction.

Properties from the 3rd simulation (see paragraph above) at 600Hz

ANISOTROPIC RATIO	DISPLACEMENT IMAGE
1	
0.9	

<p style="text-align: center;">0.8</p>	 <p>U, U3</p> <ul style="list-style-type: none"> +3.305e-03 +2.767e-03 +2.230e-03 +1.692e-03 +1.155e-03 +6.172e-04 +7.968e-05 -4.578e-04 -9.954e-04 -1.533e-03 -2.070e-03 -2.608e-03 -3.145e-03 <p>Y Z X ODB: mre_homtools1601646309.348.odb Abaqus/Standard 6.14-5 Step: Step-1 Increment 2: Frequency = 600.0</p>
<p style="text-align: center;">0.7</p>	 <p>U, U3</p> <ul style="list-style-type: none"> +2.986e-03 +2.440e-03 +1.894e-03 +1.347e-03 +8.012e-04 +2.550e-04 -2.913e-04 -8.373e-04 -1.384e-03 -1.930e-03 -2.476e-03 -3.022e-03 -3.569e-03 <p>Y Z X ODB: mre_homtools1601647441.814.odb Abaqus/Standard 6.14-5 Step: Step-1 Increment 2: Frequency = 600.0</p>
<p style="text-align: center;">0.6</p>	 <p>U, U3</p> <ul style="list-style-type: none"> +3.036e-03 +2.482e-03 +1.928e-03 +1.374e-03 +8.201e-04 +2.661e-04 -2.879e-04 -8.420e-04 -1.396e-03 -1.950e-03 -2.504e-03 -3.058e-03 -3.612e-03 <p>Y Z X ODB: mre_homtools1601648517.74.odb Abaqus/Standard 6.14-5 Step: Step-1 Increment 2: Frequency = 600.0</p>
<p style="text-align: center;">0.5</p>	 <p>U, U3</p> <ul style="list-style-type: none"> +2.970e-03 +2.429e-03 +1.883e-03 +1.346e-03 +8.047e-04 +2.633e-04 -2.782e-04 -8.196e-04 -1.361e-03 -1.903e-03 -2.444e-03 -2.985e-03 -3.527e-03 <p>Y Z X ODB: mre_homtools1601649394.923.odb Abaqus/Standard 6.14-5 Step: Step-1 Increment 2: Frequency = 600.0</p>



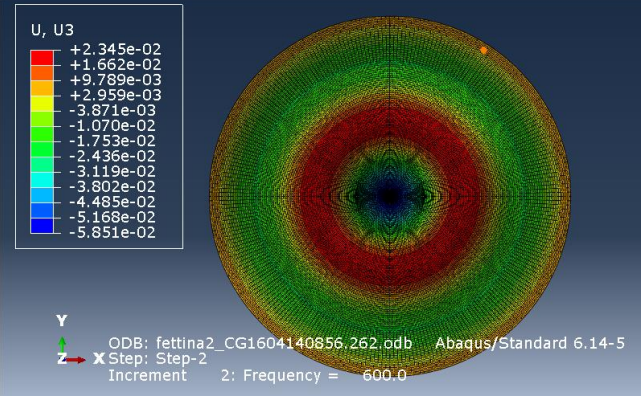
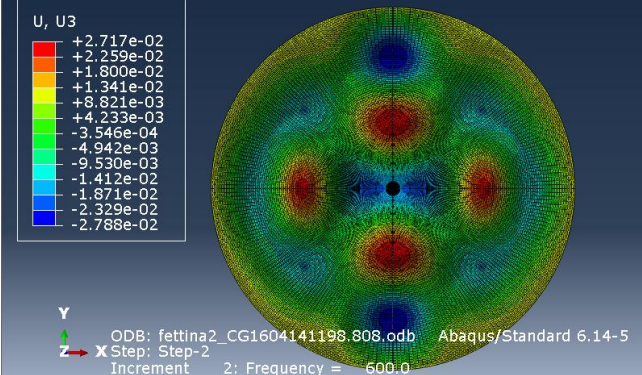
From this simulation it is evident that the elongation in the x direction (having fibers aligned in the y direction, as in the real experiments) increases as the difference between the two shear moduli increases.

Furthermore, to better visualize the effect that different fibers' volume fractions have on the wave displacement pattern, one could exploit the presence of the newly created geometry (quarter slice), that displays a thicker mesh.

Visual results for displacement patterns, in this case, would be feasible provided a mirroring of the geometry.

Table 4.3: Changes in the displacement images' pattern as the anisotropic ratio value increases the mismatch between parallel and perpendicular (to the fibers) direction evaluated for the smaller, more thickly meshed geometry.

Properties from the 3rd simulation (see paragraph above) at 600Hz

ANISOTROPIC RATIO	DISPLACEMENT IMAGE
1	
0.4	

It is evident that, shuttling from an isotropic case (value of anisotropic ratio of 1) to a highly anisotropic case (value of anisotropic ratio of 0.4) the wave mode strongly changes, going from concentric circles to elongated ellipses.

4.4 COMBINING VARIATIONS IN FREQUENCY OF ACTUATION AND ANISOTROPIC RATIO

To further investigate the anisotropic behavior of the phantom, one could try another visual experiment, that consists in both varying the anisotropic ratio and the frequency of actuation.

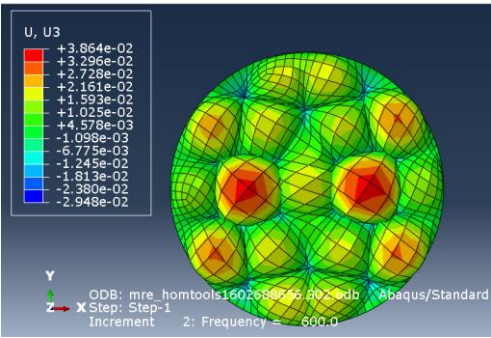
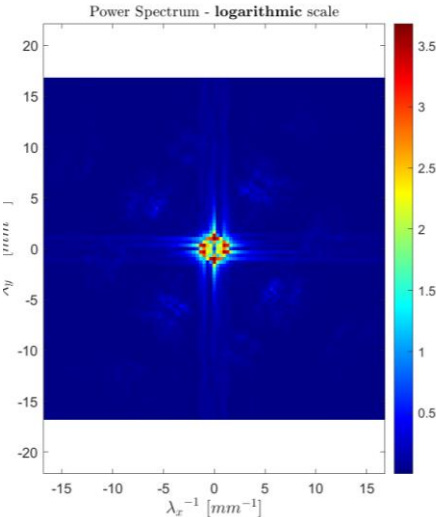
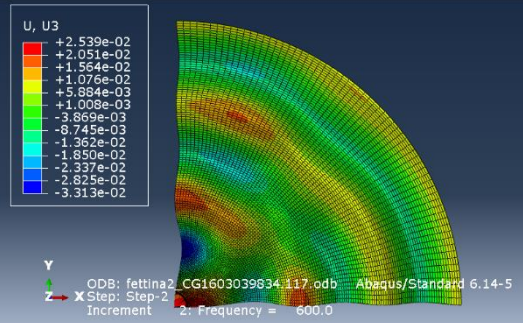
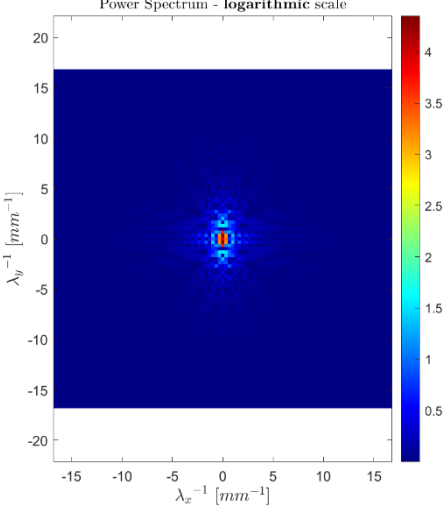
Table 4.4: Representation of displacement images from the first simulation at different frequencies (500 and 800Hz) and different anisotropic ratio (1 and 0.4)

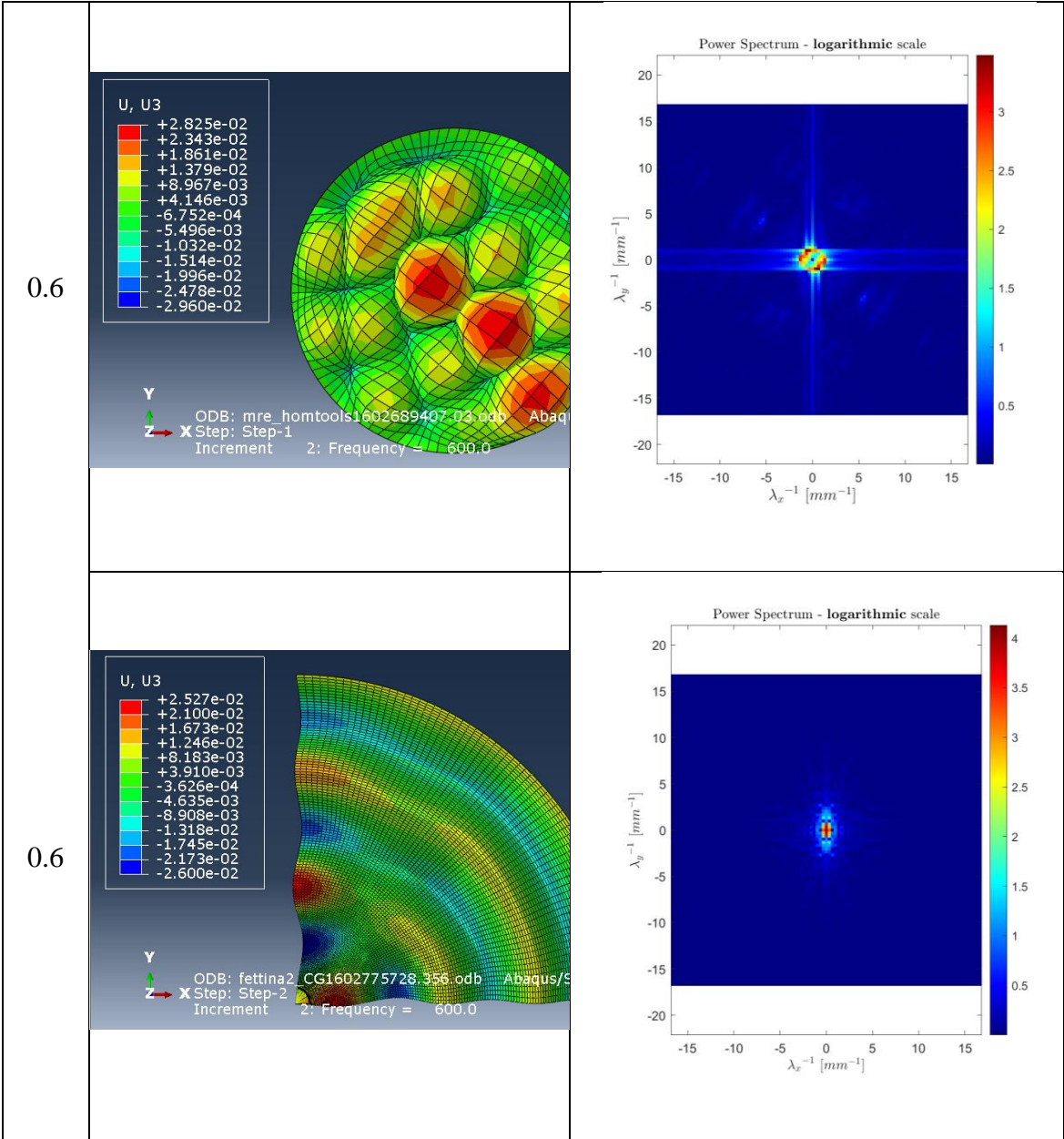
A.R / Freq	500Hz	800Hz
1	<p>U, U3 +5.550e-03 +4.855e-03 +4.161e-03 +3.466e-03 +2.771e-03 +2.076e-03 +1.381e-03 +6.866e-04 -8.208e-05 -7.030e-04 -1.398e-03 -2.093e-03 -2.787e-03</p> <p>Y X Step: Step-1 Increment 1: Frequency = 500.0</p>	<p>U, U3 +2.919e-03 +2.501e-03 +2.084e-03 +1.668e-03 +1.249e-03 +9.314e-04 +4.140e-04 -3.494e-06 -4.210e-04 -8.384e-04 -1.256e-03 -1.673e-03 -2.091e-03</p> <p>Y X Step: Step-1 Increment 2: Frequency = 800.0</p>
0.4	<p>U, U3 +4.889e-03 +4.250e-03 +3.611e-03 +2.972e-03 +2.333e-03 +1.693e-03 +1.054e-03 -2.238e-04 -8.629e-04 -1.502e-03 -2.141e-03 -2.780e-03</p> <p>Y X Step: Step-1 Increment 1: Frequency = 500.0</p>	<p>U, U3 +2.931e-03 +2.406e-03 +1.880e-03 +1.355e-03 +8.289e-04 +3.033e-04 -7.480e-04 -1.274e-03 -2.223e-04 -1.799e-03 -2.325e-03 -2.850e-03 -3.376e-03</p> <p>Y X Step: Step-1 Increment 4: Frequency = 800.0</p>

The elongated ellipsoidal shape becomes more visible at high frequencies and when the mismatch between the shear moduli is higher: this is due to the fact that, as the stiff component increases the complex stiffness does too.

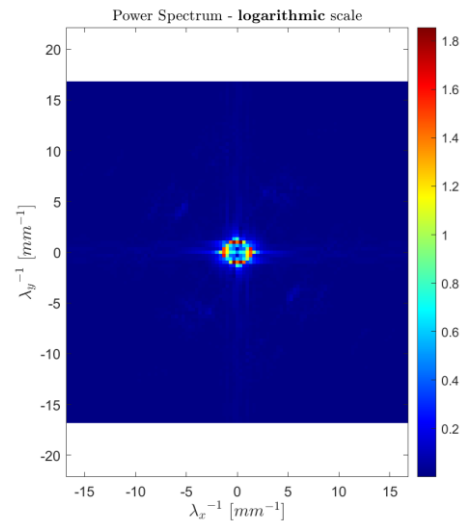
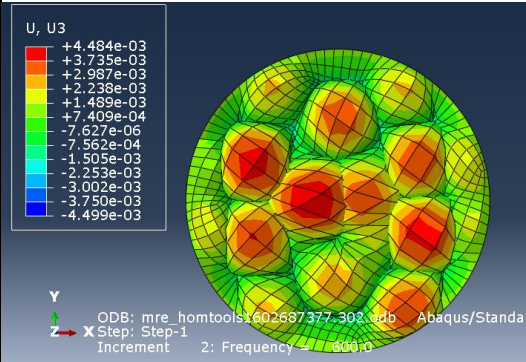
4.5 FROM DISPLACEMENT IMAGES TO SHEAR MODULUS VALUES VIA FOURIER TRANSFORM

Table 4.5: Comparison between displacement image and Fourier map of the whole geometry VS the sliced geometry for different anisotropic ratio values. Properties from the 3rd simulation (see paragraph above) at 600Hz and density value $\times 4$.

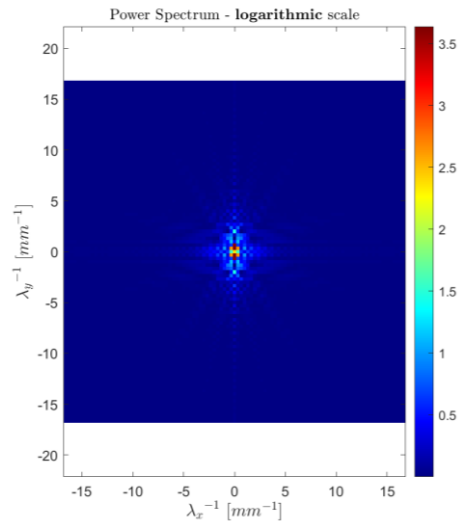
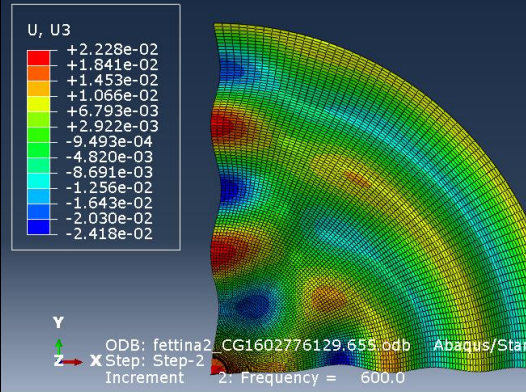
AR	DISPLACEMENT IMAGE	FOURIER MAP
0.7	 <p style="font-size: small;">ODB: mre_homtools1607688076.002.odb Abaqus/Standard Step: Step-1 Increment 2: Frequency = 600.0</p>	 <p style="font-size: small;">Power Spectrum - logarithmic scale</p>
0.7	 <p style="font-size: small;">ODB: fettina2_CG1603039834.117.odb Abaqus/Standard 6.14-5 Step: Step-2 Increment 2: Frequency = 600.0</p>	 <p style="font-size: small;">Power Spectrum - logarithmic scale</p>



0.5



0.5



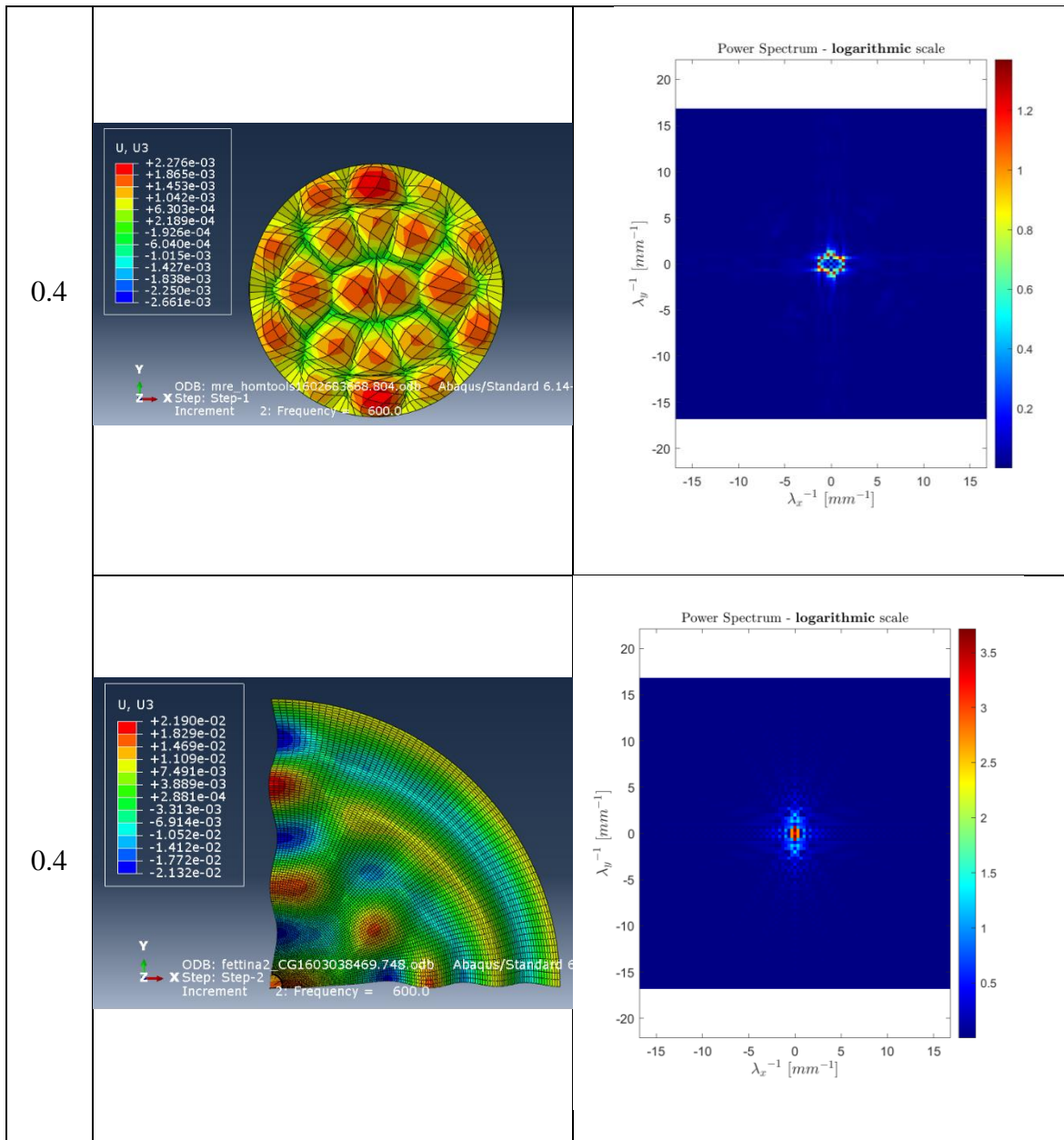


Table 4.5 clearly shows that postprocessing of the sliced geometry guarantees better results in terms of Fourier maps. As a matter of fact, a clear elongation in the y direction is visible in these maps, while the same cannot be said for the Fourier maps relative to the whole geometry: this may be due to the presence of a better mesh on the smaller feature that, thanks to the mirroring process, gets propagated and duplicated on a virtual circular cross section. As for the presence of peaks in the Fourier maps, these are more clearly visible also due to the fact that density has been increased by a factor of 4 with respect to the original setup, going from 1.06E-09 to 4.24E-09. A visual representation of the difference between the use of the two density values is shown in *Figure 4.9*

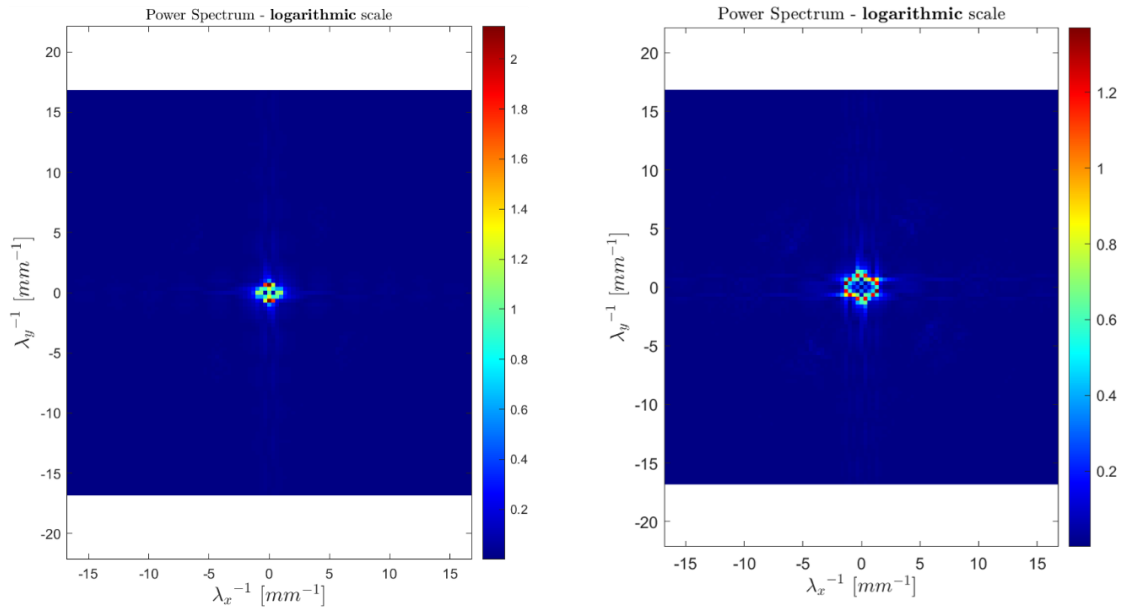


Figure 4.9: Fourier maps for the same simulation (third simulation at 600 Hz). On the left density value is $1.06E-09$, on the right density value is $4.24E-09$

4.6 WAVE NUMBER VS. ANISOTROPIC RATIO: A QUANTITATIVE COMPARISON

After having delineated the power spectrum heatmap for each anisotropic ratio value within each simulation, one could create a series of plots that describe the relationship between the wave number and the power density, previously delineated by the different color intensities in the heatmap.

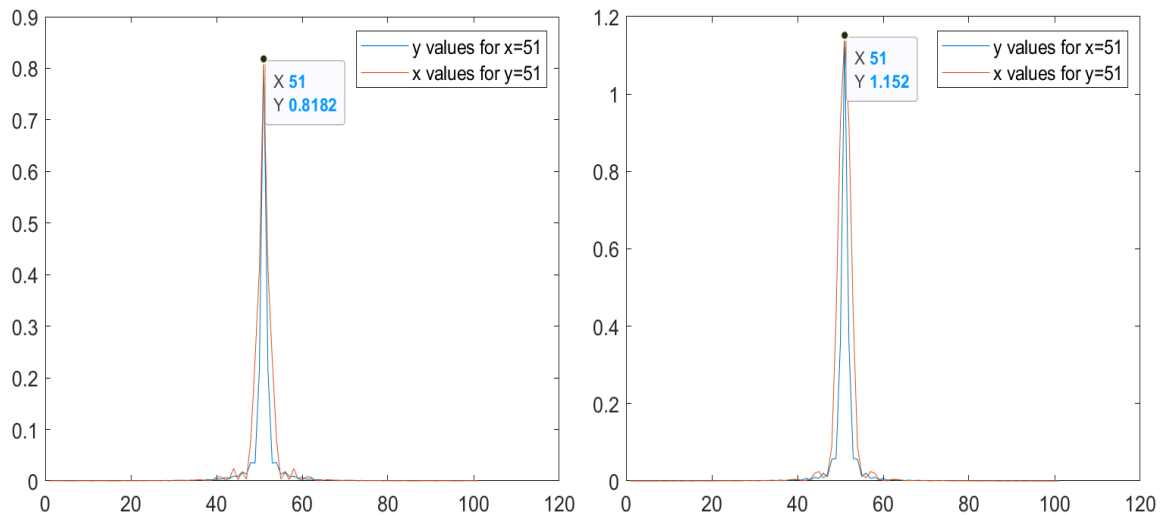


Figure 4.10: Plots from the 1st simulation at 3000Hz. Left: anisotropic ratio of 1; Right: anisotropic ratio of 0.3. X axis represents alternatively values of λ_x^{-1} and λ_y^{-1} . Y axis represents the power density

Although the difference between the two plots is not pronounced, it is still possible to visualize variations between the two plots that represents phantoms that have different anisotropic ratio values.

The left plot refers to the case in which shear moduli in the two directions have the same value, i.e. anisotropic ratio=1. The right plot refers to a value of anisotropic ratio value of 0.3, referring to the fact that the two shear moduli are highly different.

It is visible that the two colored lines tend to stick more tightly together when the AR=1, while slightly growing apart with AR=0.3

Moreover, these plots represent the starting point for the extraction of shear modulus values (parallel and perpendicular to the fibers), via the use of the LFE technique that exploits the extraction of wave numbers.

In this case, wave numbers may be directly taken from the plots following the relation

$$k = \frac{2\pi}{\lambda} \quad [4.1]$$

And its extraction may provide value for the shear modulus

$$\mu = \frac{\omega^2 \rho}{k^2} \quad [4.2]$$

This last step represents the recovery of an inverse problem: care must be taken in the setting of the UMAT subroutine, making sure that the anisotropic ratio value results congruent to the fiber volume fraction of the real phantom. This had been calculated to be of 14%, meaning that (assuming a direct relationship between volume of the fibers and shear modulus) the ratio between the moduli in the two directions needs to be between 80% and 90% approximately.

Still, in order to perform this task, a correct density value for the real phantom needs to be known and used throughout the entire simulation.

4.7 BYPASSING THE PROPERTIES FITTING: A MORE PUNCTUAL ASSESSMENT OF THE WHOLE PROCESS

A final analysis can be performed to determine which solution or merging of solutions works better for our purposes: this consists in plugging properties into the simulation in a slightly different manner with respect to what was previously done. Rather than creating a curve fitting of the numerical properties on the experimental ones, one could simply plug the values of shear modulus available from the experimental UIC results.

Each frequency possesses four values, coupled two by two: two are related to the parallel modulus (real and imaginary), the other two are related to the perpendicular modulus (real and imaginary) (see Table 3.2).

Hereby images resulting from the computational analysis carried out at 1500 Hz are displayed; shear modulus values are directly taken from Table 3.2.

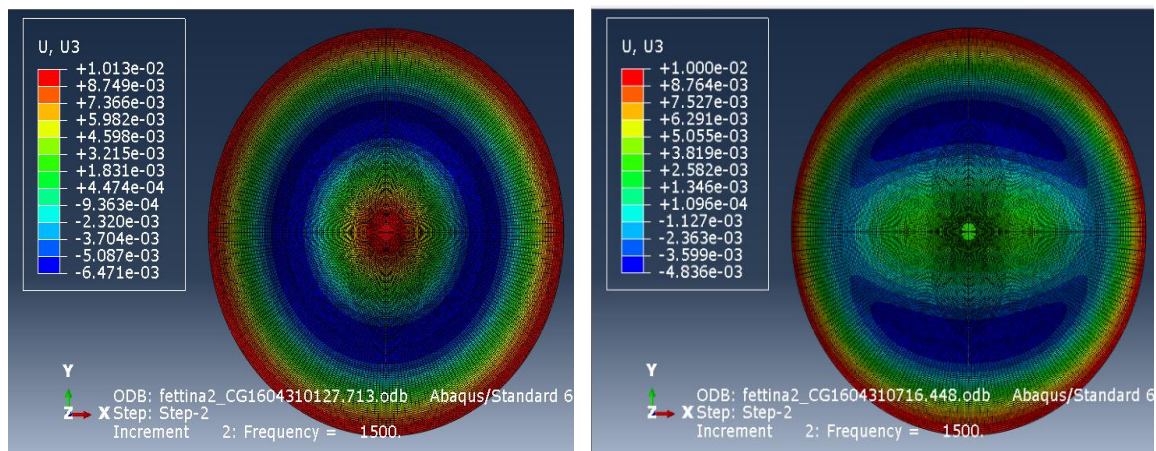


Figure 4.11: Visualization of displacement pattern for simulations run at 1500Hz adjusting the FE shear modulus values to the experimental values. Left: anisotropic ratio value of 1. Right: anisotropic ratio value of 0.1

Figure 4.11 shows a pronounced difference in the way waves propagate through the media when different amounts of fibrous structures are employed, having an elongated ellipsoidal pattern with an increasing difference between shear moduli in the two directions (parallel and perpendicular to the fibers).

The latter image (anisotropic ratio value=0.1) can be further used as a source of comparison with the displacement maps provided by the experiments done at UIC.

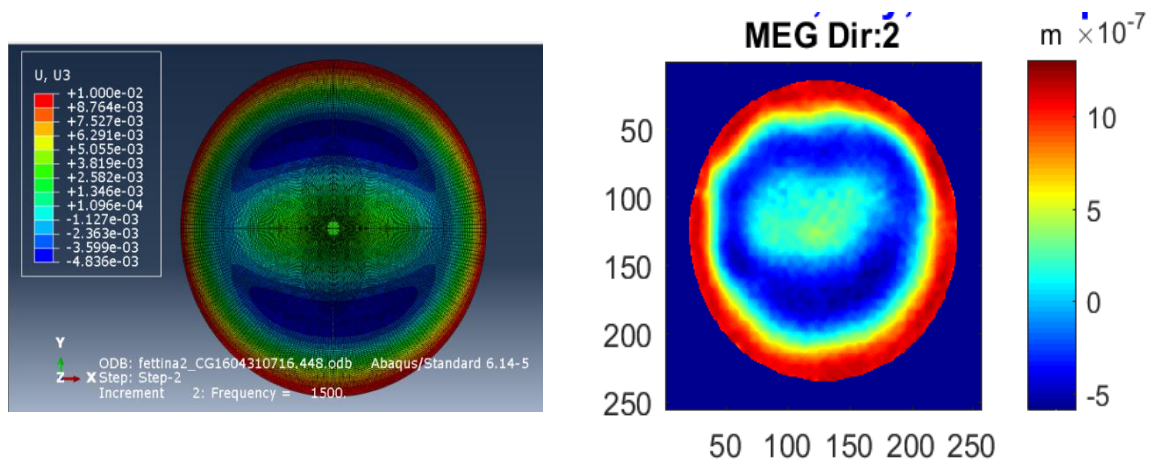


Figure 4.12: Comparison between FE simulation and MRE experiment. Frequency=1500Hz

The two images show the same kind of elongation; additionally, the color intensity wave of the two heatmaps shows a comparable pattern.

All the passages that were conducted for the previous types of simulations can be performed in this case as well, going from the extraction of data for the displacement in the z direction, to the visualization of the power spectrum and the subsequent plot reconstruction.

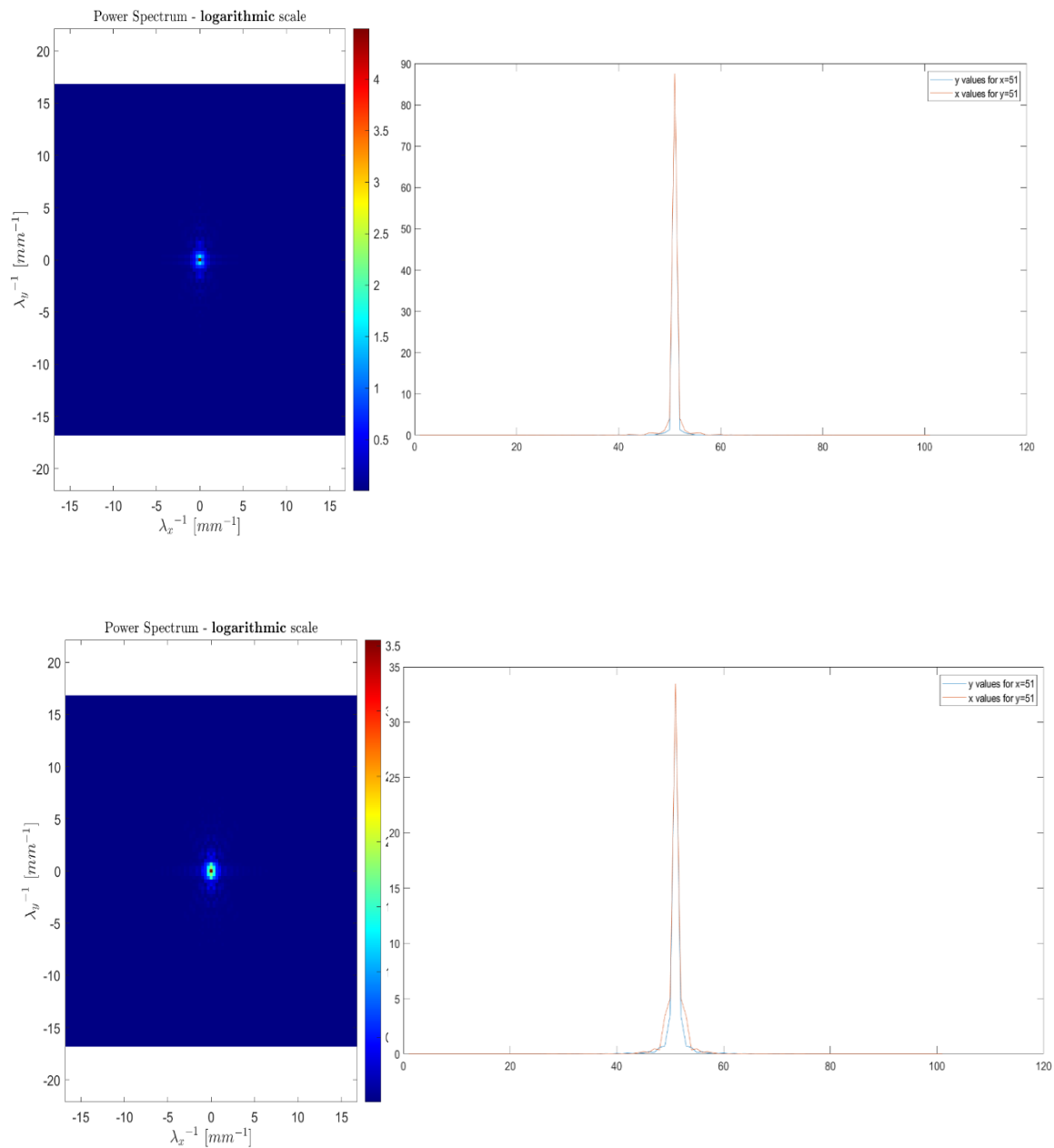


Figure 4.13: Top row shows the power spectrum and plot for the simulation run at 1500Hz with an anisotropic ratio value of 1. Bottom row shows the power spectrum and plot for the simulation run at 1500Hz with an anisotropic ratio value of 0.1

Both the power spectrum images and the plots better delineate the differences in applying different anisotropic ratio values with respect to the images gathered from previous simulations.

However, this newly adopted methodology lacks in versatility, meaning that the values of shear modulus need to be changed in the UMAT subroutine whenever a new frequency value is plugged in the Abaqus Step tab, preventing the user from a faster analysis.

5 CONCLUSION AND FUTURE DEVELOPMENTS

This thesis work poses itself in the wide panorama of research on the topic of Magnetic Resonance Elastography: the technique has been proposed as an innovative and non-invasive solution for the healing of various and severe pathologies that affect different body districts. Focus has been set to skeletal muscle tissue that can be affected by a series of neuromuscular disorders; the overall visible effect of such ailments is the modification of properties within the tissue itself. MRE sets itself the objective of preemptively detecting and analyzing such changes, in order to stop the evolution of the disease. The technique is based on an inversion algorithm that, after having provided a harmonic excitation to the sample and having visualized the displacement pattern followed by mechanical waves inside the material, reverses the displacement results to data of shear moduli. Yet, the process is not so intuitive when anisotropic media, such as skeletal muscle tissue, comes into play. For this reason, the specific aim of this project is to implement an inverted approach of the traditional MRE technique, that is to say, the creation of a “Direct Problem” that would switch from data of shear moduli to displacement field images. In this specific case, the input shear moduli data has been provided (and subsequently rearranged) by a series of previous experiments that were carried out by the author in the Acoustics and Vibrations Lab of the University of Illinois at Chicago. The Direct Problem would thus serve as a source of comparison between displacement images coming from the simulation and the experimental ones, in addition to being a useful tool to assess the effect of material properties on the way waves propagate.

Starting from the acquisition of mechanical properties for the simulation input, this work has explored different modalities to be fitting properties from the ones gathered from the UIC experiment:

- The first analysis that provides good results is the Matlab fitting utilizing equations that take into account the viscoelasticity of the material (eq. 3.6 and 3.7). The viscoelastic parameters have been set by means of a trial and error procedure: this methodology seems to provide curves for the simulation that do not quite match the experimental ones. Yet the result in terms of displacement

maps provides good and comparable images between those coming from the simulation and those coming from the experiments. As the anisotropic ratio and the frequency of actuation increase, the ellipsoidal elongation of the maps does too both for the FEA and for the UIC results. This demonstrates that the MRE technique and its computational imitation are able to highlight differences within anisotropic tissues, characterized by different levels of fiber volume fractions.

This positive result is visible for all types of fittings carried out in the Matlab sequence, albeit the viscoelastic parameters employed differ.

- Additionally, to provide a better assessment of the similarities between the two works, a second path has been followed: this consists of taking the input properties from the results provided by the experimental analysis and directly plug them in the simulation without any kind of rearrangement. This trial has resulted particularly successful in the visualization of displacement maps that, for the same set of frequencies, show a high level of similarity both in the displayed geometry and in the color intensity pattern, validating at the same time both the experimental and the numerical procedure. However accurate, this method has the disadvantage of forcing the user to iteratively change the coupling between frequency and shear modulus value, not exploiting the possibility of executing analyses simultaneously in a vast range of frequency.

Employing the visualization of displacement images, this work has provided an alternative to what had been previously done by Yasar et al.: in their work, the differences between the numerical simulation and the experiment were provided by means of plots showing the displacement profile (for the two cases) on the cylinder top surface as a function of radial position; the comparison that is proposed in this work is somewhat more immediate to the reader, as it presents the actual displacement images, allowing for fast detection of noteworthy differences.

Another positive outcome of the work is the fact that different anisotropic ratio values do provide a substantial difference to the simulation results. This difference is highly visible in the displacement maps, thanks to the degree of elongation, that deviates from the concentric pattern visible for isotropic samples; still, it lacks in clearness in the power spectrum

heatmaps, retrieved thanks to a 2D Fourier Transform on the acquired displacement data. However, the heatmaps are needed in order to create wave number VS power spectrum plots where the discrepancies when using different anisotropic ratio values are not only visible but also quantifiable.

The plots may represent the starting point for a less complicated extraction of mechanical parameters: as a matter of fact, the LFE technique states that values for the shear modulus can be calculated, provided the presence of a wave number, which, as mentioned before, has been extracted via a Fourier Transformation. This will be feasible when both the exact density value and the anisotropic ratio (quantity of fibers) for the phantom will be known.

Overall this work has resulted successful in tracing the actual experiments and, given the comparable results, has provided a validation to the employed MRE process: when plugging experimental values into a computational simulation (theoretically set as the given experiment) this returns the same result (displacement map) from which the experiment had started. It is thus certified the interchangeability of the inverse and direct problem in this particular scenario.

Moreover, this work represents a further validation of the fact that anisotropy present within samples provides a tangible contribution to the wave transmission: as the stiff component increases, the complex stiffness does too.

Although the analysis has been successful in providing what was intended for it as a first aim some issues are still present:

The direct problem formulation entails as a final result the extraction of the displacement images: however, this has not been the last step of this analysis which continued with the numerical data extraction and the plotting of the power spectrum result. In this way, the problem turns out to be an inverse formulation of an initial different direct problem. Quantitative interpretation of the plots is still not clear and further study on the subject may be needed.

Furthermore, when evaluating displacement images coming from simulations that were provided with properties taken by the Matlab fitting, different modes of vibrations are visible in the FE images; these were not present in the experimental analysis: this may be due to the

fact that properties of stiffness, density and anisotropy are not exactly those present in the anisotropic phantom, albeit the struggle of tracing them as precisely as possible.

One should be able to plug in the simulation the exact properties of the used phantom, without resorting to the expedient of inserting as properties those that were results of an experiment and that may present errors, given by the nature of the experiment itself. To do so, one could exploit the “Barbero code” and apply a homogenization procedure between the properties of the matrix and those of the fibers. Unfortunately, no precedent literary work nor technical sheets presented the needed details for the two materials in terms of stiffness, Young’s modulus and density.

Direct problems rest on their inputs, which are the material properties: the lack of detailed information on these or even a slight mismatch between density values may result in major differences and inaccuracies when analyzing results.

CITED LITERATURE

1. Duck FA. *Physical Properties of Tissue. A Comprehensive Reference Book.*; 1990.
2. Sarvazyan AP, Skovoroda AR, Emelianov SY, et al. Biophysical Bases of Elasticity Imaging. In: ; 1995. doi:10.1007/978-1-4615-1943-0_23
3. Krouskop TA, Wheeler TM, Kallel F, Garra BS, Hall T. Elastic moduli of breast and prostate tissues under compression. *Ultrasound Imaging.* 1998. doi:10.1177/016173469802000403
4. Barton MB, Harris R, Fletcher SW. Does this patient have breast cancer? The screening clinical breast examination: Should it be done? How? *J Am Med Assoc.* 1999. doi:10.1001/jama.282.13.1270
5. Manduca A, Oliphant TE, Dresner MA, et al. Magnetic resonance elastography: Non-invasive mapping of tissue elasticity. *Med Image Anal.* 2001;5(4):237-254. doi:10.1016/S1361-8415(00)00039-6
6. Varghese T. Quasi-Static Ultrasound Elastography. *Ultrasound Clin.* 2009. doi:10.1016/j.cult.2009.10.009
7. Fung YC, Skalak R. Biomechanics. Mechanical Properties of Living Tissues. *J Appl Mech.* 1982. doi:10.1115/1.3162171
8. Klatt D. Lecture notes, Elastography course. 2019.
9. Gennisson JL, Deffieux T, Fink M, Tanter M. Ultrasound elastography: Principles and techniques. *Diagn Interv Imaging.* 2013;94(5):487-495. doi:10.1016/j.diii.2013.01.022
10. Mariappan YK, Glaser KJ, Ehman RL. Magnetic resonance elastography: A review. *Clin Anat.* 2010. doi:10.1002/ca.21006
11. Fowlkes JB, Emelianov SY, Pipe JG, et al. Magnetic-resonance imaging techniques for detection of elasticity variation. *Med Phys.* 1995;22(11):1771-1778. doi:https://doi.org/10.1118/1.597633
12. Sandrin L, Fourquet B, Hasquenoph J-M, et al. Transient elastography: a new noninvasive method for assessment of hepatic fibrosis. *Ultrasound Med Biol.* 2003;29(12):1705-1713. doi:10.1016/j.ultrasmedbio.2003.07.001
13. Bataller R, Brenner DA. Liver fibrosis. *J Clin Invest.* 2005;115(2):209-218.

- doi:10.1172/JCI24282
14. Venkatesh SK, Yin M, Ehman RL. Magnetic resonance elastography of liver: Technique, analysis, and clinical applications. *J Magn Reson Imaging*. 2013. doi:10.1002/jmri.23731
 15. Cadranel JF, Rufat P, Degos F. Practices of liver biopsy in France: Results of a prospective nationwide survey. *Hepatology*. 2000. doi:10.1053/jhep.2000.16602
 16. Poynard T, Ratziu V, Bedossa P. Appropriateness of liver biopsy. *Can J Gastroenterol*. 2000. doi:10.1155/2000/107982
 17. Soloway RD, Baggenstoss AH, Schoenfield LJ, Summerskill WHJ. Observer error and sampling variability tested in evaluation of hepatitis and cirrhosis by liver biopsy. *Am J Dig Dis*. 1971. doi:10.1007/BF02235164
 18. Maharaj B, Leary WP, Naran AD, et al. SAMPLING VARIABILITY AND ITS INFLUENCE ON THE DIAGNOSTIC YIELD OF PERCUTANEOUS NEEDLE BIOPSY OF THE LIVER. *Lancet*. 1986. doi:10.1016/S0140-6736(86)90883-4
 19. Abdi W, Millan JC, Mezey E. Sampling Variability on Percutaneous Liver Biopsy. *Arch Intern Med*. 1979. doi:10.1001/archinte.1979.03630430043014
 20. Friedman SL. Liver fibrosis - From bench to bedside. *J Hepatol Suppl*. 2003. doi:10.1016/s0168-8278(02)00429-4
 21. Venkatesh SK, Ehlman RL. *Magnetic Resonance Elastography*. Springer; 2014.
 22. Singh S, Venkatesh SK, Wang Z, et al. Diagnostic performance of magnetic resonance elastography in staging liver fibrosis: A systematic review and meta-analysis of individual participant data. *Clin Gastroenterol Hepatol*. 2015. doi:10.1016/j.cgh.2014.09.046
 23. Yin M, Talwalkar JA, Glaser KJ, et al. Assessment of Hepatic Fibrosis With Magnetic Resonance Elastography. *Clin Gastroenterol Hepatol*. 2007. doi:10.1016/j.cgh.2007.06.012
 24. Ophir J, Céspedes I, Ponnekanti H, Yazdi Y, li X. Elastography: A quantitative method for imaging the elasticity of biological tissues. *Ultrason Imaging*. 1991. doi:10.1177/016173469101300201
 25. Szabo TL. *Diagnostic Ultrasound Imaging: Inside Out.*; 2004. doi:10.1055/s-2005-861725
 26. Ultrasound Imaging. <https://www.medicalradiation.com/types-of-medical->

- imaging/other-types-of-medical-imaging/ultrasound-imaging. Accessed December 29, 2019.
27. Weishaupt D, Köchli VD, Marincek B. *How Does MRI Work?*; 2003. doi:10.1007/978-3-662-07805-1
 28. Lieber RL, Steinman S, Barash IA, Chambers H. Structural and functional changes in spastic skeletal muscle. *Muscle and Nerve*. 2004. doi:10.1002/mus.20059
 29. Basford JR, Jenkyn TR, An KN, Ehman RL, Heers G, Kaufman KR. Evaluation of healthy and diseased muscle with magnetic resonance elastography. *Arch Phys Med Rehabil*. 2002;83(11):1530-1536. doi:10.1053/apmr.2002.35472
 30. Sack I, Bernarding J, Braun J. Analysis of wave patterns in MR elastography of skeletal muscle using coupled harmonic oscillator simulations. *Magn Reson Imaging*. 2002;20(1):95-104. doi:10.1016/S0730-725X(02)00474-5
 31. Lorgna G. FINITE ELEMENT MODELS FOR MAGNETIC RESONANCE ELASTOGRAPHY (MRE) APPLIED TO ANISOTROPIC PHANTOM. 2017.
 32. Rothwell J. *Control of Human Voluntary Movement*.
 33. Tortora GJ, Nielsen MT. *Principles of Human Anatomy*. Vol 53.; 2012.
 34. Guidetti M. Transverse Isotropic Multiscale Muscle Phantom for MR Elastography.
 35. Hirsch S, Braun J, Sack I. *Magnetic Resonance Elastography*.; 2016. doi:10.1002/9783527696017
 36. Martina Guidetti , Dieter Klatt TJ. R. TRANSFORMATION ELASTOGRAPHY : CONVERTING ANISOTROPY TO ISOTROPY. 2(1):2-5.
 37. Brokešová J. Reflection/transmission coefficients at a plane interface in dissipative and nondissipative isotropic media: A comparison. *J Comput Acoust*. 2001. doi:10.1142/S0218396X01000760
 38. Guidetti M, Royston TJ. Analytical solution for converging elliptic shear wave in bounded and unbounded transverse isotropic viscoelastic material with nonhomogeneous inner boundary. *J Acoust Soc Am*. 2019;145(1):EL59-EL65. doi:10.1121/1.5088028
 39. Guidetti M, Royston TJ. Analytical solution for diverging elliptic shear wave in bounded and unbounded transverse isotropic viscoelastic material with nonhomogeneous inner boundary. *J Acoust Soc Am*. 2019;145(1):EL59-EL65. doi:10.1121/1.5088028

40. Klatt D, Papazoglou S, Braun J, Sack I. Viscoelasticity-based MR elastography of skeletal muscle. *Phys Med Biol*. 2010;55(21):6445-6459. doi:10.1088/0031-9155/55/21/007
41. Fovargue D, Nordsletten D, Sinkus R. Stiffness reconstruction methods for MR elastography. *NMR Biomed*. 2018;31(10):e3935-e3935. doi:10.1002/nbm.3935
42. Martincek I, Pudis D, Chalupova M. Technology for the preparation of PDMS optical fibers and some fiber structures. *IEEE Photonics Technol Lett*. 2014;26(14):1446-1449. doi:10.1109/LPT.2014.2326695
43. Morimoto Y, Kato-Negishi M, Onoe H, Takeuchi S. Aligned free-standing muscle fibers connected with neurons. In: *15th International Conference on Miniaturized Systems for Chemistry and Life Sciences 2011, MicroTAS 2011*. ; 2011.
44. Yasar, Temel K., Royston, Thomas J., Magin RL. Wideband MR elastography for viscoelasticity model identification. 2012;100(2):130-134. doi:10.1016/j.pestbp.2011.02.012.Investigations
45. Guidetti M, Romanò J. FE model for Magnetic Resonance Elastography experiments on a phantom replicating skeletal muscle tissues. 2016:841817.
46. Barbero EJ. *Finite Element Analysis of Composite Materials Using AbaqusTM*.; 2013. doi:10.1201/b14788
47. Carcione JM, Kosloff D, Kosloff R. Wave propagation simulation in a linear viscoelastic medium. *Geophys J*. 1988;95(1988):597-611. doi:10.1111/j.1365-246X.1988.tb06706.x
48. Endo VT, de Carvalho Pereira JC. Linear orthotropic viscoelasticity model for fiber reinforced thermoplastic material based on Prony series. *Mech Time-Dependent Mater*. 2017;21(2):199-221. doi:10.1007/s11043-016-9326-8
49. Writing USER Subroutines with ABAQUS.
50. Clayton EH, Okamoto RJ, Bayly P V. Mechanical properties of viscoelastic media by local frequency estimation of divergence-free wave fields. *J Biomech Eng*. 2013;135(2):1-6. doi:10.1115/1.4023433
51. Moratal D, Vallés-Luch A, Martí-Bonmati L, Brummers ME. k-Space tutorial: An MRI educational tool for a better understanding of k-space. *Biomed Imaging Interv J*. 2008. doi:10.2349/biij.4.1.e15

6 APPENDIX A: MATLAB CODES

BARBERO CODE

```
% FEAcamp. Solution of Example C.1
% E. J. Barbero, WVU, 2007
clear all,close all,
% Input file ExampleC1.dat
% Isotropic Matrix: Em, num,
% Transversely isotropic Fiber: EA,ET,nuAT,nuTT,GAT
% Fiber volume fraction: Vf
n_file = 'materialC1';disp(n_file);
% OPEN I/O FILES
%fidinp = fopen([n_file, '.dat'],'r');
%fidout = fopen([n_file, '_results.dat'],'w');
% READ PROPERTIES FROM INPUT FILE
%prop = fscanf(fidinp,'%g'); disp(prop);
%Vf = prop(8);
Vf=0.14
Vm = 1-Vf;
% Matrix
%E1 = prop(1);
E1=65* 10e3;
E2 = E1;      %%matrix is isotropic
E3 = E2;
%nu12 = prop(2);
nu12=0.5;
nu21 = nu12;
nu13 = nu12;
nu31 = nu21;
nu23 = nu12;
nu32 = nu23;
G12 = E1/2/(1+nu12);
G13 = G12;
G23 = G12;
Gm = G12;
num = nu12;
% COMPUTE S AND C
Sm= [1/E1      -nu21/E2      -nu31/E3  0  0  0;
     -nu12/E1   1/E2         -nu32/E3  0  0  0;
     -nu13/E1   -nu23/E2      1/E3     0  0  0;
     0  0  0  1/G23  0  0;
     0  0  0  0  1/G13  0;
     0  0  0  0  0  1/G12];
%
Cm = inv(Sm)
% Transversely isotropic fiber: plane of isotropy in dir 1
% E1, E2=E3, nu12=nu13, nu23, G12=G13, G23=E2/(2*(1+nu23))
%E1 = prop(3);
```

```

E1=1.8*10e6;      %Mpa
%E2 = prop(4);
%E2=24.8;
E2=E1;
E3 = E2;
%nu12 = prop(5);
nu12=0.311;
nu21 = nu12;
nu13 = nu12;
nu31 = nu21;
nu23 = nu12;
nu32 = nu23;
% nu21 = nu12*E2/E1;
% nu13 = nu12;
% nu31 = nu21;
%nu23 = prop(6);
%nu23=0.005;
%nu32 = nu23*E3/E2;
%G12 = prop(7);
%G12=44.1;

G12 = E1/2/(1+nu12);
G13 = G12;
G23 = G12;

% G13 = G12;
% G23 = E2/(2*(1+nu23));
% COMPUTE S AND C
Sf= [1/E1      -nu21/E2      -nu31/E3  0  0  0;
     -nu12/E1   1/E2         -nu32/E3  0  0  0;
     -nu13/E1   -nu23/E2     1/E3      0  0  0;
     0  0  0  1/G23  0  0;
     0  0  0  0  1/G13  0;
     0  0  0  0  0  1/G12];
%
Cf = inv(Sf)
%
S1=0; S4=0; S8=0; S9=0;
S3=0.49247-0.47603*Vf-0.02748*Vf^2;
S2=S3;
S6=0.36844-0.14944*Vf-0.27152*Vf^2;
S5=S6;
S7=0.12346-0.32035*Vf+0.23517*Vf^2;
% Trial values
% Initialize P
P = [ 0 0 0 0 0 0;
     0 0 0 0 0 0;
     0 0 0 0 0 0;
     0 0 0 0 0 0;
     0 0 0 0 0 0;
     0 0 0 0 0 0];
%Ptensor.m 12/25/06
P(1,1)=S1/Gm-S4/2/Gm/(1-num);
P(2,2)=S2/Gm-S5/2/Gm/(1-num);
P(3,3)=S3/Gm-S6/2/Gm/(1-num);
P(1,2)=-S9/2/Gm/(1-num); P(2,1)=P(1,2);

```



```

P(1,3)=-S8/2/Gm/(1-num);P(3,1)=P(1,3);
P(2,3)=-S7/2/Gm/(1-num);P(3,2)=P(2,3);
P(4,4)=(S3+S2)/4/Gm-S7/2/Gm/(1-num);
P(5,5)=(S1+S3)/4/Gm-S8/2/Gm/(1-num);
P(6,6)=(S1+S2)/4/Gm-S9/2/Gm/(1-num);
P;
% Initialize Reuter
R = [ 1 0 0 0 0 0;
      0 1 0 0 0 0;
      0 0 1 0 0 0;
      0 0 0 2 0 0;
      0 0 0 0 2 0;
      0 0 0 0 0 2];
% Initialize I(2)
I2 =[ 1 0 0 0 0 0;
      0 1 0 0 0 0;
      0 0 1 0 0 0;
      0 0 0 1 0 0;
      0 0 0 0 1 0;
      0 0 0 0 0 1];
% Calculate Af contracted
Af = ((Cm - Cf)^(-1)) .* (((Cm - Cf)^(-1) - P)^(-1));
Am = (I2 - Vf * Af) / Vm;
C= Cm - Vf*((Cm - Cf)^(-1) - P)^(-1)
%it is the same as writing C=Cm-Vf*(Cm-Cf)*Af
%Alternatively
%C = Vf*Af*Cf + Vm*Am*Cm
% WRITE SOLUTION IN A FILE
% fprintf(fidout,'%10s\n','FIBER STRAIN CONCENTRATION');
% for row=1:6
%     fprintf(fidout,'%10.4e\t %10.4e\t %10.4e\t %10.4e\t %10.4e\t
%10.4e\n',Af(row,1),Af(row,2),Af(row,3),Af(row,4),Af(row,5),Af(row,6));
% end
% fprintf(fidout,'%10s\n','MATRIX STRAIN CONCENTRATION');
% for row=1:6
%     fprintf(fidout,'%10.4e\t %10.4e\t %10.4e\t %10.4e\t %10.4e\t
%10.4e\n',Am(row,1),Am(row,2),Am(row,3),Am(row,4),Am(row,5),Am(row,6));
% end
% fprintf(fidout,'%10s\n','SIFFNESS MATRIX');
% for row=1:6
%     fprintf(fidout,'%10.4e\t %10.4e\t %10.4e\t %10.4e\t %10.4e\t
%10.4e\n',C(row,1),C(row,2),C(row,3),C(row,4),C(row,5),C(row,6));
% end
% fclose(fidinp);
% fclose(fidout);

S=inv(C)
E11=1/S(1,1)
E22=1/S(2,2)
E33=E22
G12=1/S(4,4)
G13=G12
Nu12=-S(1,2)*E11
Nu13=Nu12
Nu23=-S(2,3)*E22
G23=E22/2*(1+Nu23)

```

FITTING VISCOELASTICITY PARAMETERS TO EXPERIMENTAL CURVES

```

x1=[600*2*pi
    700*2*pi
    1000*2*pi
    1200*2*pi
    1500*2*pi
    1800*2*pi
    2000*2*pi];

y1=[315
    555
    2410
    3300
    6520
    3350
    3070]; %dati di loss modulus

ys=[569
    1310
    3630
    9630
    11700
    7860
    11700]; %dati di storage modulus

a =      50000 %sposta la curva in alto (se aumenta) o in basso
g1 =     0.006 %aumentando crea un'ulteriore gobba sulla sx
g2 =     0.09  %aumentando elimina la seconda gobba a sx e fa
schizzare il lim per 0 in su
g3=       0.4
t1 =     0.09
t2 =     0.7   %ha pochissima influenza sulle curve
t3=0.0001     %sposta la curva a sinistra se aumenta

i=0;
xv=linspace(0,2*pi*40000,40000)
for i=1:40000
    x=xv(i);
g_loss(i)=a*((g1*t1*x)/(1+t1^2*x^2)+(g2*t2*x)/(1+t2^2*x^2)+(g3*t3*x)/(1+t
3^2*x^2)); %formula per Gloss
g_storage(i)=a*(1-
(g1+g2+g3))+a*((g1*t1^2*x^2)/(1+t1^2*x^2))+((g2*t2^2*x^2)/(1+t2^2*x^2))+
((g3*t3^2*x^2)/(1+t3^2*x^2))); %formula per Gstorage
end

loglog(xv,g_loss,x1,y1); legend('Loss modulus simulation','Loss modulus
experimental'); title('Shear Modulus vs Frequency');
xlabel('Frequency (w)'); ylabel ('Shear modulus')
figure

```

```

loglog(xv,g_storage,xl,ys); legend('Storage modulus simulation','Storage
modulus experimental'); title('Shear Modulus vs Frequency');
xlabel('Frequency (w)'); ylabel ('Shear modulus')

```

MIRRORING THE DATA: FROM A QUARTER SLICE TO THE ENTIRE GEOMETRY

```

%%u3rz=u3r6000_11
j=0
for i=1:length(z)
    if(z(i)==1)
        j=j+1;
        xr(j)=x(i);
        yr(j)=y(i);
        u3r(j)=zdisp1(i);
    end
end
j
xmax=2;
dx=0.01;
[xq,yq] = meshgrid(0:dx:xmax, 0:dx:xmax);
vq = griddata(xr,yr,u3r,xq,yq,'cubic');
mesh(xq,yq,vq)
ju=j;
ju1=ju;
plot3(xr,yr,u3r)

for i=1:ju

    xr(ju+i)=-xr(i);
    yr(ju+i)=yr(i);
    u3r(ju+i)=u3r(i);

end
ju=ju+ju;
for i=1:ju1

    xr(ju+i)=-xr(i);
    yr(ju+i)=-yr(i);
    u3r(ju+i)=u3r(i);

end
ju=ju+ju1;
for i=1:ju1

    xr(ju+i)=xr(i);
    yr(ju+i)=-yr(i);
    u3r(ju+i)=u3r(i);

end
end

```

```

xmax=3;
dx=2*xmax/100;
[xq,yq] = meshgrid(-xmax:dx:xmax, -xmax:dx:xmax);
vq = griddata(xr,yr,u3r,xq,yq);

mesh(xq,yq,vq)

%x=coordhor(:,2);
%y=coordhor(:,3);
%z=coordhor(:,4);
%zdispl=tryouthor(:,4);

```

APPLYING FAST FOURIER TRANSFORM TO THE DISPLACEMENT DATA

Mirroring

% Code used to mirror the quarter sliced geometry on the xz and yz plane

```

%u3rz=u3r6000_11
x=coordhorfettina(:,2);
y=coordhorfettina(:,3);
z=coordhorfettina(:,4);
zdispl=tryouthorfettina(:,4);

j=0
for i=1:length(z)
    if(z(i)==1)
        j=j+1;
        xr(j)=x(i);
        yr(j)=y(i);
        u3r(j)=zdispl(i);
    end
end
j
xmax=3;
dx=2*xmax/100;
[xq,yq] = meshgrid(0:dx:xmax, 0:dx:xmax);
vq = griddata(xr,yr,u3r,xq,yq, 'cubic');
mesh(xq,yq,vq)
ju=j;
ju1=ju;
plot3(xr,yr,u3r)

for i=1:ju

    xr(ju+i)=-xr(i);
    yr(ju+i)=yr(i);
    u3r(ju+i)=u3r(i);

```

```

end
ju=ju+ju;
for i=1:ju1

    xr(ju+i)=-xr(i);
    yr(ju+i)=-yr(i);
    u3r(ju+i)=u3r(i);

end
ju=ju+ju1;
for i=1:ju1

    xr(ju+i)=xr(i);
    yr(ju+i)=-yr(i);
    u3r(ju+i)=u3r(i);

end
xmax=3;
dx=2*xmax/100;
[xq,yq] = meshgrid(-xmax:dx:xmax, -xmax:dx:xmax);
vq = griddata(xr,yr,u3r,xq,yq);
mesh(xq,yq,vq)

%x=coordhor(:,2);
%y=coordhor(:,3);
%z=coordhor(:,4);
%zdisp1=tryouthor(:,4);

```

FFT_Fettina

```

% Code used to apply the 2D Fourier transform to the displacement maps
close all
zdisp=u3r;
ut=zdisp;
xmax=3;
dx=2*xmax/100;

% - an ordered coordinates grid is created and the displacement data
(ALONG X,Y AND Z) ut are interpolated at the query points of the new
ordered mesh
[xq,yq] = meshgrid(-xmax:dx:xmax, -xmax:dx:xmax);
vq = griddata(xr,yr,ut,xq,yq);
[row, col] = find(isnan(vq));

%pause
for i=1:length(row)
for j=1:length(col)
vq(row(i),row(j))=0;
end
end
mesh(xq,yq,vq)
pause
f2=fft2(vq);

```

```

f2shift=abs(fftshift(f2));
clims = [0 0.1]

% - the Fourier transform is rearranged by shifting the zero-frequency
component to the center of the array
figure
imagesc(abs(fftshift(f2)),clims);

% - the insitu_dft function, reported below, is recalled
Xd=-xmax:dx:xmax;
Yd=Xd
[F,Xr,Yr] = insitu_dft(vq,Xd,Yd);
figure
%surf(f2)
surf(f2shift)

figure
plot(f2shift(51,:)) %y for x=51
hold on
plot(f2shift(:,51)) %x for y=51
legend('y values for x=51','x values for y=51');

```

Insitu_DFT

```

% This .m file is meant to compute the Discrete Fourier Transform of an
% image

```

```

function [F,Xr,Yr] = insitu_dft(I,Xd,Yd)

%% - set text options
set(0,'defaulttextinterpreter','latex')
fontname = 'Helvetica';
set(0,'defaultaxesfontname',fontname);
set(0,'defaulttextfontname',fontname);
fontsize = 12;
set(0,'defaultaxesfontsize',fontsize);
set(0,'defaulttextfontsize',fontsize);

%% - compute DFT
%%I = varargin{1};
[Ny, Nx] = size(I);
%%Xd = 0:Nx-1;
%%Yd = 0:Ny-1;
debug = 1;

%if nargin > 1 Xd = varargin{2}; Yd = varargin{3}; end
%if nargin > 3 debug = varargin{4}; end

% - define physical space grid
dXd = Xd(2) - Xd(1);
Nx = length(Xd);
dYd = Yd(2) - Yd(1);
Ny = length(Yd);
% - compute Discrete Fourier Transform
% I = mat2gray(I); % enhance image contrast
F = fft2(I);

```

```

% - shift F to the center
F = fftshift(F);
% - cut at Nyquist frequency
%%F = F(Ny/2 - Ny/8 : Ny/2 + Ny/8 , Nx/2 - Nx/8 : Nx/2 + Nx/8);
F = abs(F);

% - define reciprocal space
Ksx = 1/dXd;
dXr = Ksx / Nx;
Ksy = 1/dYd;
dYr = Ksy / Ny;
Xr = -Ksx : dXr : Ksx;
Yr = -Ksy : dYr : Ksy;

%% - (if requested) display results

if debug

    % - create subplot to show Spectrum both in linear and logarithmic
    % scales
    figure('units','normalized','outerposition',[0 0 1 1]);
    set(gcf,'Name','Surface fit results','NumberTitle','off','color','w')

    % ... linear scale
    subplot(1,2,1);
    clim=[0. 0.00001];
    imagesc(Xr,Yr,F/(Nx*Ny),clim);
        axis equal
    title('Power Spectrum - \textbf{linear} scale')
    colormap jet;
    colorbar
    set(gca,'YDir','normal');
    xlabel('\lambda_{x}^{-1} [mm^{-1}]','FontSize',15);
    ylabel('\lambda_{y}^{-1} [mm^{-1}]','FontSize',15);

    % ... log scale
    subplot(1,2,2);
    imagesc(Xr,Yr,log(F+1));
    title('Power Spectrum - \textbf{logarithmic} scale')
    axis equal
    colormap jet;
    colorbar
    set(gca,'YDir','normal');
    xlabel('\lambda_{x}^{-1} [mm^{-1}]','FontSize',15);
    ylabel('\lambda_{y}^{-1} [mm^{-1}]','FontSize',15);

    %%close(gcf)

end

```

7 APPENDIX B: USER DEFINED FUNCTIONS

UMAT TO DEFINE VISCOELASTIC PROPERTIES OF THE SIMULATION MATERIAL

```
SUBROUTINE UMAT(STRESS,STATEV,DDSDDE,SSE,SPD,SCD,  
1 RPL,DDSDDT,DRPLDE,DRPLDT,  
2 STRAN,DSTRAN,TIME,DTIME,TEMP,DTEMP,PREDEF,DPRED,CMNAME,  
3 NDI,NSHR,NTENS,NSTATV,PROPS,NPROPS,COORDS,DROT,PNEWDT,  
4 CELENT,DFGRD0,DFGRD1,NOEL,NPT,LAYER,KSPT,JSTEP,KINC)  
  
C  
    INCLUDE 'ABA_PARAM.INC'  
  
C  
    CHARACTER*80 CMNAME  
    DIMENSION STRESS(NTENS),STATEV(NSTATV),  
1 DDSDE(NTENS,NTENS,2),  
2 DDSDDT(NTENS),DRPLDE(NTENS),  
3 STRAN(NTENS),DSTRAN(NTENS),TIME(2),PREDEF(1),DPRED(1),  
4 PROPS(NPROPS),COORDS(3),DROT(3,3),DFGRD0(3,3),DFGRD1(3,3),  
5 JSTEP(4)  
    DIMENSION DSTRES(6),D(3,3)  
  
C  
C EVALUATE NEW STRESS TENSOR  
C  
C User material parameters definition.  
C     adir= anisotropy direction (1,2,3)  
C  
C     amu0_par=props(1) !! mu_0 parallelo  
C     apar=amu0_par  
C     g1=props(2)  
C     g2=props(3)  
C     g3=props(4)  
C     t1=props(5)
```



```

t2=props(6)
t3=props(7)

amu0_per=props(8)
aper=amu0_per

anu=props(9)
adir=props(10)
C
C frequency vector and Pi definition
x=time(1) !!! frequenza

anup=anu
Pi=3.141592
C
C muR and muI definition
C
amuR_par=apar*(1.d00-
(g1+g2+g3))+a*(((g1*t1**2*x**2)/(1+t1**2*x**2))+
+
((g2*t2**2*x**2)/(1+t2**2*x**2))+((g3*t3**2*x**2)/(1+t3**2*x**2)))
C
amuR_per=aper*(1.d00-
(g1+g2+g3))+a*(((g1*t1**2*x**2)/(1+t1**2*x**2))+
+
((g2*t2**2*x**2)/(1+t2**2*x**2))+((g3*t3**2*x**2)/(1+t3**2*x**2)))
C
amuI=apar*((g1*t1*x)/(1+t1**2*x**2)+(g2*t2*x)/(1+t2**2*x**2))+
+ (g3*t3*x)/(1+t3**2*x**2));
C amuR_par=11700*(10E-6)
C amuR_per=0.86*amuR_par

```

```

C      amuI=6520*(10E-6)
C
C      E' and E'' definitions
      Ep=2*amuR_per*(1+anu)
      Ez=2*amuR_par*(1+anu)
      Ep2=2*amuI*(1+anu)
      Ez2=Ep2
C
C      Delta definition
      aD=(1+anup)*(1-anup-2*anup**2)/(Ep**2*Ez)
      aD2=(1+anup)*(1-anup-2*anup**2)/(Ep2**2*Ez2)
C
C
C      Stiffness matrix C initialization
C
      DO K1=1,NTENS
        DO K2=1,NTENS
          DDSDDDE(K2,K1,1) = 0.
        END DO
      END DO
C
C      First quadrant
      DO K1=1,NDI
        DO K2=1,NDI
          DDSDDDE(K2,K1,1) = (anu+anu*anup)/(Ep*Ez*aD)
        END DO
      END DO
C
C
C      First quadrant diagonal
C
      DO K1=1,NDI
        DDSDDDE(K1,K1,1) = (1-anu**2)/(Ep*Ez*aD)
      END DO

```

```

C
      DDSDE(adir,adir,1) = (1-anup**2)/(Ep**2*aD)
C
C Changing different components
C
      DO K1=1,NDI
        DO K2=1,NDI
          IF (K1.NE.adir.AND.K2.NE.adir.AND.K1.NE.K2) THEN
            DDSDE(K1,K2,1) = (anup+anu**2)/(Ep*Ez*aD)
          END IF
        END DO
      END DO

C
C Fourth quadrant diagonal
C
      DO K1=NDI+1,NDI+NSHR
        DDSDE(K1,K1,1) = Ez/(1+anup)
      END DO

C
C mu_perpendicular
      K1=adir+NDI
      DDSDE(K1,K1,1) = Ep/(1+anup)

C
C
C Damping matrix D initialization
      DO K1=1,NTENS
        DO K2=1,NTENS
          DDSDE(K2,K1,2) = 0.
        END DO
      END DO

C
C First quadrant
C
      DO K1=1,NDI
        DO K2=1,NDI

```

```

                DDSDE(K2,K1,2) = (anu+anu*anup)/(Ep2*Ez2*aD2)
            END DO
        END DO
C
C
C First quadrant diagonal
C
        DO K1=1,NDI
            DDSDE(K1,K1,2) = (1-anu**2)/(Ep2*Ez2*aD2)
        END DO
C
        DDSDE(adir,adir,2) = (1-anup**2)/(Ep2**2*aD2)
C
C Changing different components
C
        DO K1=1,NDI
            DO K2=1,NDI
                IF (K1.NE.adir.AND.K2.NE.adir.AND.K1.NE.K2) THEN
                    DDSDE(K1,K2,2) = (anup+anu**2)/(Ep2*Ez2*aD2)
                END IF
            END DO
        END DO
C
C Fourth quadrant diagonal
C
        DO K1=NDI+1,NDI+NSHR
            DDSDE(K1,K1,2) = Ez2/(1+anup)
        END DO
C
C mu_perpendicular
        K1=adir+NDI
        DDSDE(K1,K1,2) = Ep2/(1+anup)
C
C Stress definition
        do is=1,NTENS

```

```

        STRESS(is)=0
        do it=1,NTENS
            stress(is)=stress(is)+DDSDDE(is,it,1)*STRAN(it)
        end do
    end do
C
C
1001 format(6f12.5)
    RETURN

    END

```

DISP.PY: THE PYTHON CODE TO EXTRACT DISPLACEMENT AND COORDINATES DATA FROM THE ODB FILE

```

import odbAccess
#odb=session.openOdb('mre_homtools.odb')
odb=odbAccess.openOdb(path='fettina2_CG.odb')
timeFrame=odb.steps['Step-2'].frames[2]
displacement=timeFrame.fieldOutputs['U']
coord=timeFrame.fieldOutputs['COORD']
pipenode=odb.rootAssembly.instances['PART-1-1'].nodeSets['SET-1']
pipenodeDIsp=displacement.getSubset(region=pipenode)
pipenodeCoord=coord.getSubset(region=pipenode)
myoutfile=open('tryouthor_fettina.txt','w+')
myoutfile1=open('coordhor_fettina.txt','w+')
myoutfile.write("Node  ")
myoutfile.write("xdisp  ")
myoutfile.write("ydisp  ")
myoutfile.write("zdisp\n")
myoutfile1.write("Node  ")

```

```

myoutfile1.write("x ")
myoutfile1.write("y ")
myoutfile1.write("z\n")
for v in pipenodeDIsp.values:
    print "Node1 label= %d",v.nodeLabel
    myoutfile.write(str(v.nodeLabel))
    myoutfile.write(" ")
    print "x disp=",v.data[0]
    myoutfile.write(str(v.data[0]))
    myoutfile.write(" ")
    print "x disp=",v.data[1]
    myoutfile.write(str(v.data[1]))
    myoutfile.write(" ")
    print "x disp=",v.data[2]
    myoutfile.write(str(v.data[2]))
    myoutfile.write("\n")
myoutfile.close()
for v in pipenodeCoord.values:
    print "Node1 label= %d",v.nodeLabel
    myoutfile1.write(str(v.nodeLabel))
    myoutfile1.write(" ")
    print "x disp=",v.data[0]
    myoutfile1.write(str(v.data[0]))
    myoutfile1.write(" ")
    print "x disp=",v.data[1]
    myoutfile1.write(str(v.data[1]))
    myoutfile1.write(" ")
    print "x disp=",v.data[2]
    myoutfile1.write(str(v.data[2]))
    myoutfile1.write("\n")
myoutfile1.close()
odb.close

```

In collaboration with University of
Illinois at Chicago, Richard and Loan
Hill Department of Bioengineering